KINETICS OF THE FORMATION OF AN AMORPHOUS LAYER DURING A SOLID STATE REACTION

Thesis by

BENJAMIN PAUL DOLGIN

In Partial Fulfillment of the Requirements
for the Degree of
Doctor of Philosophy

California Institute of Technology
Pasadena, California

1985

(Submitted June 11, 1984)

ACKNOWLEDGEMENTS

I would like to express my gratitude to Dr. Marc Van Rossum who was the first one to believe in what is written in this thesis and to Michael Atzmon whose constructive criticism was more than helpful. I appreciate the assistance of my advisor Dr. W. L. Johnson whose original discovery of the Solid State Reaction initiated this thesis.

I must mention the names of my parents who are the reason I have become what I am. My wife was always with me when I needed her and it is impossible to overestimate her help and support. Her direct contribution to this thesis is the translation of the text from Russian English into the language spoken in the United States. The reader should appreciate this. Mr. and Mrs. Samuel Goldfarb have helped me from the moment I came to this country; and I doubt I could have done half of what I have been able to accomplish without them. I want to thank Mrs. Angela Bressan who has influenced every aspect of life for the people working on the third floor of Keck building and who is the spirit of the lab in which I spent more than three years.

I appreciate the help of Dr. W. J. Hamilton who made his SIMS analyzer available for my research. I needed the assistance P. F. Koen in TEM studies. Consultations with Prof. B. Fornberg helped in solving the numerical equations. The funding of my work by the United States Department of Energy is greatly appreciated.

ABSTRACT

Solid State reaction as a new method of amorphous film fabrication was introduced by R. Schwartz and W. L. Johnson in 1983. A thermodynamic explanation for the process given by the original article provides a clue to understanding the forces making the reaction possible. This thesis emphasizes the kinetic approach to the description of the reaction. The movements of the interfaces as a fundamental mechanism of the reaction is suggested. The reaction in La-Au and Ni-Hf multilayers is described. Resistance measurements, TEM and SIMS techniques, and Rutherford backscattering are used to study the process.

The thesis contains a proof that the final product of the Solid State Reaction is amorphous. It describes the morphology of the reacting multilayers. The one-dimensional and multi-dimensional processes taking place during the growth are separated. The thesis connects the properties of the reaction with known properties of the "fast diffusion." The phenomenological model for the reaction is introduced. The model consists of a diffusion equation with a new set of boundary conditions. The amorphous layer growth rate in the limit of short time is found to be $X=1-\exp(-At)$ and $X=-1/(A-1)+(2at)^{1/2}$ in the limit of long time. The "steady state" approximation as a solution to the diffusion equations in the limit of long time is found to be incorrect. The model shows excellent agreement with the experimental data.

TABLE OF CONTENTS

page

LIST OF ILLUSTRATIONS

page

I. INTRODUCTION.

Solid State Reaction as a method of the formation of amorphous materials was introduced by R. Schwarz and W. L. Johnson in 1983. Currently, there are only four publications on this subject available to a researcher. All of these publications describe the successful attempts to stage a Solid State Reaction. The original paper by Schwarz and Johnson explains the reaction in terms of the Gibbs free energy. The questions of the validity of this explanation and the kinetics of the reaction have not been addressed yet. The necessary and sufficient conditions for performing the reaction have not been established, either. This thesis proposes an answer to the question of the kinetics of the reaction. The model for the reaction suggests the type of the conditions which influence the possibility of the process.

Chapter II of the thesis gives a review of the methods of the formation of amorphous solids and the place of the Solid State Reaction among them. It also discusses fundamentals of the diffusion which is an important part of the Solid State Reaction.

Chapter III describes the preparation of the lanthanum gold samples for the Solid State Reaction and the experimental techniques used in this thesis to study the reaction.

Chapter IV presents the experimental evidence that the final product of the Solid State Reaction is amorphous. The correlations between the properties of the Reaction and the parameters of the diffusion are portrayed. Physical properties and topology of the reacting multilayers are described in this chapter as well.

Chapter V introduces a phenomenological model for the Solid State Reaction in the gold lanthanum multilayers and compares it with the experimental data. The diffusion equations which are solved in this chapter describe the growth of a wide class of interlayers which are not necessarily amorphous.

Chapter VI compares the prediction of the model described in Chapter V with the measurement on the reacting Ni-Hf samples performed by Dr. M. Van Rossum. This chapter summarizes the properties of the Solid State Reaction discovered so far.

II. THEORETICAL AND EXPERIMENTAL BACKGROUND.

II.1 FORMATION OF THE METALLIC GLASSES.

Traditionally, a glass is defined as an undercooled liquid brought below a characteristic freezing temperature referred to as a glass transition temperature T_g. The formation of the glass requires that the process of crystallization be bypassed during cooling through the thermodynamic melting point T_m and the undercooled temperature range to below T_g. Once cooled much below this crystallization region, the glass stays in the metastable state for a period of time which for all practical purposes can be regarded as infinity. In 1960, Duwez, et al.[1,2], using what is now called the Duwez gun, discovered the first metal-metalloid glasses (Au-Ge and Au-Si). Since then, the gun and numerous other techniques were used to obtain a number of metallic and metal-metalloid glasses.

The techniques utilizing an approach similar to the one introduced by Duwez, are usually referred to as Rapid Liquid Quenching. There are several methods belonging to this general category. The Duwez Gun is designed to direct a spray of an atomized melt of an alloy to a cold copper substrate where the droplets will be cooled below T_g at a rate up to 10^7K per second. In a Piston and Anvil method[3,4], a droplet of melted alloy is smashed between two moving copper surfaces to produce a foil of approximately 10-60 μm thick. In a Melt Spinner[5], a melted alloy is brought in touch with a fast spun cold copper wheel. This method and its subsequent modifications are able to produce a continuous glassy ribbon up to 1 meter wide and are used in the industrial production of amorphous materials. All of the above methods are characterized by cooling rates from 10^2 to 10^7 K/sec. Another Rapid Liquid Quenching technique is associated with a much higher cooling rate of up to 10^{10} K/sec. This technique is laser glazing[6]. In this method, the laser beam is used to overheat a small and shallow area of the surface of the sample. The bulk of the material serves as a heat sink. Figure 1 illustrates the principal methods of Rapid Liquid Quenching.

To create an amorphous material, one must bypass crystallization. The nucleation and growth of crystals in an undercooled melt involves atomic rearrangements which occur on a time scale τ_x, which should depend on the temperature, pressure, etc. of the surrounding media. By the nature of the process, the temperature and the pressure of the sample itself are not easy to define. A metastable glass/liquid does not have the opportunity or the time to probe all the energetically available states in the phase space as the equilibrium thermodynamics would require. The system is able to probe only the immediate surroundings of the point in the phase space where the system is located at any given moment. Moreover, the division of the system into smaller subsystems would not be helpful, either. Thermodynamics require that the size of the subsystems be large enough to be treated as a thermodynamic system. At the same time their size must be small enough to satisfy the conditions of a system in equilibrium. These two demands can not be sustained at the same time in the case of the formation of metallic glasses. The described

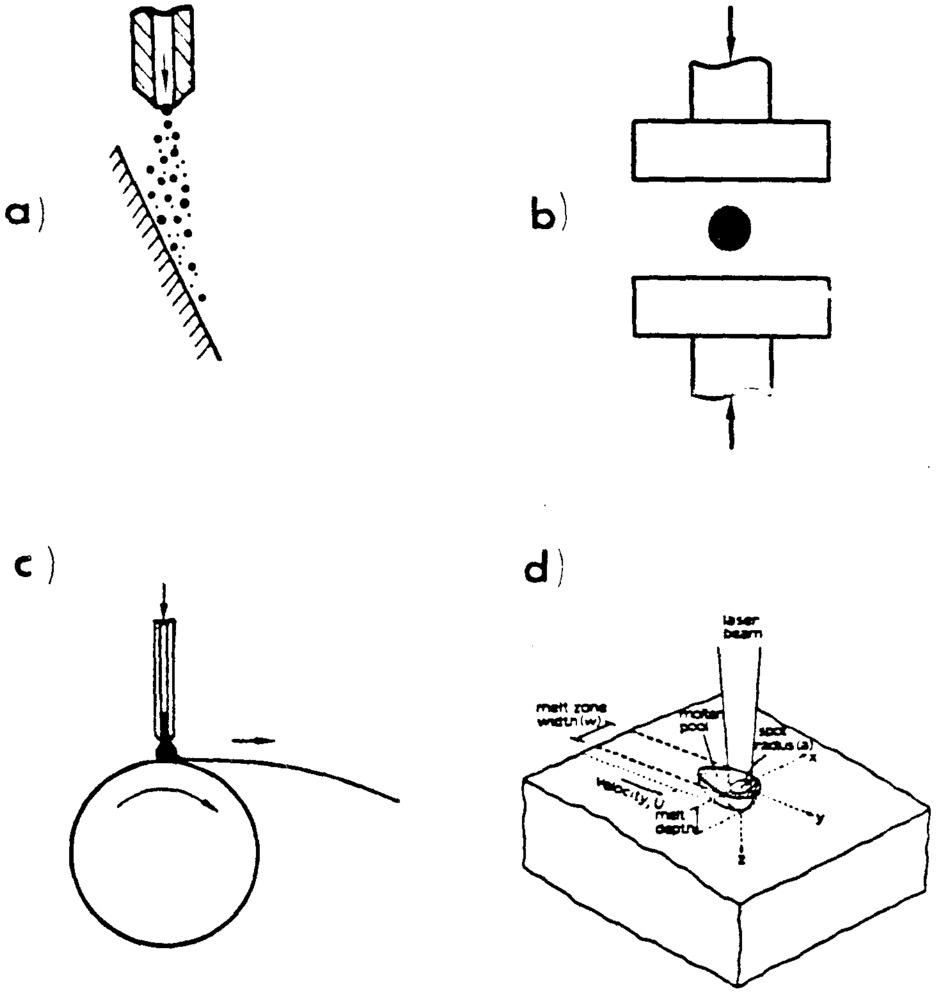

Fig. 1. Principal methods of the Rapid Liquid Quenching: a) "Duwez Gun," b) Piston and Anvil, c) Melt spinner, d) Laser glazing (Fig. 1d is from Ref. 38)

situation prompts one to introduce an effective or fictitious temperature, pressure etc. These new parameters lose one of the main properties of their thermodynamic counterparts. The set of pressure, temperature, and volume of the system can no longer completely describe the state of the system. It requires the introduction of some less conventional degrees of freedom to complete the description. From this point on, unless it is stated otherwise, whenever temperature or pressure is mentioned, one of the two following definitions is applicable. It is the temperature or the pressure of the thermal bath in which the glass is contained. Or, it is the effective temperature, volume, and pressure of the glass in the situation where all the atomic motions are restricted in a special way. Atomic motion should not sample the points describing the state of the system in the phase space far away from the position where it was located initially. Also this motion should not involve tunneling through the potential barriers with the height much larger than kT.

Very roughly, the cooling of the liquid through the undercooled region must take place on a time scale τ_c such that $\tau_c > \tau_x$ in order to achieve the glassy state. Detailed theories which lead to specific criteria for the case of metallic liquids have been put forth by Turnbull and others[7]. For a pure liquid metal, liquid quenching is unable to provide a low enough value of τ_c in order to bypass the crystallization. For some alloys, typically those with the composition lying near a deep eutectic, the rate of cooling is fast enough to produce a metallic glass. The "deep eutectic" criteria for glass formation is associated naturally with the fact that the undercooling interval T_m-T_g or reduced undercooling interval $\Delta=(T_m-T_g)/T_m$ is typically smaller for alloy compositions near the deep eutectic.

Historically, the Liquid-Quenched glasses were not the first amorphous metallic systems discovered. Vapor-Quenched amorphous metals were studied by Buckel and Hilsch[8] as early as 1954. In this method, a vapor of a metal or a mixture of metals is condensed on a substrate cooled to an appropriate temperature. Depending on the material, liquid helium temperatures are required sometimes. The difference between the rate of growth of the condensed material and the rate of atomic rearrangement on its surface determines whether the condensate remains in a crystalline or an amorphous form. The low temperature of the substrate restricts all atomic rearrangement to the surface of the growing layer. Deep eutectic criteria are not a limitation for the vapor quenching. The vapor-quenched amorphous materials can be produced in much wider ranges of concentrations of constituencies for different alloys. Subsequent studies[7,9] have shown that vapor quenched amorphous alloys are often nearly structurally indistinguishable from their liquid quenched counterparts. In this sense, the use of the two terms metallic "glass" and "amorphous alloy" reflects the two methods of preparation as opposed to two fundamentally different materials. Currently, the terms "glass" and "amorphous material" are often used interchangably. The term "glass" will herein be used to refer to an amorphous material irrespective of its origin.

Both of the methods for the formation of amorphous solids have the same underlying principle. The formation of the amorphous material proceeds on a time scale which is much faster than the time scale required for recrystallization. Rapid Liquid and Vapor Quenching use liquids and gas media as a way of creating a glass. Plasma and solid state can be utilized also. Plasma Spraying (Cahn[10]) was introduced in 1978. It is a development of the original "Duwez Gun." In 1983, Schwarz and Johnson[11] proved that a solid state reaction can produce a metallic material which was claimed to be amorphous. TEM studies of the reacted La-Au samples made by the author[12] were one of the arguments confirming this discovery. Amorphous alloys were also produced by hydrogenization (X. L. Yeh, et al.[13] 1983). This method can be regarded as a solid state reaction as well.

All the methods which create amorphous materials must start with some thermodynamically stable ingredients. Then, some process should bring the system into a metastable amorphous state. This transition can be achieved as a bulk transformation when low speed of recrystallization and nucleation barriers can prevent the system from proceeding to the lowest energy state. The examples of the bulk type transformation are ion mixing[14], ion implantation[15], and straight forward undercooling of an ultrapure material[16]. The other way to create an amorphous material is through the aid of a fast moving interface. Once glass is formed, low temperatures prevent it from recrystallization (no homogeneous nucleation). The fast moving interface prevents surface rearrangements from creating any type of crystallites. The majority of modern glass formation methods belongs to this category. Some Liquid Rapid Quenching methods, Vapor Quenching, cosputtering and coevaporation techniques, electrodeposition, can all be characterized by a fast moving interface. This interface separates the formed glass from conventional thermodynamic substances. Solid State Reaction belongs to this category as well. The question of what kind of material is produced by the solid state reaction is decided at the interfaces. The rate of reaction can be determined by some other factors. For example, diffusion can limit the rate of the reaction. It may take too much time to grow an extremely thick layer of glass. In this case, the nucleation in the bulk, especially homogeneous nucleation, becomes an important factor. But the question whether the reaction can produce any amorphous material at all is decided at the interfaces.

The La-Au system can serve as an example of a reacting binary system. Every statement in the following discussion is true for this system. Since the Au-La system is not unique in this sense, it is more appropriate to talk about a general binary alloy A-B. The following is paraphrased from Ref. 12 (Johnson, Dolgin and Van Rossum). Consider a binary alloy system $A_{1-x}B_x$ at temperature T_1 lying everywhere below the liquidus curve of the equilibrium A-B phase diagram shown in Fig. 2. One assumes that pure solids A and B have crystalline structures α and β, respectively, and can exothermically react to form several crystalline intermetallic compounds (e.g., γ - AB, δ - AB_2, and ϵ - A_2B). That is, the solid elements A and B have a large negative heat of mixing with respect to the crystalline compounds of structure γ, δ, and ϵ. In contrast, assume that the heat of mixing for the terminal solutions α and β are characterized by a large and positive value. This situation is characteristic of a large number of binary alloy systems. Let us add to this still rather general case an additional assumption that the binary liquid $A_{1-x}B_x$ is characterized by a large negative heat of

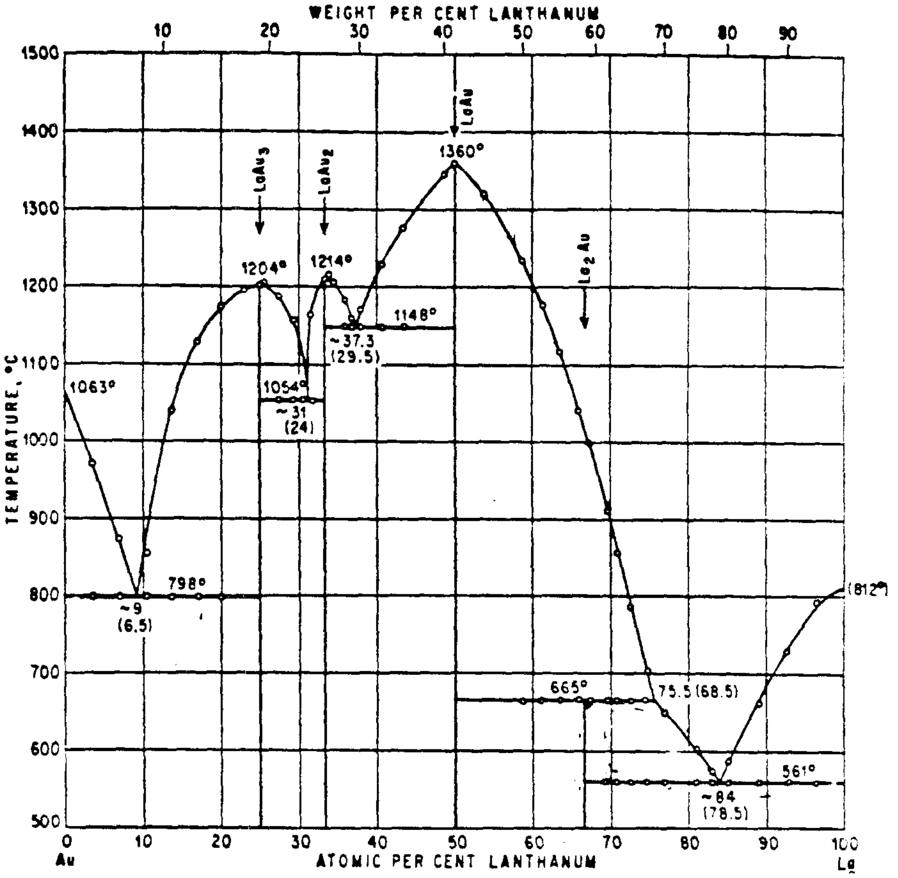

Fig. 2. Equilibrium phase diagram for La - Au system (From Ref. 27).

mixing with respect to the pure liquids. Again this is a rather common situation (see, for example, Miedema[17,18]). At temperature T_1, a free energy diagram corresponding to Fig. 2 is shown in Fig. 3. The free energy of the liquid state is shown[11] and labeled by λ. The λ - curve represents a metastable liquid state since T_1 lies below the temperature range where a thermodynamically stable liquid can not exist. For $T_1<T_g$, the λ - curve will be used to represent a glass. The question of justification of the existence of this metastable curve is not addressed here. For a discussion of the justification, the reader is referred, for example, to Penrose and Lebowitz[19]. In addition, the approximate positions of the free energy vs. composition curves for the α, β, γ, δ, and ϵ phases are shown in Fig. 3, although they have not been calculated. The thermodynamic parameters mentioned in this description are used in the sense discussed in this chapter. Notice that the terminal points of λ - curve represent undercooled liquids of pure A and B at temperature T_1. The differences between these terminal points and those of the α - and β - curves give the free energy of crystallization of the pure undercooled metals A and B. Following Turmbull[20], this difference can be simply approximated by

$$\Delta H_{\alpha-\lambda}(T_1) = \left[\frac{T_m^\alpha - T_1}{T_m^\alpha}\right] \Delta H_m^\alpha$$

where T_m^α and ΔH_m^α are the melting point and heat of fusion for pure α - A (or β - B). More sophisticated approximations could be used as well[21]. In any case, this allows one to fix the endpoints of the λ - curve.

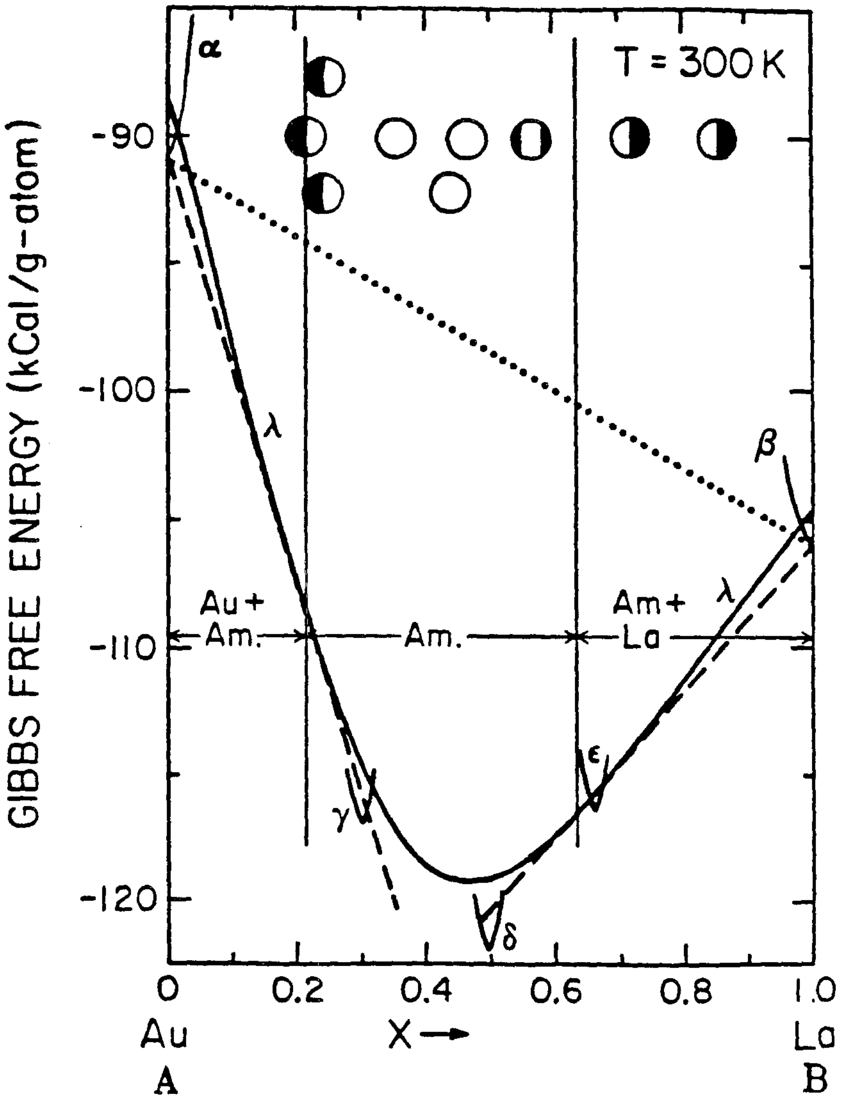

Fig. 3. Gibbs Free Energy diagram for La - Au system (after Ref. 11). See description in the text.

Now consider a problem depicted in Fig. 4. A layer of liquid or glass is brought into contact with layers of pure solids A and B at a temperature T_1. How will this system evolve in time? Let us say that concentrations of this glass or liquid at the interfaces are $A_{1-x_1}B_{x_1}$ and $A_{1-x_2}B_{x_2}$. The creation of the amorphous compounds at the interfaces already significantly decreases the free energy of the system. If the interfaces were in place long enough, the diffusion would bring the necessary amount of corresponding elements and would change atomic arrangements so that a "proper" thermodynamically favorable compound would precipitate. But the interface moves. Later in this thesis, this movement will be characterized by a constant κ which relates the concentration at the interface with the speed of movement of the interface. This parameter was introduced by Dolgin and Johnson[22]. The time constant which is associated with the movement of the interface will be shown to be $\tau_G = D/\kappa^2(C_1-C_2)^2$, where D is a diffusion coefficient, and C's are the concentrations of a diffusant at the corresponding interfaces. The type of the compound being created depends on the ratio of τ_X and τ_G.

Formation of crystalline compounds requires significant atomic rearrangements. These rearrangements can involve a tunneling through some nucleation barriers. The latter process has a small probability at low temperatures of the Solid State Reaction. The nucleation barriers can suppress the formation of some or all of the crystalline compounds. Primitive cells of the compounds γ, δ and ϵ in Fig. 3 may be comparatively large[27]. The large size of the cells means a tremendous amount of correlated atomic rearrangements during nucleation and,

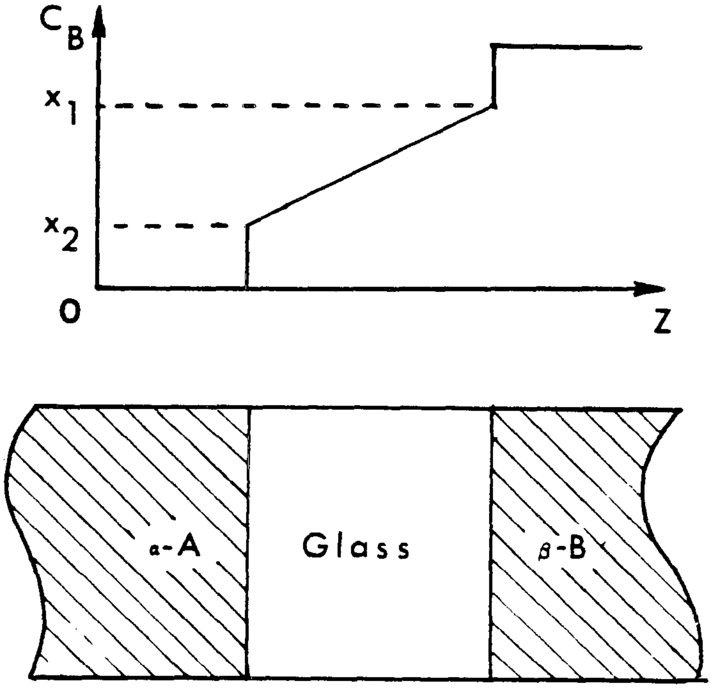

Fig. 4. Binary diffusion couple containing a glassy/liquid interlayer.

as a consequence, high nucleation barriers. At low temperatures, the behaviour of the La-Au system can be governed by an effective Gibbs free energy diagram which does not have any crystalline compounds except α and β. In this case, the product of the solid state reaction would be determined by the common tangent rule[43] applied to curves α, β and γ. The description which will be introduced below belongs to Schwarz and Johnson[11]. The common tangent rule divides the phase diagram into 3 regions (see Fig. 3.). If the reacting layers are Au rich, then the lowest Gibbs free energy state will be a mixture of Au and an amorphous alloy. La rich compositions will produce La and amorphous alloy mixtures. There is a region in between where a pure amorphous product of the reaction can be expected. The values of the concentration which separate these three regions are shown in Fig. 3. These values also correspond to the concentrations at which amorphous and crystalline phases can coexist. The fact that these concentrations exist will be used extensively in the mathematical model of the Solid State Reaction described in Ch. V.

The physics of the interfaces was suggested to be crucial to understanding the properties of the Solid State Reaction. The interface between two solids is different from any other interface. Ever since the discovery of the Kirkendal effect[34], the atomic rearrangement during the growth and the excess molar volume of formation of a new phase became important arguments in the description of the interlayer growth. The interface between the glass and a crystlline solid is no exception. The coherence of atomic arrangement is lost at the interface. The situation in question lies in between what is observed in crystals and liquids. A liquid can not sustain any stress. There is nearly no stress in the solid which is in contact with a liquid, either. A crystal can withstand some stresses. Because of this, the geometry of the interlayer of the reacting couple of crystals goes through complicated transformations. More than this, even if the excess molar volume is zero, some geometrical transformations will take place anyway. The atomic rearrangements required to form a noncoherent interface introduce stresses. These stresses can penetrate deeply into the solids. The liquid / solid interface lacks the ability to support stress. The excess molar volume of glass formation and the ability of the glass to sustain stress are smaller than those of crystals (see for example Ref. 7; for the case of La-Au see Ref. 35). Nevertheless, the influence of stress determines many features in the behaviour of the forming glass. This influence has not been addressed properly at the current stage of research of the Solid State Reaction. The author believes that the understanding of the properties of the interfaces requires an adequate description of these stresses. Some discussion of the manifestation of those stresses can be found in Chapters IV and VI.

Recent experiments[22,23] have shown that the values of κ and D are interrelated. As such, the higher value of D corresponds to a higher value of κ (see Chapters V and VI). This relation explains the fact that higher values of D correspond to extremely low τ_G. The latter is the reason why the couples which demonstrate the existence of a so-called "fast diffuser" were the first to show solid state reaction produced amorphous alloys. In order to obtain large amounts of material in a reasonable time, the value of the diffusion coefficient must be large enough even at the extremely low temperatures of the solid state reaction (see Fig. 5). This is another reason for the fast diffusers to be in an advantageous position.

"Anomalous fast diffusion" has been originally observed in crystalline materials. The model of the solid state reaction proposed by the author involves the assumption of diffusion through the bulk of the glass created during the reaction. It is this diffusion that must be fast. There is no proof that diffusion coefficients in the crystalline and amorphous states must be related. Nevertheless, the local atomic orders in glasses and crystals are very similar. This similarity can be used as an argument for an assumption that diffusion processes in glasses and crystals are basically the same. It should be even more so for the interstitial diffusion. All known fast diffusers diffuse interstitially. The lack of the long-range order should decrease the diffusion coefficient but should not eliminate fast diffusion completely. Diffusion is essentially a random walk. In glasses, the steps of this random walk are not directionally correlated as they are in crystals. But the probabilities of those steps in glasses and crystals should be nearly the same. That is the reason why the diffusion coefficients in glassy and crystalline states can be related.

There is a general lack of a good description for the interfaces derived from the first principles. The parameter κ which plays the most important role in the solid state reaction must be introduced as a phenomenological parameter. Because of this lack of physical models, a more detailed discussion of the criteria for the formation of an amorphous alloy during a solid state reaction is impossible at

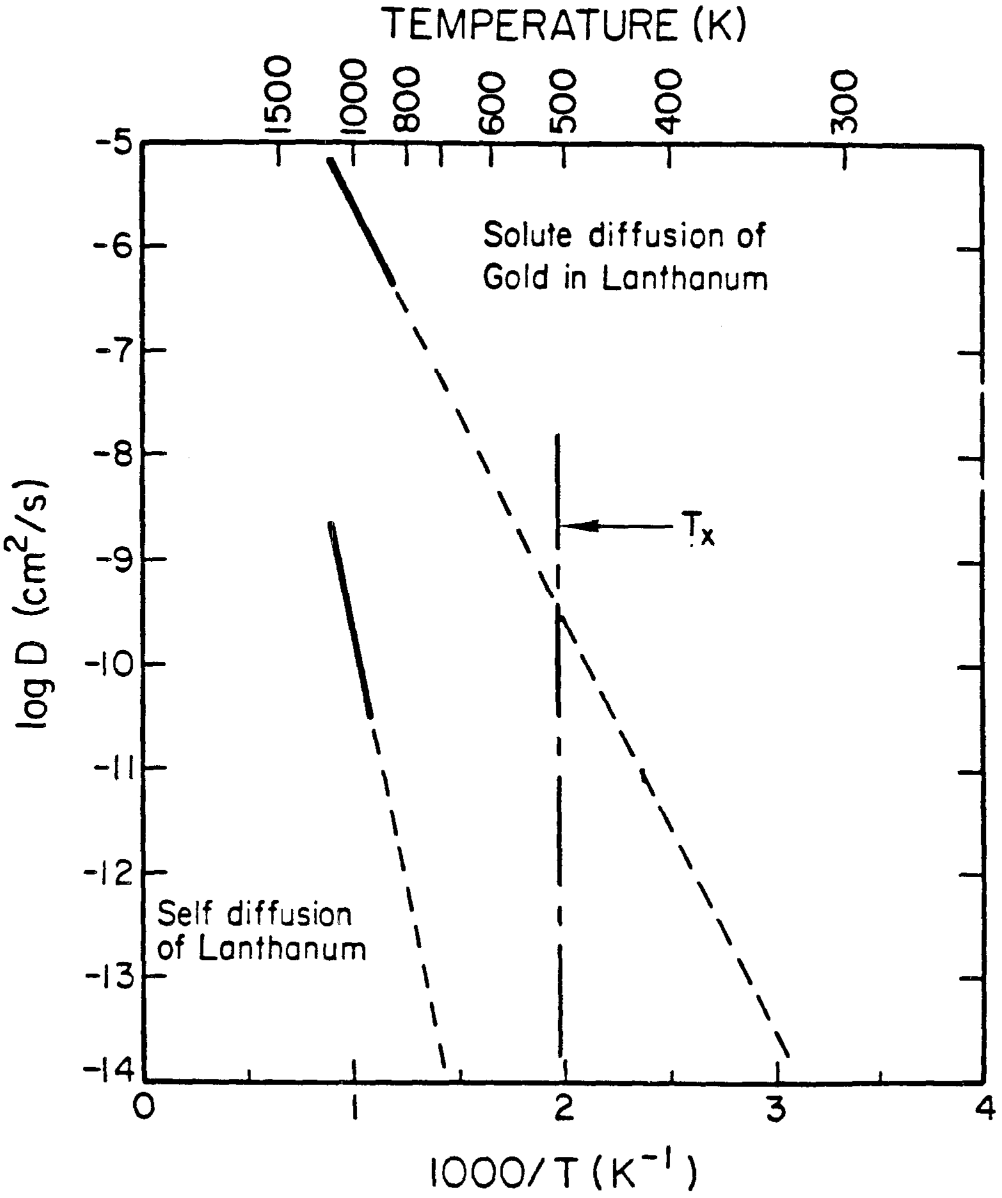

Fig. 5. Diffusion data for the diffusion of Au in La metal and self diffusion of La metal. Also shown is the approximate T_x of Au-La glass (after Ref. 17).

the current state of reseach.

II.2 THE THEORY OF DIFFUSION FLUXES.

The common chemical approach to diffusion[40] has to start with the Second Law of Thermodynamics. All permissible processes should be accompanied by a decrease of the Gibbs free energy of the reacting sample. The first approximation for the dynamics of the reaction would be to relate the rate of the reaction linearly with the change of the chemical potential. In the case of diffusion, this would be equivalent to writing:

$$\vec{J}_\alpha = - c_\alpha M_\alpha \nabla\mu_\alpha \tag{1}$$

where J_α is the flux of the specie α, c_α is the concentration of it in atoms per volume, μ is the chemical potential of the same component, and M_α is the linear constant which was introduced as the first approximation. In a general case, M_α should be a tensor. It is assumed to be a constant in order to simplify the arguments. In the theory of regular solutions, the chemical potential can be written in the form:

$$\mu_\alpha(c_\alpha) = \mu_\alpha^0 + k_B T \, \ell n(\gamma_\alpha c_\alpha)$$

and

$$\nabla\mu_\alpha = \frac{k_B T}{c_\alpha} \nabla c_\alpha + \frac{k_B T}{\gamma_\alpha} \frac{\partial \gamma_\alpha}{\partial c_\alpha} = \frac{k_B T}{c_\alpha} (1 + \frac{\partial \, \ell n \gamma_\alpha}{\partial c_\alpha}) \nabla c_\alpha \tag{2}$$

where k_B is the Boltzman constant, T is the temperature of the system, and γ_α is the activity coefficient. It is customary to relate the flux not to the change of chemical potential but to the gradient of concentration c_α

$$\vec{J}_\alpha = k_B T\ M_\alpha\ (1 + \frac{\partial\ \ell n \gamma_\alpha}{\partial\ c_\alpha})\ \nabla c_\alpha = -\ D \nabla C_\alpha\quad .$$

Parameter D is usually refered to as diffusion coefficient.

$$D = k_B T\ M_\alpha\ (1 + \frac{\partial\ \ell\ \gamma_\alpha}{\partial\ c_\alpha})$$

From the original definition (1), M_α is always positive. It is not true for the diffusion coefficient. The diffusion coefficient D can change its sign at the phase boundary. The diffusion coefficient can be negative at any point where the material can not be described by the ideal solution model.

A strict description of the interdiffusion of two materials into each other requires an introduction of three variables. They are concentrations of the components and the topological configuration of the mixed material. The latter is usually done by the introduction of vacancy fluxes. The fluxes of the interdiffusing species can be written in a form:

$$\begin{cases} \vec{J}_\alpha = -\ L_{\alpha\alpha} \nabla \mu_\alpha - L_{\alpha\beta} \nabla \mu_\beta \\ \vec{J}_\beta = -\ L_{\beta\alpha} \nabla \mu_\alpha - L_{\beta\beta} \nabla \mu_\beta \quad . \end{cases} \tag{3}$$

In this case, the flux of vacancies has to be $\vec{J}_v = \vec{J}_\alpha + \vec{J}_\beta$. There are general symmetry restraints applicable to the factors $L_{\alpha\beta}$. They are called Onsager relations. In the case of a two-component system, they are: $L_{\alpha\beta} = L_{\beta\alpha}$. From the fact that the sum of the concentrations is

$C_\alpha + C_\beta = 1$, one can get:

$$C_\alpha \nabla \mu_\alpha = - C_\beta \nabla \mu_\beta \quad .$$

A comparison of equation (1), (2), and (3) yields:

$$\vec{J}_\alpha = - RT \, (c_\alpha^{-1} \, L_{\alpha\alpha} - c_\beta^{-1} \, L_{\alpha\beta})(1 + \frac{\partial \, \ell n \gamma_\alpha}{\partial \, \ell n c_\alpha}) \, \nabla c_\alpha$$

and

$$D_\alpha = RT\Omega^{-1} \, (C_\alpha^{-1} \, L_{\alpha\alpha} - C_\beta^{-1} \, L_{\alpha\beta})(1 + \frac{\partial \, \ell n \gamma_\alpha}{\partial \, c_\alpha}) \quad . \tag{4}$$

The factor Ω is introduced to convert the concentrations in atoms per volume into the ones which change from 0 to 1.

The vacancy flux represents the movement of the sample as a whole. This part of the diffusion does not represent any mixing of the components. Because the mixing is the subject of the discussion, it is reasonable to choose a reference system in which this flux is equal to zero. In this system,

$$\vec{J}_\alpha = \vec{J}_\alpha - \vec{J}_v = C_\beta \vec{J}_\alpha - C_\alpha \vec{J}_\beta \quad . \tag{5}$$

From equations (4) and (5)

$$\vec{J}_\alpha = (C_\alpha D_\beta + C_\beta D_\alpha) \, \nabla C_\alpha \quad .$$

In the center of mass system, the diffusion equation can be written in a form

$$\vec{J}_\alpha = - D \, \nabla C_\alpha$$

where

$$D = (C_\alpha D_\beta^o + C_\beta D_\alpha^o)(1 + \frac{\partial \, \ell n \gamma_\alpha}{\partial \, \ell n c_\alpha}) \tag{6}$$

where D^o are defined as:

$$D_\alpha^o = RT\Omega^{-1} \left(C_\alpha^{-1} L_{\alpha\alpha} - C_\beta^{-1} L_{\alpha\beta}\right) \quad .$$

The latter can be measured in the experiment in the dilute solution of material α in material β. Usual experimental data contain measurements of D^o as opposed to D. Figure 5 is an example of such measurements. This form of the diffusion coefficient, introduced in the equation (6), will be used later in the model of the solid state reaction.

The total amount of atoms α and β must be conserved. The condition of the conservation of species can be written in a form:

$$\nabla\vec{J} = -\frac{\partial C}{\partial t} \quad . \tag{7}$$

A substitution of the flux equation in equation (7) leads to

$$\frac{\partial C}{\partial t} = \nabla(D\nabla C) \; .$$

This is the diffusion equation which must be solved for a given set of initial and boundary conditions and geometry.

III. EXPERIMENTAL TECHNIQUES.

III.1 SAMPLE PREPARATION.

Thermal vacuum evaporation is the most suitable technique for the sample preparation for the La-Au system. Since tungsten evaporators do not react with either of the two metals, one can utilize fully the advantages of the method. The vacuum chamber for the thermal vacuum evaporation is the most simple and inexpensive to build. All the other alternatives (sputtering, e-gun evaporators, etc.) require expensive power supplies and elaborate feedthrough systems. Thermal evaporation permits *in situ* La purification. It was discovered that oxygen-free lanthanum is one of the most crucial ingredients of the solid state reaction. Lanthanum purification becomes a major problem for every method except the thermal evaporation. All the above arguments make thermal evaporation the choice for Au-La system.

All of the details of the experimental setup, including the vacuum chamber, the feedthroughs, and the power supplies, were designed by the author. The generalized view of the vacuum system is outlined in Fig. 6. The system has 4 evaporators. Each can be heated independently. The shutter does not permit more than one of the evaporators to be exposed to the samples at any given time. The shutter and the evaporators′ geometry is shown in Fig. 7. The sample holders have thermal pumps attached to them. The thermal pumps are

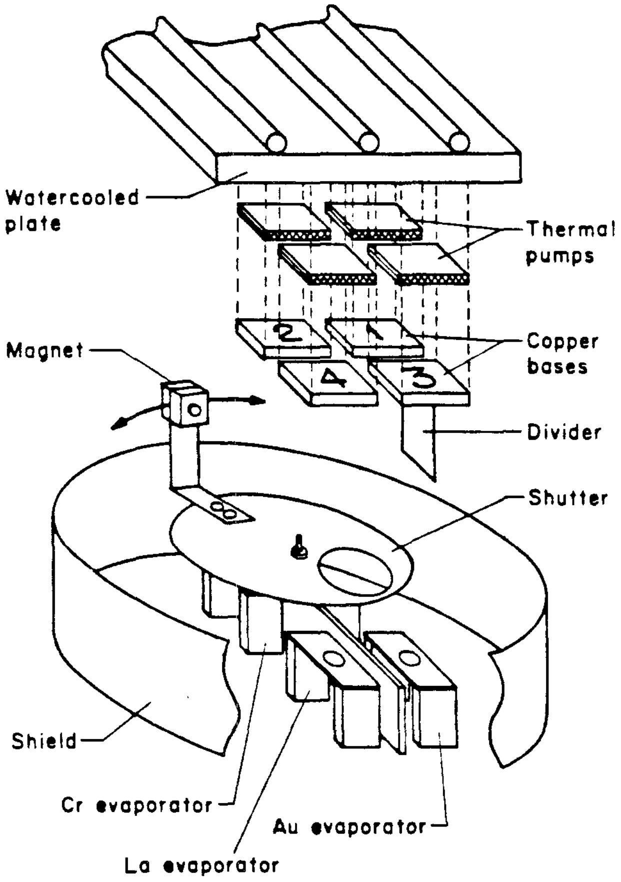

Fig. 6. Generalized view of the vacuum chamber.

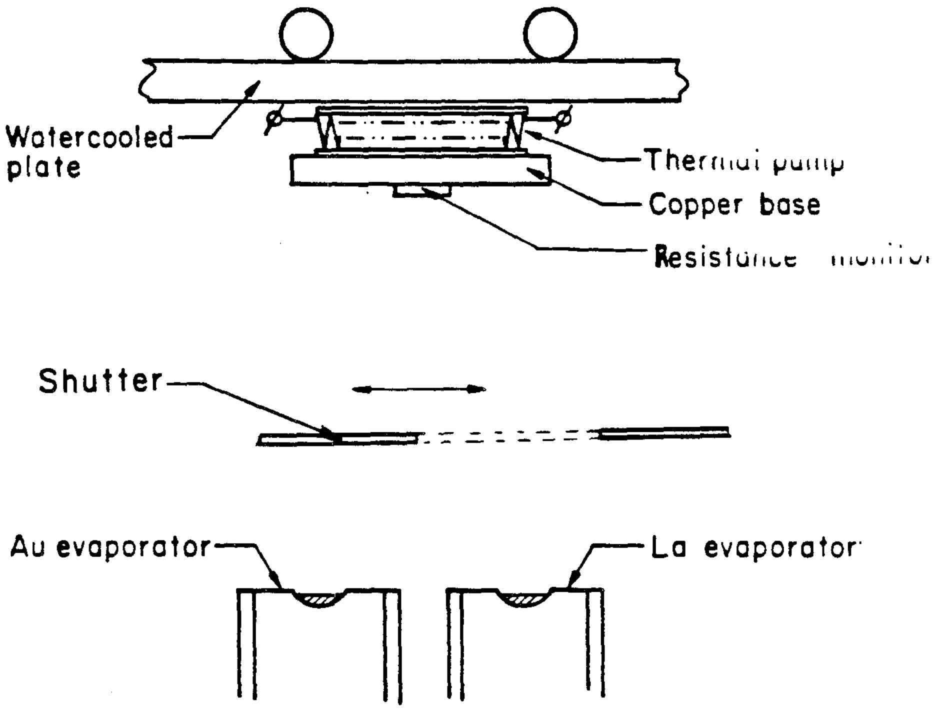

Fig. 7. Schematic diagram of the multilayer sample preparation.

Peltier effect heaters/coolers. They permit control of the temperature of the samples in the temperature range from -15 to +150 C. All of the temperatures were measured by chromel-alumel thermocouples. The reference point thermocouple was immersed into the melting ice. One of the sample holders (position #3 in Fig. 6) had a divider installed. This position was used as a thickness monitor. The geometry of the thickness monitor is described in Fig. 8. The thickness monitor for La is exposed to the lanthanum source only. The other evaporator is blocked from the thickness monitor by the divider. The Au thickness monitor is positioned similarly. This design permits independent monitoring of the total amount of each of the elements. The geometry of the resistance monitor itself is described in Fig. 9. The gold contact strips are evaporated on the pyrex slides in a separate evaporation. The contact wires are attached by a soft solder. The set of resistors R_1, R_2 ... controls the current through the monitors. The current increases 2, 3, 4, ... times when the switch connects resistors R_2, R_3, R_4, ... into the circuit. The reading of the voltmeter V (Fig. 9) is proportional to the resistance of the monitor. The readings of this voltmeter at the end of the evaporation of each layer were maintained constant. This constant voltage corresponds to the constant resistance of the layers. Conductivity of the bulk materials is proportional to their thickness. For the bulk materials, the constant resistance corresponds to the constant thickness of the layers. The calibration of the homemade monitor is described later. The calibration proved that the relation between the thickness of the layer and its resistance is close to being linear. Resistor R_{sh} (see Fig. 9) is introduced in order to limit the maximum current density in

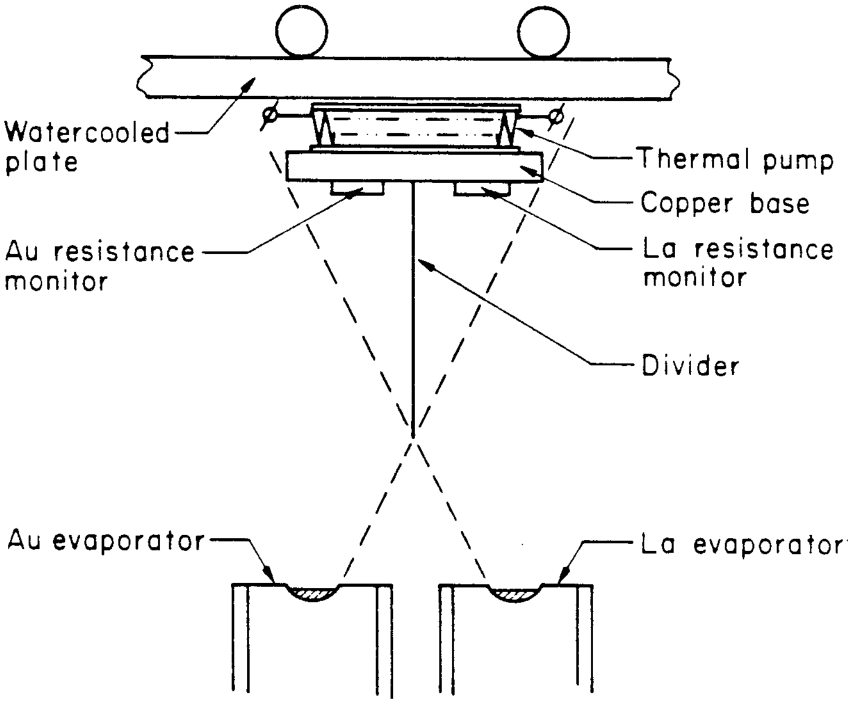

Fig. 8. Schematic diagram of the geometry of the thickness monitor.

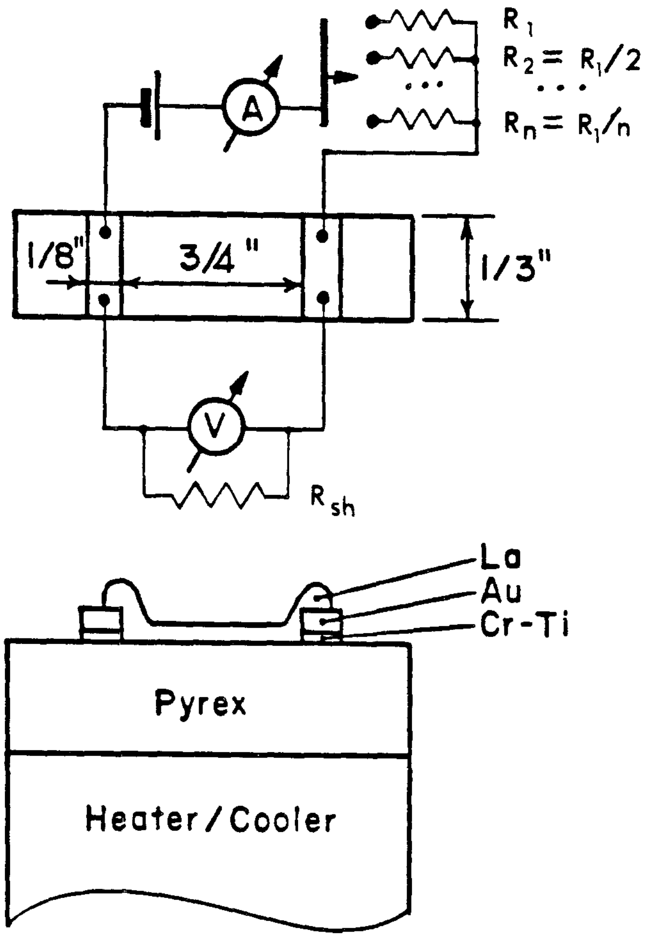

Fig. 9. Block diagram of the resistance monitor for the thickness measurements.

the film of metal growing on the monitor.

The structure and therefore the resistivity of evaporated material is strongly influenced by the temperature of the substrate on which it is evaporated. Lanthanum has two crystalline phases which are referred to as α- and β-lanthanum. It was found from the X-ray studies that the amount of α-La increases dramaticaly when the temperature of the substrate grows higher than -5 C. Resistance of the lanthanum layer, evaporated on the substrate which is kept at +10 C, can be 4-8 times higher than resistance of the same amount of lanthanum, evaporated on the substrate kept at -10 C. Gold does not demonstrate such a significant dependence of resistance on the temperature of the substrate. Still, the difference of the resistance of Au films evaporated on the +10 C and -10 C substrate can be as much as 50%. Annealing even at low temperatures can eliminate this difference in resistance for gold samples. Lanthanum films do not anneal at low temperatures. Calibration curves for the weight of evaporated gold and lanthanum as functions of the conductance of the standard resistance monitor are reproduced in Fig. 10. To obtain the curves, the metals were evaporated on the 1.5"x1" pyrex slides. The weight of the evaporated films was found by weighing the slides before and after the evaporation. The bulk density was used in the conversion from weights to thicknesses.

The samples for the solid state reaction are multilayers of alternating gold and lanthanum. The ingredients were evaporated on the substrates kept below -5 C. During the evaporation, the vacuum was better than 10^{-6} torr. Schwarz and Johnson[11] found that α-La hardly produces any solid state reaction at all. In order to increase the

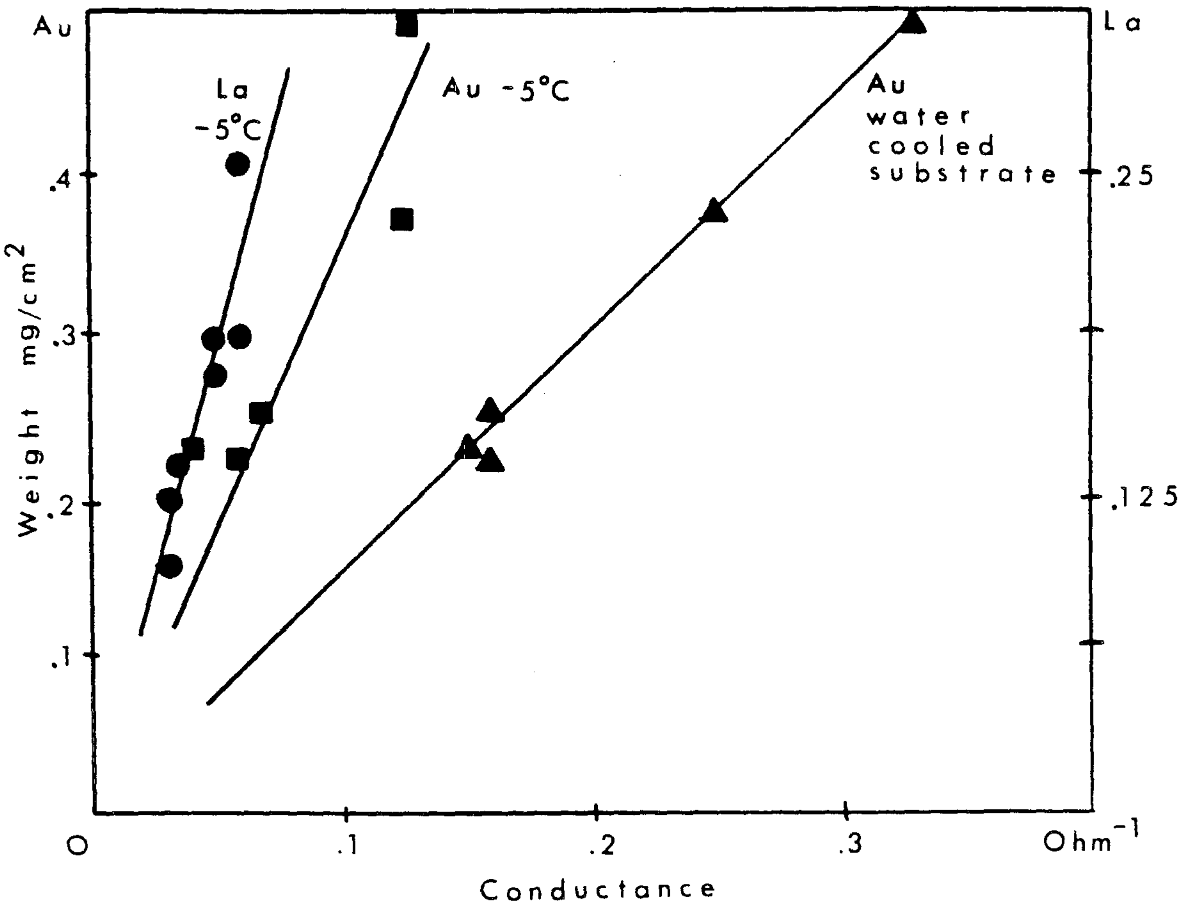

Fig. 10. Calibration curves for the thickness monitor: a) La film, b) Au film on +10 C substrate, c) Au film on -10 C substrate.

ratio of β-La to α-La in the evaporated films, the vacuum in the system must not drop below $1.5\cdot10^{-6}$. The La source must be cleaned and the vacuum system must be baked to insure such a degree of cleanliness. Lanthanum ingot must be melted in the tungstun evaporator and kept in the liquid state for at least 4 hours in order to purify lanthanum. The vacuum system was usually baked at the same time. The samples were kept at 150 C during baking. This high temperature prevents condensation on the substrates and keeps them clean. The sample holders were never cooled down earlier than 10-15 minutes before the evaporation.

The actual geometry of the evaporated layers was different for different experiments. The number of layers and their thickness were chosen to fit the requirements of each experiment. In the thesis, the description of the geometry of the sample and the temperature of the thermal treatment accompany the description of every experiment introduced.

III.2 THERMAL TREATMENT OF THE SAMPLES. RESISTANCE CURVES.

The thermal treatment of the samples consisted of heating the samples and keeping them at a predetermined temperature for a period of time. It would take 1/2 a minute to heat up the substrate to the temperature of 70 C. The maximum treatment temperature of 120 C could be achieved in 1.5 minutes. The resistance of the samples was monitored constantly during thermal treatment. The block diagram of the experiment is the Fig. 11. The sawtooth generator had a repetition period of approximately 15 minutes. The output signal from

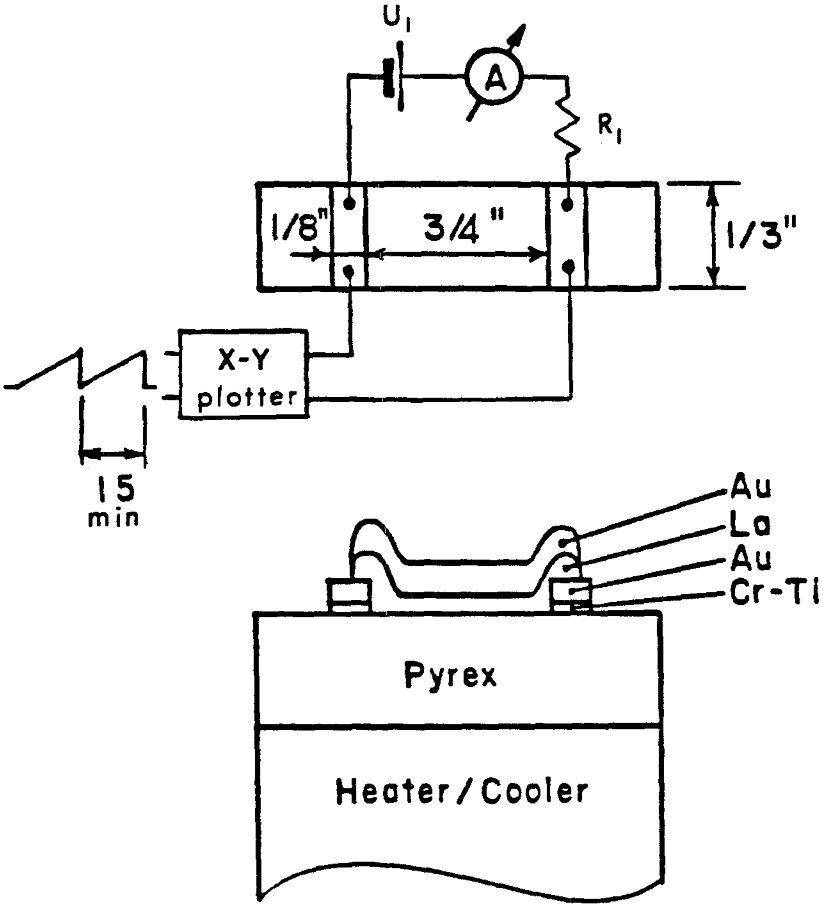

Fig. 11. Block diagram of the resistance measurements of the reacting multilayers.

the generator was applied to the X input of the X-Y plotter. The voltage across the sample was applied to the Y input of the plotter. This voltage is proportional to the resistance of the sample. A typical trace produced by the plotter during the thermal treatment is reproduced in Fig. 12. All the resistance curves were digitized and saved in the computer memory.

III.3 SIMS MEASUREMENTS.

Secondary Ion Mass Spectroscopy is a method which analyzes the ionized atoms sputtered from the surface of the sample. An ion gun mills away one layer of the sample after another. Some of these sputtered atoms get ionized and can be detected by usual techniques of mass spectroscopy. The described process enables the researcher to obtain a concentration vs. depth profile of the analyzed sample.

A block diagram of the SIMS set up used in the study of La-Au samples is reproduced in Fig. 13. An ion gun (a) produces a beam of primary ions (Cs^+ in our case) which sputters away the surface of the sample (b). The ion gun consists of the Cs source (a_1), dua-plasmatron ion beam source (a_2) and focusing system (a_3). The energy of the Cs ions is determined by the potential difference U_2-U_1. This energy controls the sputtering rate if all the other factors remain constant. Sputtered (secondary) ions go through the drift chamber (c) and become accelerated and focused by the system of electrodes (d and e). The energy of the secondary ions is determined by the potential U_1. The 90 degree electrostatic energy monochromator (f) sorts out the ions with "wrong" energies. The contrast diaphragm (g) determines the

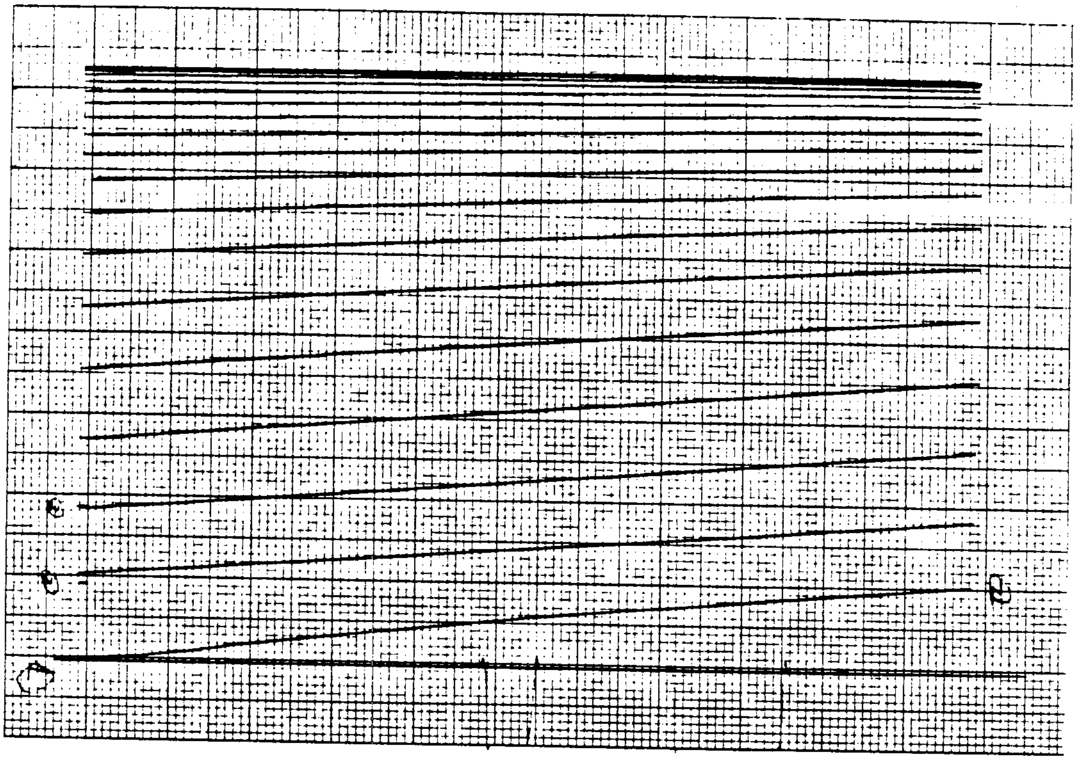

Fig. 12. Typical trace produced by the X-Y plotter during the thermal treatment of a sample (see description in the text). The treatment was started at the begining of the first sweep.

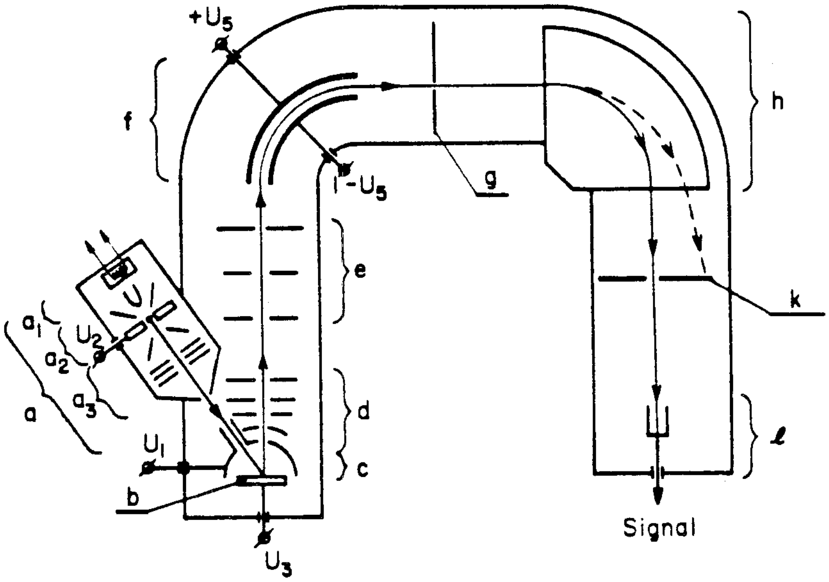

Fig. 13. Block diagram of the SIMS analyzer. See description in the text.

input beam of the 90 degree magnetic mass spectrometer (h). The field aperture (k) selects ions with required mass to charge ratio. The dashed line in the diagram shows the trajectory of the atoms with "wrong" charge to mass ratio. The detector (l) counts the amount of ions which passed through the analyzer.

The potential at the sample U_3 is not equal to the potential of the drift chamber. The electrical bias U_3-U_1 is applied to the sample. This bias prevents organic composites, with the same charge to mass ratio as the element in question, from going through the analizer. The SIMS unit is controlled by a microprocessor which permits the switching of the values of the sample bias and the magnetic field, so that several different elements can be traced simultaneously during the same run.

SIMS measurements are an extremely powerful analytical tool in the case of diluted impurities with concentrations below 0.1%. In the case of a La-Au system when the concentrations change from 0 to 100%, quantitative results are hard to obtain. The rate of sputtering and the yield of secondary ions both depend upon the current concentration of the analyzed material and the amount of dissolved oxygen. SIMS measurements were used to confirm some topological properties of the solid state reaction.

III.4 X-RAY SPECTROSCOPY.

The geometry of an X-ray spectrometer is described in the Fig. 14. The sample is being exposed to the beam of X-ray. The

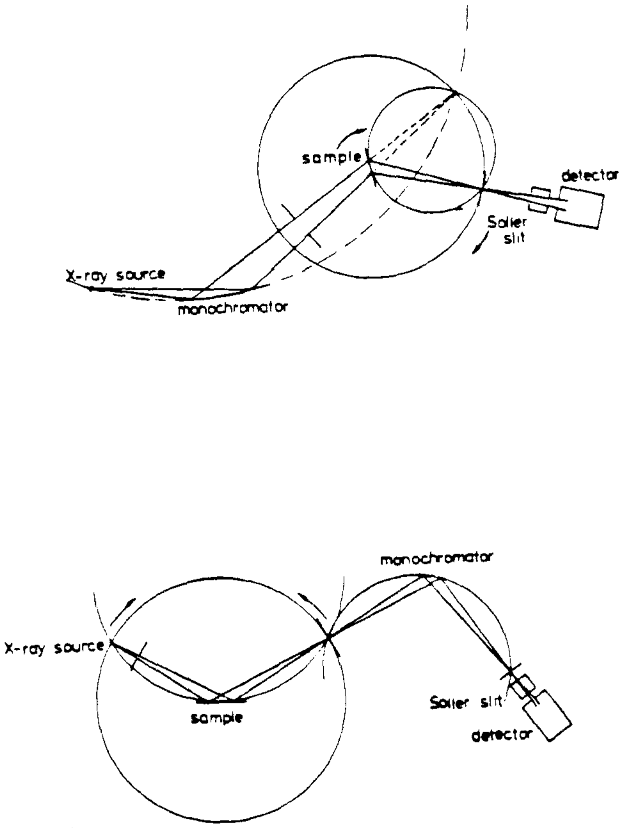

Fig. 14. Block diagram of the X-ray spectrometer (from Ref. 39). a) Symmetrical transmission geometry with the reflected beam monochromator. b) Symmetrical transmission geometry with the incident beam monochromator.

intensity of the reflected beam as a function of the scattering angle is measured by the detector. A monochromator is introduced in the beam to fix the wave length of the radiation.

The simplified theory of diffraction can be described in terms of the atomic density correlation functions[24]. Let us introduce an atomic density function:

$$p_N(r) = \sum_{m=1}^{N} \delta(\vec{r}-\vec{r}_m) \ ,$$

where $\delta(\overline{r})$ is the Dirac delta function and $\vec{r}_m$ is the position of the "m-th" atom. If the incident beam is a plane wave with a wave vector $\vec{k}_1$, then the amplitude of the scattered plane wave with the wave vector $\vec{k}_2$ is proportional to

$$\sum_{m=1}^{N} f_m(\vec{\Delta k})\exp(i\vec{k}_2\vec{r}-i\vec{\Delta k}\vec{r}_m) \ ,$$

where $\vec{\Delta k}=\vec{k}_2-\vec{k}_2$ is the change of the wave vector and $f(\vec{k})$ is a scattering amplitude for the atom "m". One scattering process assumption and several other simplifications are included in this derivation.

All physically possible detectors measure the intensity of the scattered radiation. The intensity is equal to the square of the amplitude. Simple calculations lead to the following expression:

$$I(\vec{\Delta k}) = I_o \sum_{m,m'}^{N} f_m f_{m'} \exp[i\vec{\Delta k}(\vec{r}_m-\vec{r}_{m'})] =$$
$$= \int d^3\vec{r} \exp(i\overrightarrow{kr}) \int d^3\vec{r}_1 p_N(\vec{r}_1) p_N(\vec{r}_1-\vec{r}) \ ,$$

where I_o is the incident beam intensity. The integral in this equation is a Fourier transform of the density correlation function. The latter is usually referred to as Radial Distribution Function (RDF). The ratio $I(\vec{\Delta k})/I_0$ is called the Interference Function. If the sample studied has a long-range order (crystalline material), then the RDF must have singularities at the values of the distance which correspond to the correlation length for the sample. Fourier transformation converts these singularities into peaks with an extremely high value of the Interference Function. As a result, the observer should see a peak in the diffraction pattern at an angle which corresponds to this value of $\vec{\Delta k}$. The lack of the long-range order in the amorphous materials should prevent the existence of any sharp peaks. The diffraction pattern must be significantly more diffused.

The presence of peaks in the diffraction spectrum of the material does prove that the material is crystalline. The absence of sharp peaks in the X-ray diffraction pattern is not a proof of the fact that the material is amorphous. A microcrystalline material with extremely small crystallites can produce a similar pattern. The widening of the peaks due to the small crystallite size can blur the peaks. If the area illuminated by the primary beam is large, then the microcrystalline and amorphous samples become even less distinguishable. A large area would lead to averaging over different orientations of the crystallites, etc. If the size of the crystallites is smaller than 20-30Å, then the X-ray spectroscopy is unable to distinguish this material from an amorphous one.

The arguments which lead to the conclusion that a diffraction pattern of a crystal must have sharp peaks does not take advantage of some special properties of X-rays. In fact, the arguments are true for any type of radiation. Electron diffraction gives one a possibility to illuminate an extremely small area of the sample and to detect scattering in all directions in space simultaneously. It is a much more sensitive tool to detect small crystallites and to distinguish between microcrystalline and amorphous samples.

III.5 TRANSMISSION ELECTRON MICROSCOPY.

A Transmission Electron Microscope[25] is a direct equivalent of an optical microscope; but it uses a beam of electrons instead of a beam of light. An Electron Microscope consists roughly of three important parts. First, the illumination system consists of an electron gun and condenser lenses. This system is responsible for the "illumination" of the sample with a high flux electron beam. In the case of diffraction studies, this part is responsible for defining some finer properties of the beam. Convergence and coherence of the incident beam are determined by the illumination system. Second is the objective lens. This lens is located immediately after the specimen. It produces the first magnified image of the specimen and its diffraction pattern. The objective aperture separates the objective lens from the following lenses. This aperture determines what type of electrons (transmitted or diffracted) would reach the screen which is seen by the observer. Third is the magnification system. This system magnifies the first image and produces the final image of the specimen. The ray diagrams for the major methods used in TEM are summarized in Fig. 15.

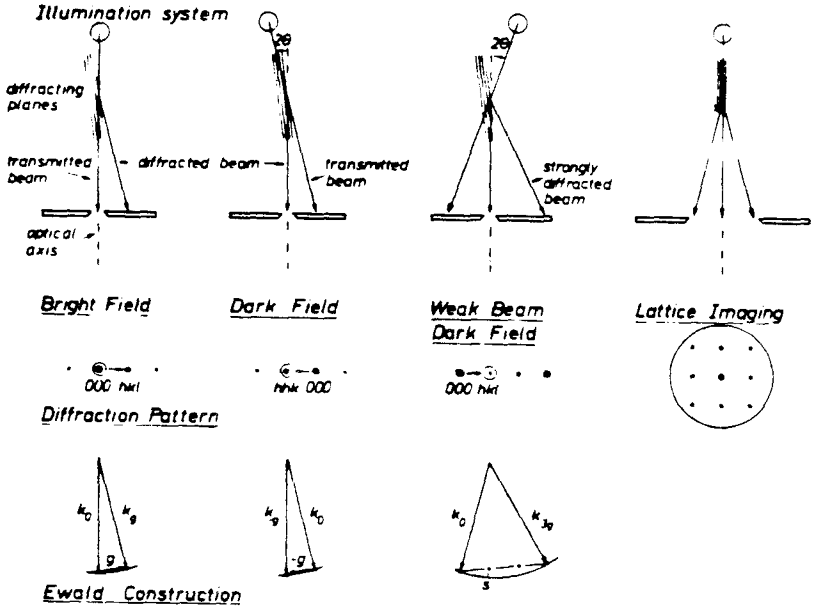

Fig. 15. Ray diagrams (including Ewald sphere construction) for a) conventional two-beam bright field image, b) Dark Field image, c) Week Beam Dark Field image, d) Lattice image (from Ref. 25).

III.6 RUTHERFORD BACKSCATTERING.

Schematic diagram of a typical backscattering spectrometer[26] is reproduced in Fig. 16. The accelerator generates a beam of α particles. The focusing system, the magnetic analyzer and the set of slits are designed to make the beam monochromatic and collimated. In the scattering chamber, the α particles scattered by the sample are intercepted by the detector. The design of the latter permits one to measure the energy of the reflected particles. The rest of the electronics is designed to reduce the signal-to-noise ratio by accumulating a high number of the scattering events.

In order to understand the relation between the energy losses and the concentration profiles in the analyzed sample, one can use the following simplified description of the process. There are two mechanisms responsible for the energy losses of the α particles. They are associated with a small and a large angle scattering. On its way through the sample an α particle slowly loses energy due to the small angle scattering. In order to be detected by the detector, at one point in time a large angle scattering must take place. The particle has to be scattered at an angle comparable to 180°. This process can be nearly adequately described as a hard sphere collision. The energy loss at this collision depends upon the ratio of the masses of the α particle and the atom involved in the collision. This dependence permits different atoms to be distinguished. On the way out of the sample the small angle scattering mechanism takes its toll of the energy loss. Both of the mechanisms of the energy losses are well

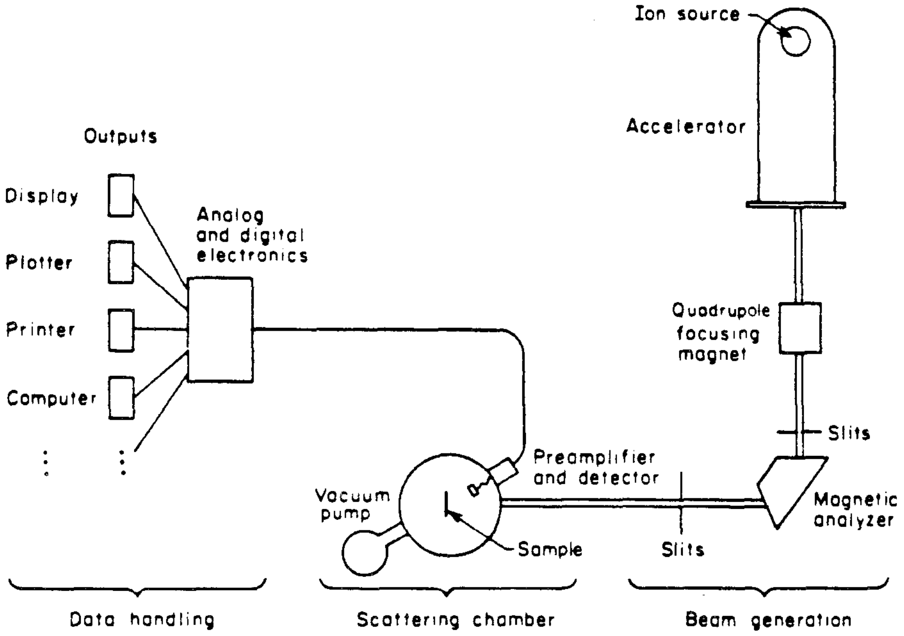

Fig. 16. Schematic diagram of a typical backscattering spectrometry system (from Ref. 26).

studied and described. From the presented description, it is obvious that the value of the energy loss carries the information on both the depth of the collision and the mass of the atom at this depth. Introduction of some assumption about the density of the sample permits the deconvolution of the real concentration depth profile from the intensity vs. energy loss data.

All the Rutherford Backscattering data used in this theses were obtained and deconvoluted by Dr. Mark Van Rossum. The author in collaboration with Dr. Van Rossum made a comparison between the concentration depth profiles and the prediction for these profiles derived from the model for the solid state reaction. This model was introduced by the author and Prof. W. L. Johnson[22].

IV. EXPERIMENTAL RESULTS.

IV.1 RESISTANCE MEASUREMENTS.

The sample preparation is described in Ch. II.1. The samples for resistance measurements were multilayers with 2, 3, 5 and 7 layers. The top layer was always gold. The bottom layer was usually a lanthanum layer. Several 3 layer samples had a thin layer of the mixture of Cr and Ti at the bottom. The bottom layer of lanthanum for 3, 5, and 7 layer samples was made extremely thin. Its main purpose was to insure the adhesion of the sample to the pyrex substrate. Usually, the total ratio of La to Au was approximately 1:1.

Typical data showing the dependence of resistance vs. time for any of the samples described above are shown in Fig. 17. The resistance increases initially at a finite rate. Typical thermal treatments were found to produce little change in the resistivity of a pure La film. On the other hand, Au films exhibit as much as a 50% decrease in resistance following the thermal treatment. This decrease was discussed in more detail in Ch. II.1 in connection with the thickness monitor calibration. The latter decrease occurs on a rather short time scale by comparison with the reaction to form amorphous layers. In Fig. 12, this decrease can be seen near the point of onset of the growth of resistance. Because of the difference in the time scales, the effects can be separated easily. No delay between the start of the heat treatment of the sample and the onset of the increase in resistance was found; at least on the time scale longer

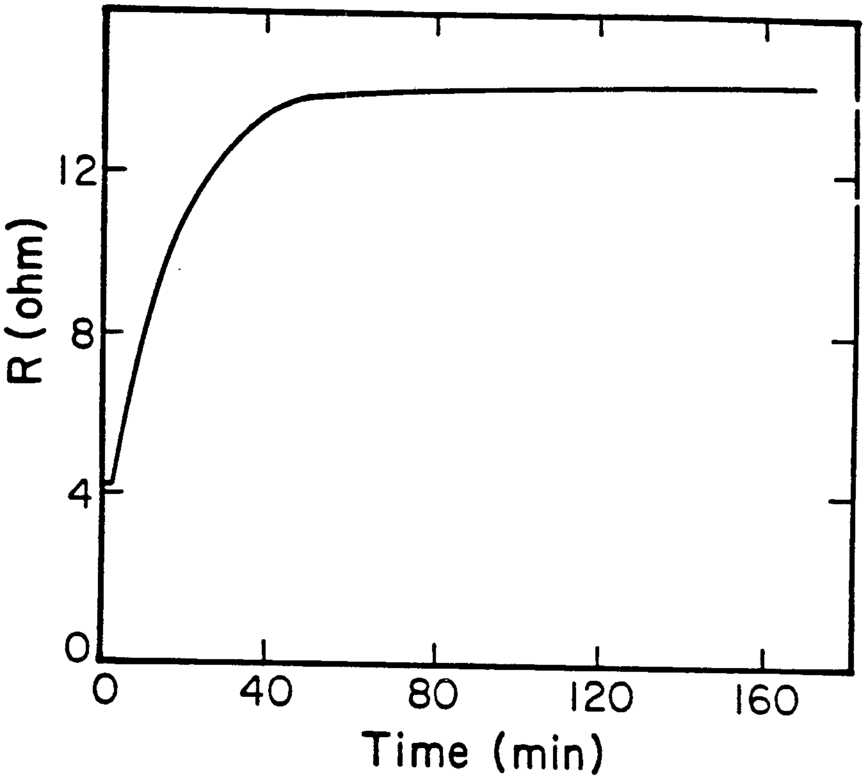

Fig. 17. Resistance of the sample # 14.3 vs. time. Thethermal treatment temperature is 95 C. Layers' thicknesses are: La - 1600 Å, Au - 1000 Å.

than 15-30 seconds. This interval can be as small as 1/500 of the time scale of the reaction process for lower temperatures. Figure 12 is a good illustration of this lack of the delay time.

Plots of the time dependence of the conductance of the samples were made. The major feature of these plots was the fact that the rate of change of the conductance at the beginning of the heat treatment does not depend on the thickness of the La or Au layer. This rate depends only on the temperature. The validity of this claim is confirmed by Fig. 20 which is discussed in the next paragraph. Even for the reactions taking place on the scale of several hours no abrupt changes of the rate of growth during first several minutes of the treatment were found. A typical plot of conductance vs. time is reproduced in Fig. 18. All attempts to fit the time dependence of the resistance or the change of conductance to a $t^{1/2}$ law were unsuccessful.

Logarithmic plots of the conductance minus the value of the conductance at the end of the reaction have shown the existence of two time constants describing the process. One time constant characterizes early stages of the reaction. A second one describes the later stages. The typical dependence is shown in Fig. 19. These two time constants were determined for a large number of runs done for different geometries of the diffusion couple. The following configurations of layers were studied: bilayer (one La and one Au), trilayer (Au-La-Au), and multilayer (Au-La-Au-La-Au) with a constant (1500 Å) thickness of La and varying Au thickness; and bilayer samples with different (800, 1500, 2500 Å) thicknesses of La and a constant

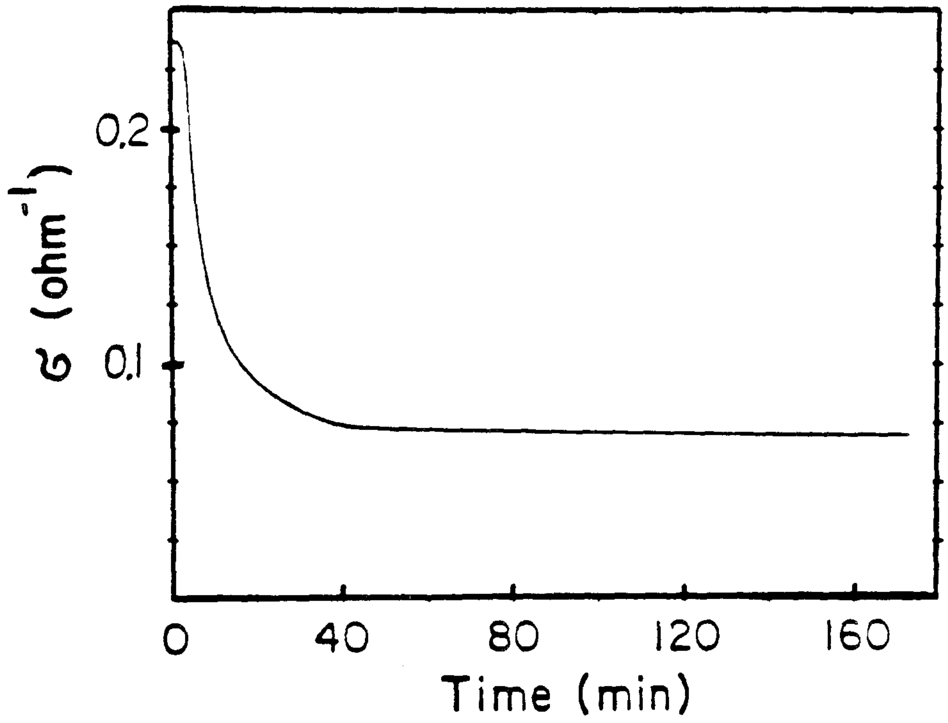

Fig. 18. Conductance of the sample # 14.3 vs. time. The thermal treatment temperature is 95 C. Layers' thicknesses are: La - 1600 Å, Au - 1000 Å.

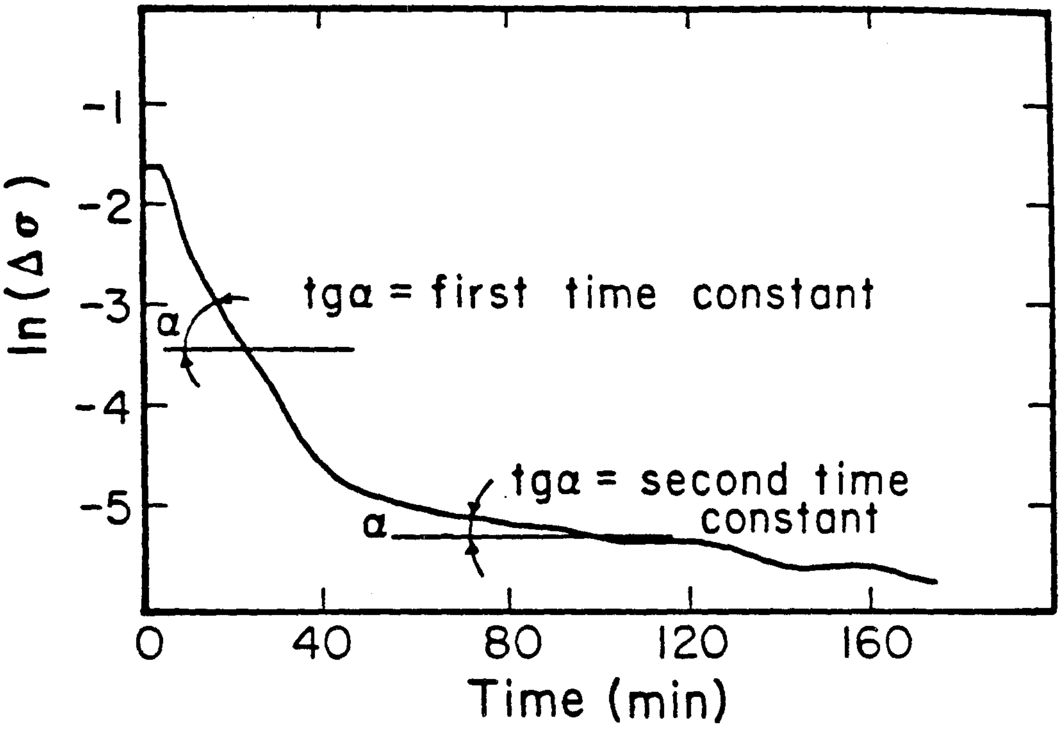

Fig. 19. Difference Δσ between conductance at time t and final conductance after long thermal treatment vs. time for the sample # 14.3. Time constants are the first and the second time constants described in the text.

(1000 Å) amount of Au. Multilayer samples had a thin sublayer of Cr-Ti or La. The samples with Cr-Ti sublayers and bilayers confirmed that the second time constant was intrinsic to the reaction and could not be caused by the difference in the thickness of multiple reacting layers. Only one factor was observed to influence the value of the first time constant. This factor was the temperature of the thermal treatment. An Arrhenius plot of these time constants is reproduced in Fig. 20. Each point on the graph corresponds to one measured sample. The Arrhenius plot shows that the dependence of the time constants on the temperature can be characterized by an activation energy. The value of this activation energy is close to that for the diffusion coefficient of Au in crystalline La, as indicated in Figure 20. The geometry and the ratio of La and Au were found to have only a small influence on the first time constant. The second time constant, in contrast, was observed to depend somewhat more strongly on these factors.

IV.2 MICROSCOPIC STUDIES.

The samples for the microscopic studies were trilayers with an La layer in between two Au layers with the total ratio of Au to La being approximately 1:1. This three-layer geometry permitted an easier separation of the reacted film from the pyrex substrate since the adhesion of Au to pyrex is comparatively poor. The total thickness of the samples for the microscopic studies was estimated by resistance measurements to be 300-500Å. During the thermal treatment, the resistance of these samples increased up to 9 times, which is larger

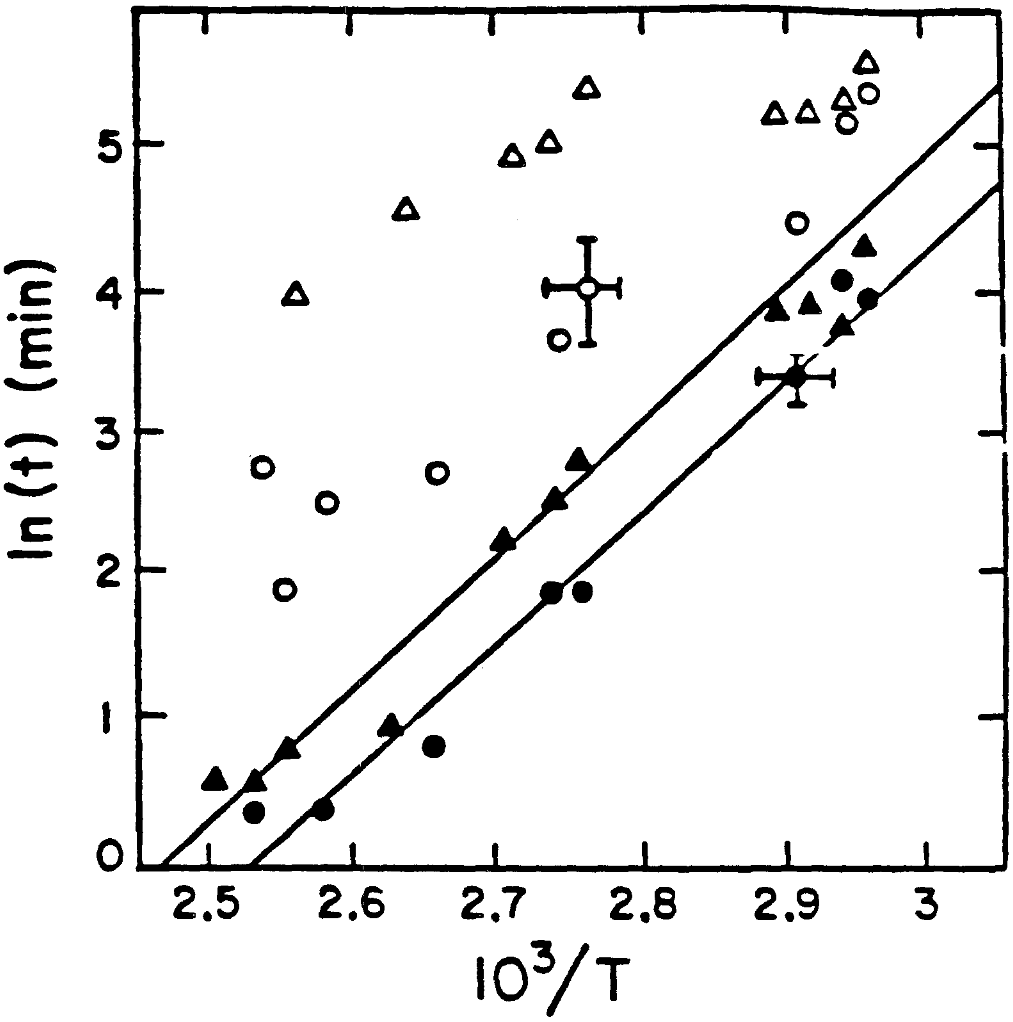

Fig. 20. Logarithm of the time constants defined in the text vs. 1/T. ● and ○ are the first and the second time constants for the bilayers. ▲ and △ are the same for trilayers. The thickness of La layer is 1600 A for all the samples. Total thickness of Au is 1000 A. The slope of the lines in the graph corresponds to the activation energy of the diffusion coefficient from Ref. 36.

than a usual increase for the thicker samples used in resistance measurements. The resistance of the latter grows approximately 4-6 times. The temperature of the thermal treatment was 100 C. The samples were then annealed in a vacuum for 15-20 hours at 120 C to be certain that all of the processes of equilibration occurred.

The pictures of the reacted trilayer taken through an optical microscope are reproduced in Fig. 21. The film looks as if it "bubbled up." The scale of the bubbles goes all the way from fractions of a centimeter down to fractions of a micron. Fig. 22 shows a picture of a characteristic crack taken through an electron microscope. It was checked under the optical microscope that the "bubbled" regions have been raised off the substrate. The narrow "folds" in the boundary regions are depressed. The "folds" around the large "bubbles" do not necessarily touch the substrate. The whole structure can be raised as high as several millimeters. The "folds" around small bubbles are in contact with the substrate. The monitor samples which were exposed to Au or La sources exclusively do not show any "bubbling" even on the thick samples. It must be emphasized that the peeling of the films is not due to the thermal cycling. The peeling of the thin and sometimes even of the thick samples could be observed while the samples were still reacting and before they were cooled down. The thickness monitors did not show any "bubbling" at all. The thick samples, which were used in the resistance measurements had a bottom layer designed to increase adhesion (Cr-Ti or La was used for the purpose). Because of that layer these films usually would not peel off, but they would crack. The crack pattern of the thick films looked identical to the

Fig. 21a. Reacted trilayer. Figure 21b and 21c are the areas in the top and the bottom of the Fig. 21a reproduced with higher magnification.

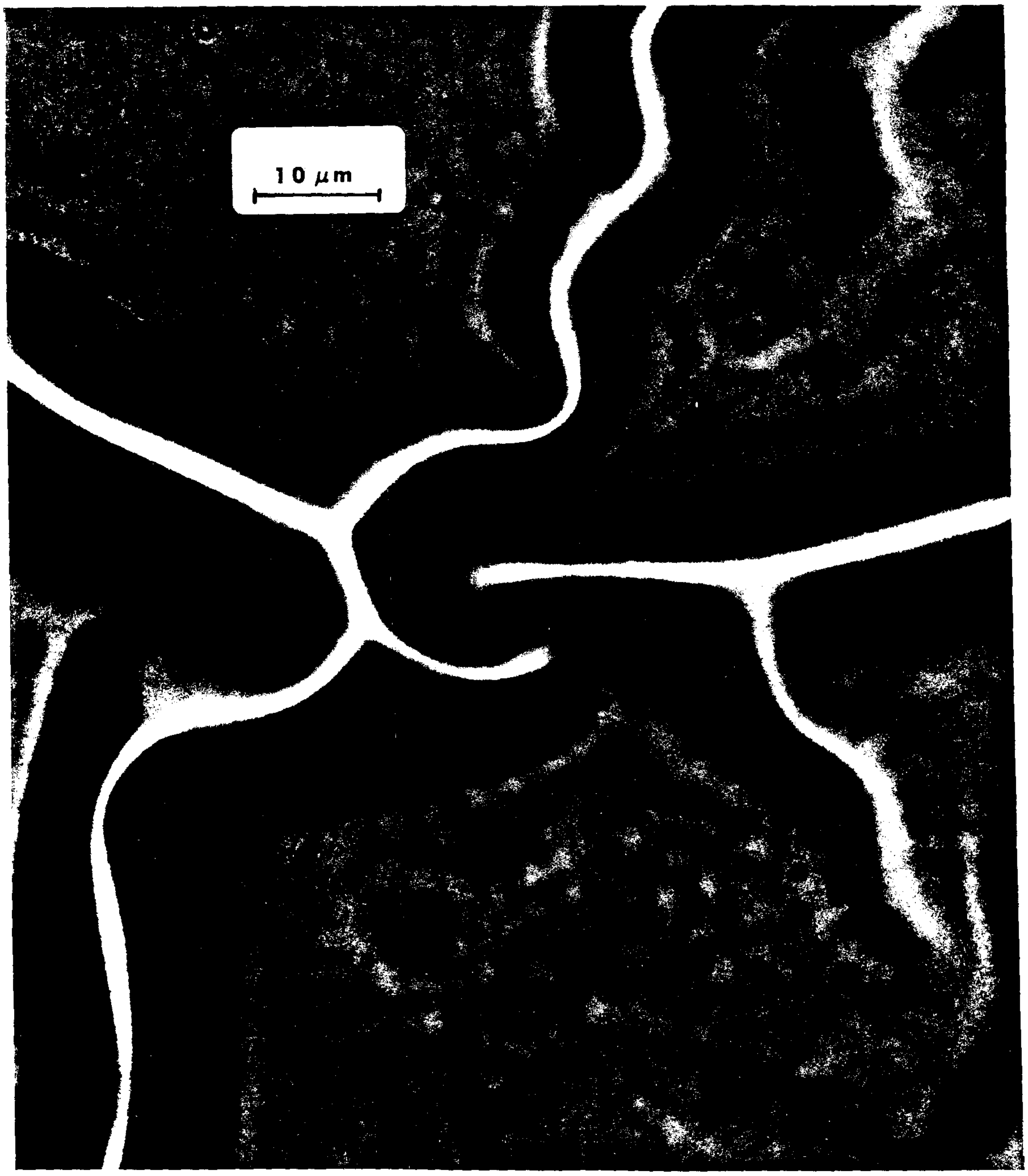

Fig. 21b. Reacted trilayer. Figure 21b and 21c are the areas in the top and the bottom of the Fig. 21a reproduced with higher magnification.

Fig. 21c. Reacted trilayer. Figure 21b and 21c are the areas in the top and the bottom of the Fig. 21a reproduced with higher magnification.

crack pattern of the thin layer in Fig. 21b. In the thick samples, this crack pattern would become apparent only at the second stage of the reaction. The monitor samples, and the samples reacted for a short time only, did not show any cracks observable through an optical microscope. After a 4-5 hour exposure to air, the thick samples would peel off. The presence of a thin blue layer of lanthanum oxides would be detected on the bottom.

The TEM micrographs of the reacted samples are reproduced in Fig. 23. Comparison between the pictures of the sample after 20 and 100 minute exposure to air shows significant differences in the amount of cracking (white spots). The size of the grains changes from 100 Å, far from the cracks, to several hundred angstroms near the cracks. Figure 24 shows the diffraction pattern for the sample. The diffraction pattern did not depend on the area of the sample selected. The radius of the illuminated area for the diffraction pattern was approximately 2000 Å (see Fig. 25).

IV.3 CRYSTALLIZATION TEMPERATURE.

Amorphous materials are characterized by a glass transition temperature T_g. Direct measurements of T_g utilize differential scanning calorimetry. These measurements are difficult to perform in the case of the La-Au system because the weight of a typical sample is less than two milligrams and the shelf life of a sample is a couple of hours. Indirect measurements of T_x can be done by monitoring the resistance of the sample as a function of temperature. Standard

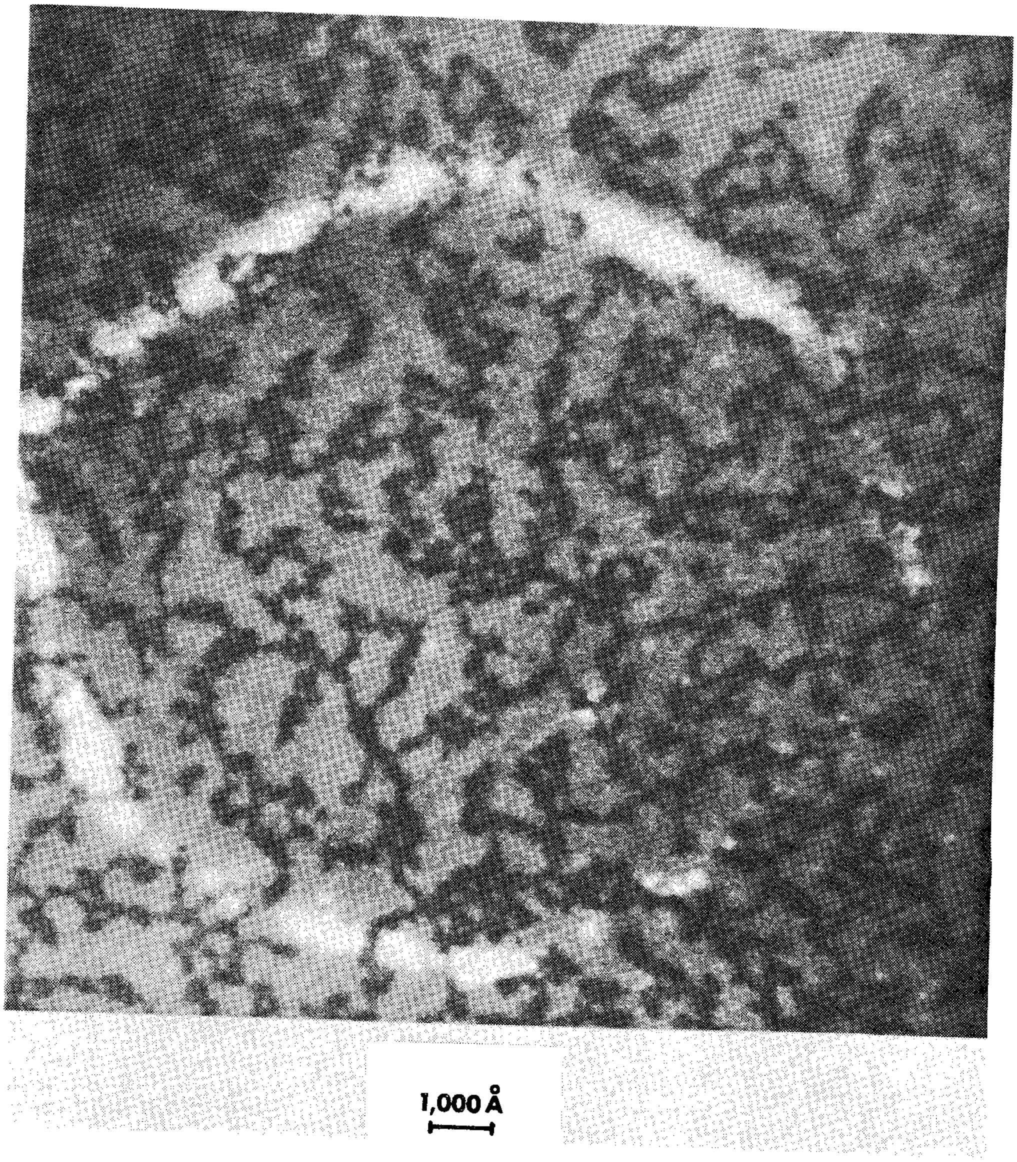

Fig. 22. A TEM micrograph of a characteristic hexagonal crack.

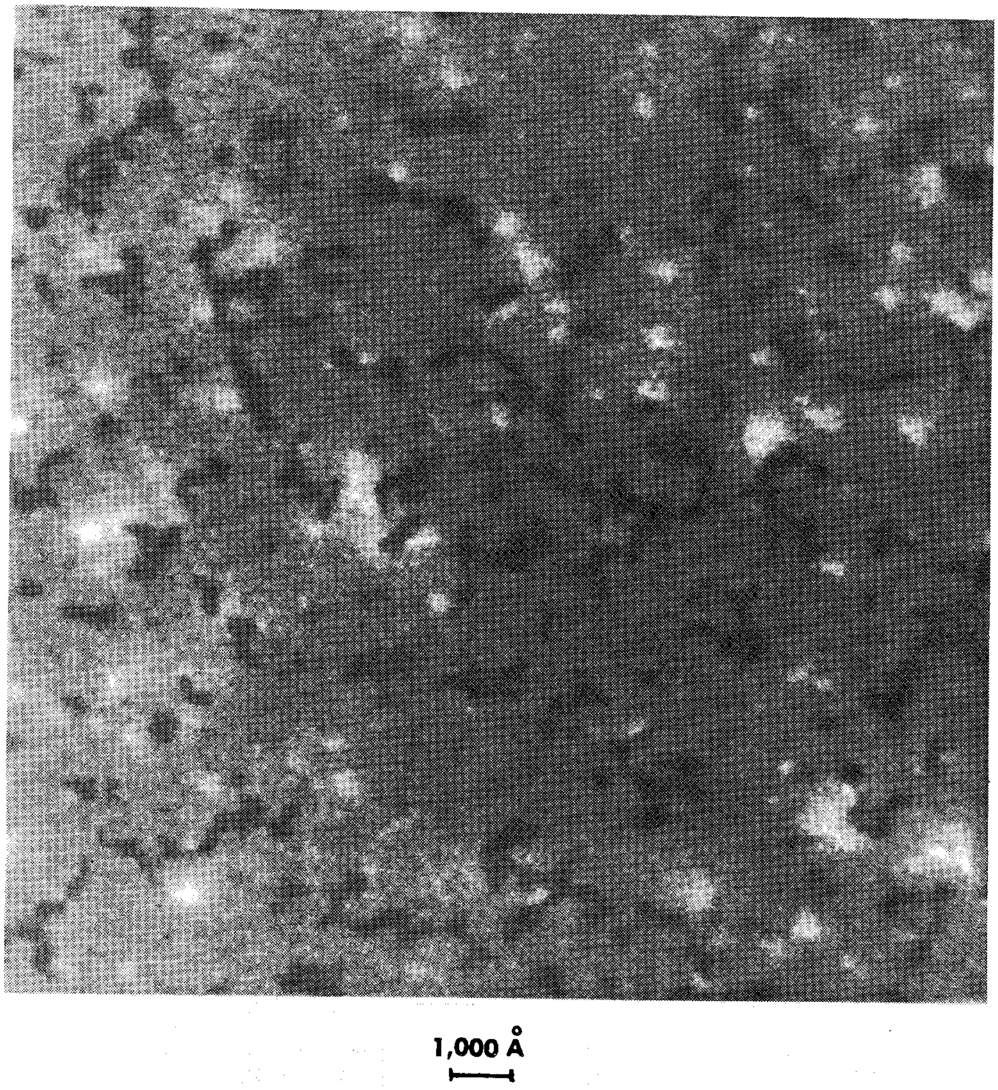

Fig. 23a. TEM micrographs of the samples with 20 minutes air exposure.

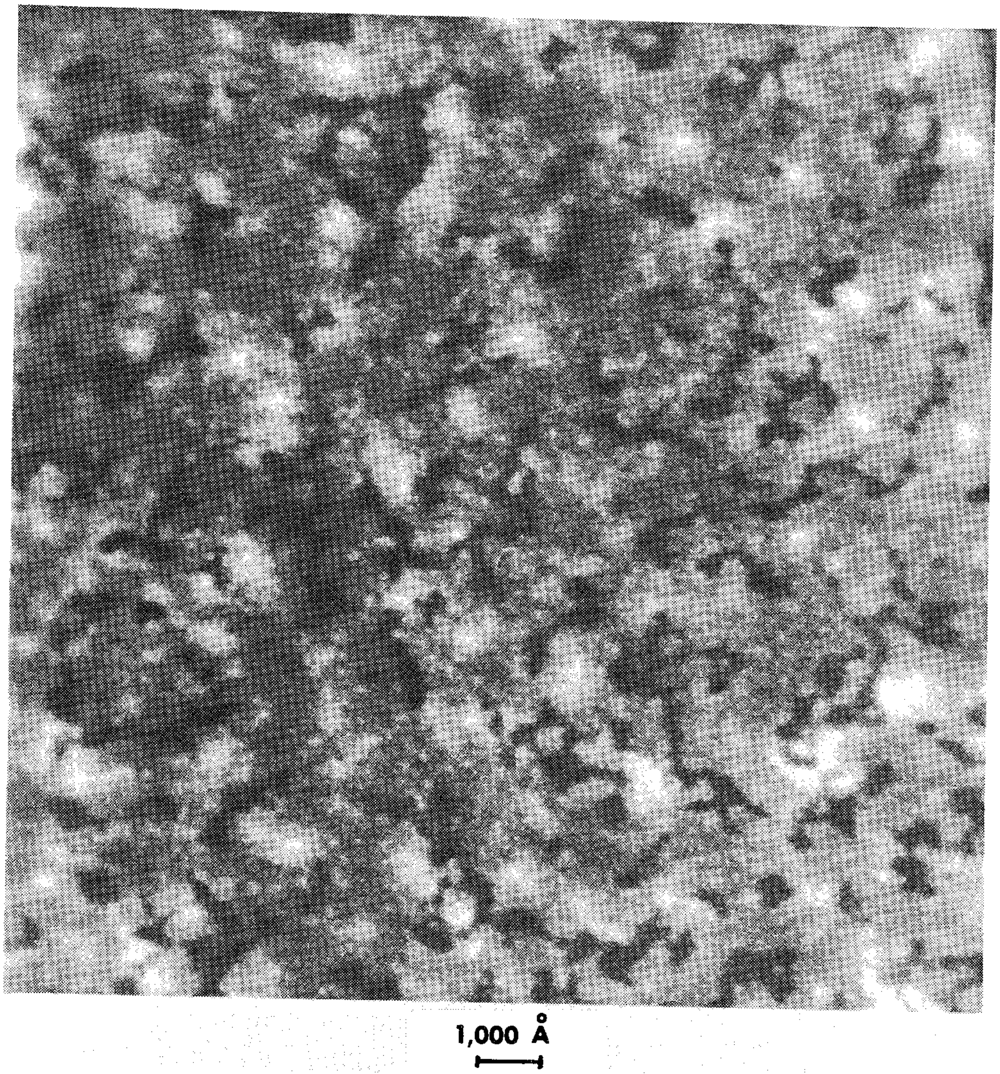

Fig. 23b. TEM micrographs of the samples with 100 minutes air exposure.

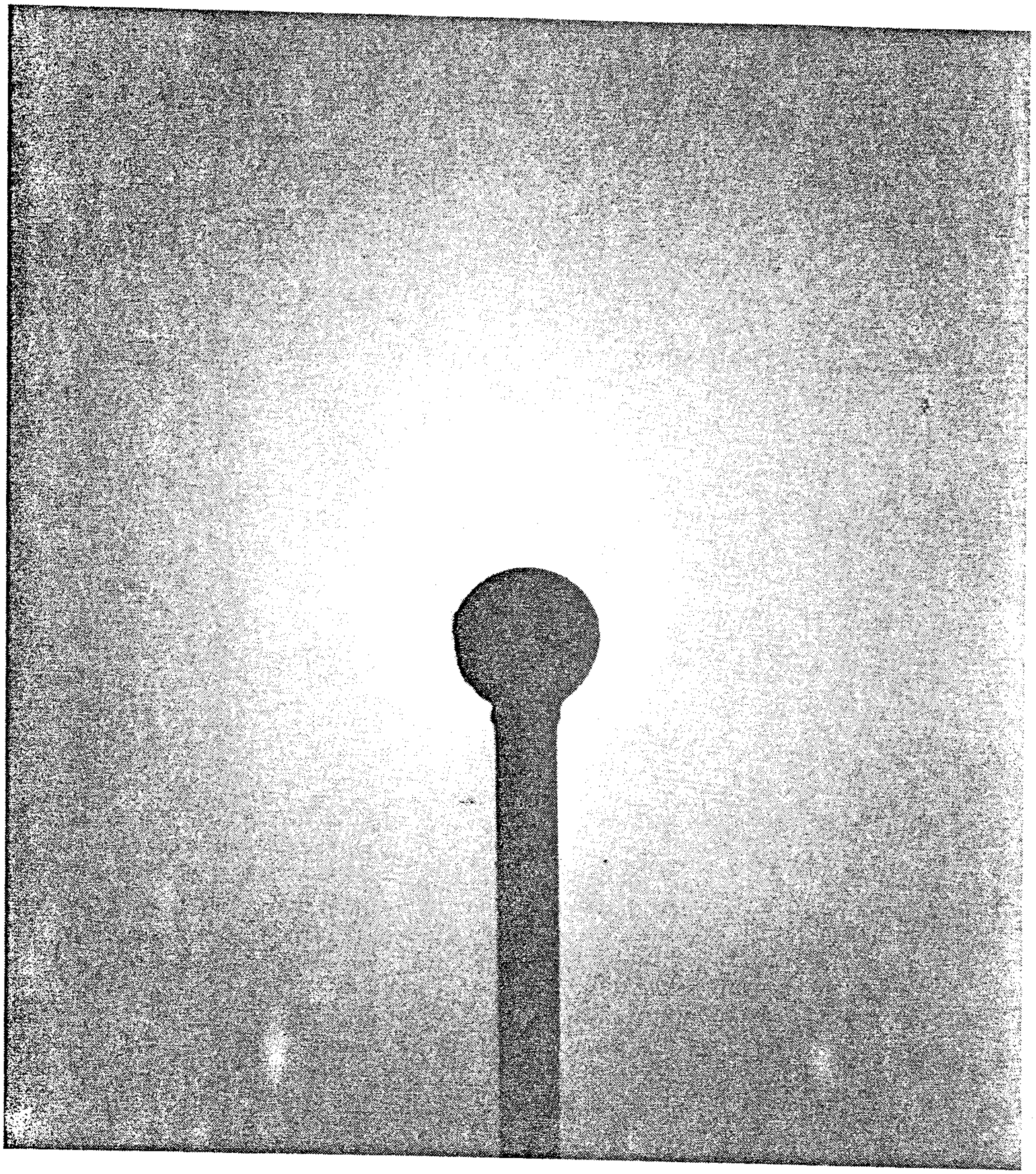

Fig. 24. Diffraction pattern of the reacted sample.

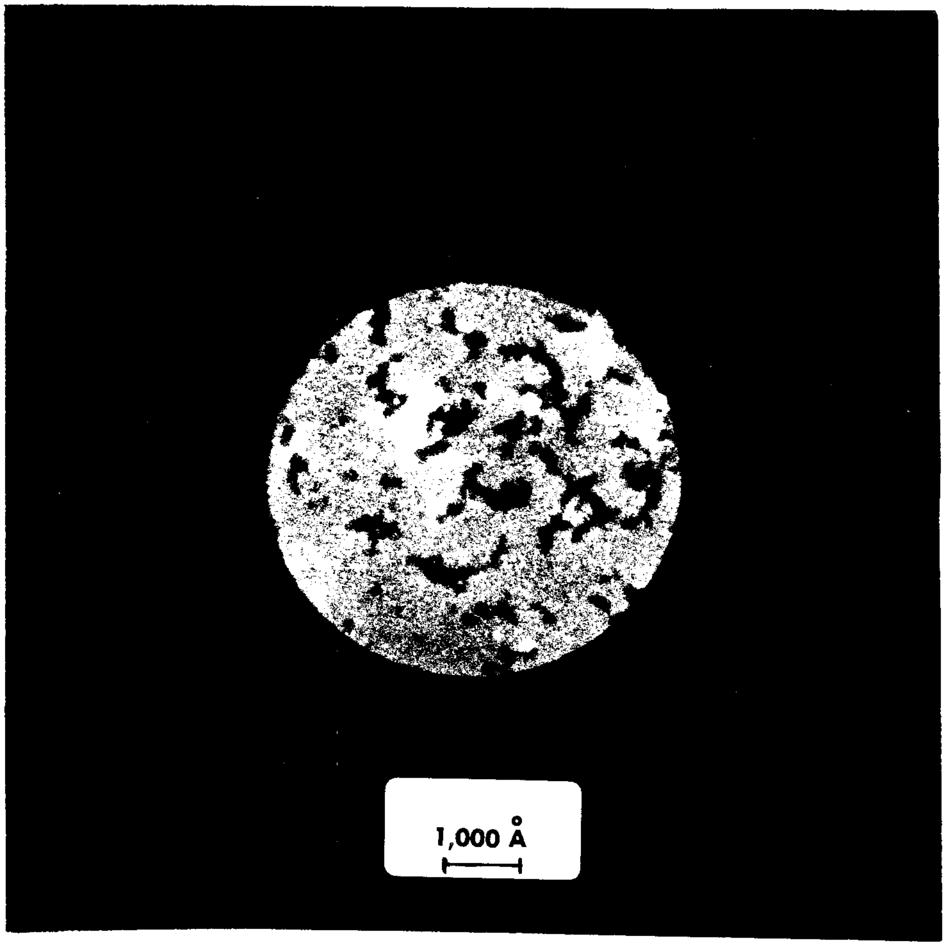

Fig. 25. TEM micrograph of the area of the sample illuminated during the diffraction experiment.

bilayer samples with the ratio Au to La approximately 1:1 and total thickness 2500 Å were prepared for these measurements. The reaction temperature was 105 C. Figure 26 shows the dependence of the resistance of an already reacted sample vs. temperature. The rate of increase of the temperature around the drop in resistance was approximately 1 C per minute. It was checked that up to the temperature 240 C all the changes in the resistance of the sample were reversible. Figure 27 shows the X-ray pattern of the sample after its resistance dropped. A control sample was prepared simultaneously with the sample described in Fig. 26. The control sample reacted at the same conditions but was not heated to 270 C. The X-ray pattern of this sample is shown side by side with the pattern for the crystallized film. The comparison of the X-ray spectra leaves no doubt that a structural transformation takes place at a temperature around 245 C.

IV.4 SIMS MEASUREMENTS.

The samples for the SIMS measurements were standard bilayer samples evaporated on pyrex substrates. They had a 1500 Å La layer at the bottom and a 1000 Å Au layer on top. The vacuum system used permitted the preparation of three samples during the same evaporation. The samples reacted at the temperature 100 C. This thermal treatment was monitored by the value of the resistance following the procedure described in Ch. II.1. The treatment of the first of the three samples was stopped when the resistance of the sample increased 2 times. The second sample increased its resistance

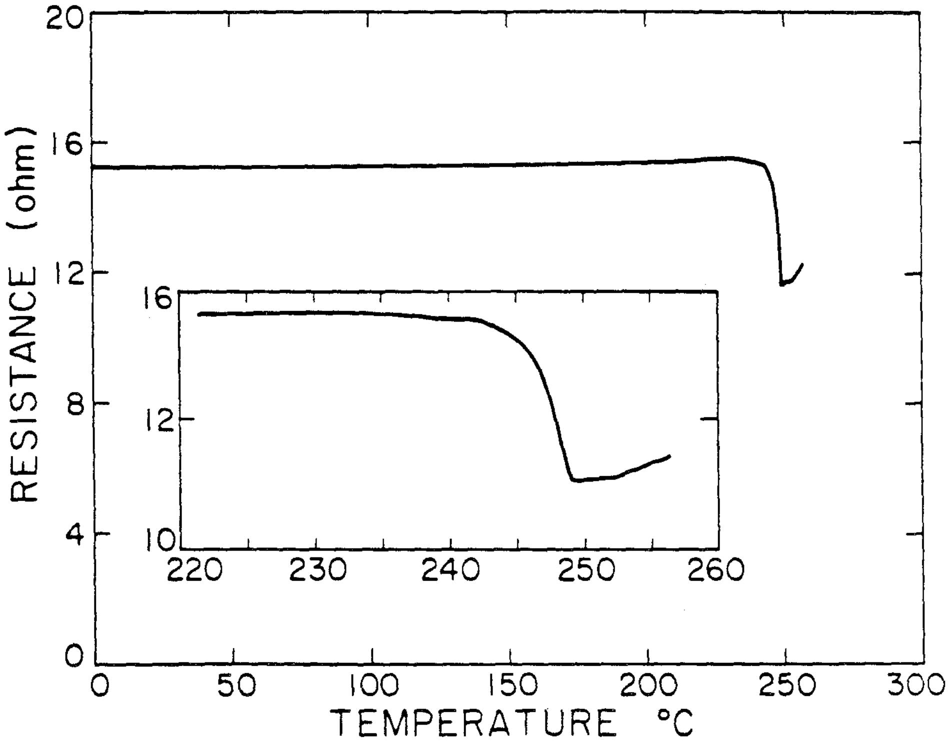

Fig. 26. Resistance vs. temperature dependence for a reacted sample.

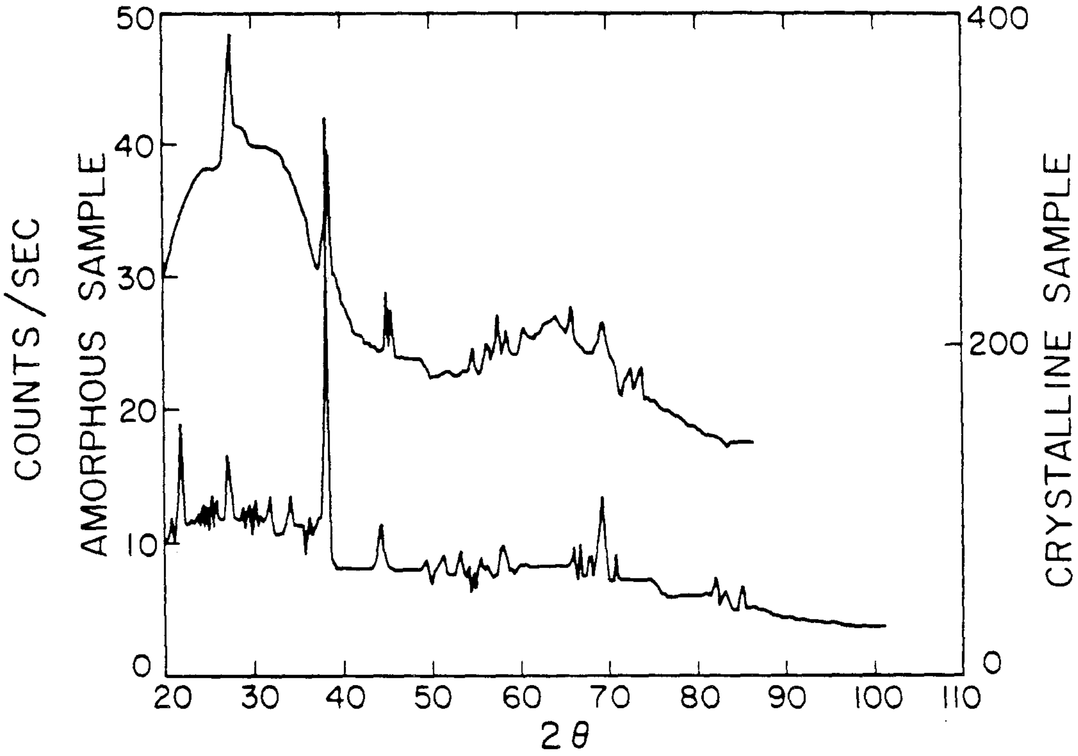

Fig. 27. X-ray diffraction pattern of a reacted sample before and after crystallization.

3 times when its thermal treatment was discontinued. The last sample was reacted until the first signs of the second stage of reaction were detected. This second stage is described previously in this chapter. The resistance of the third sample used in SIMS measurements increased approximately 4 times during the thermal treatment.

The SIMS profiles for the thermally treated samples are reproduced in Fig. 28. In order to interpret the measurements, one should remember that the etching rate of Au is an order of magnitude higher than the one of La. There are 3 points marked on the SIMS profile for the sample #3 in Fig. 28. Several of the SIMS measurements were stopped at the corresponding points so that the depth of etching could be measured directly. The depth at the point "a" was 1000 Å. The depth at the point "c" was 2700 Å. The actual depth measurements show why the thickness of Au in Fig. 28 appears to be several times smaller than the thickness of the La layer. The depth measurements at the point "b" failed because of the fast growth of lanthanum oxide crystals, which could be easily observed in the microscope. The depth of the crater, etched by the primary ion beam, could not be measured on samples #1 and #2. The diamond stylus used to measure the depth of the crater would scratch the top gold layer. In sample #3, the scratching was not observed.

IV.5 INTERPRETATION OF THE EXPERIMENTAL DATA.

The TEM studies show that the final product of the solid state reaction is amorphous at least on the level of sensitivity of an electron microscope. The size of the grains detected in the

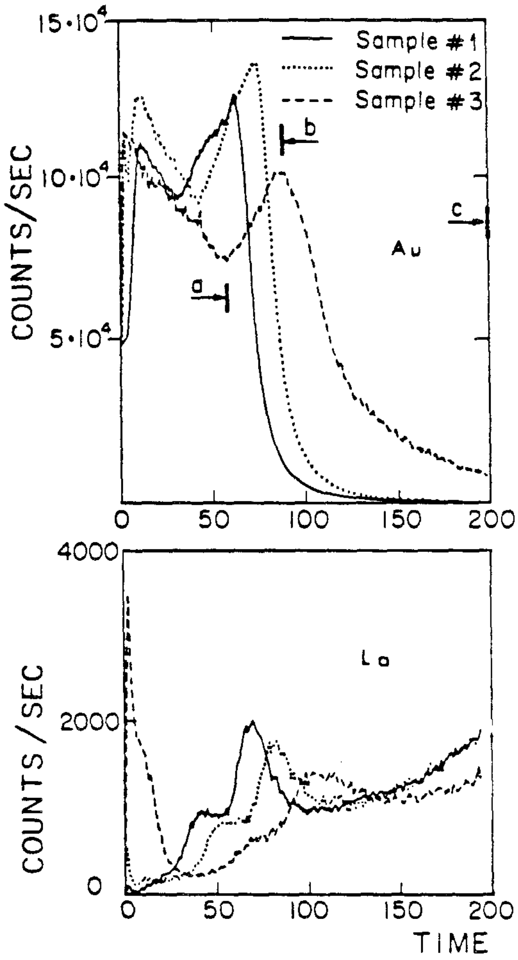

Fig. 28. SIMS profiles for the Au and La signals in the samples 1, 2 and 3. Time is measured in the internal units of the analyzer.

micrograph reproduced in Fig. 23 is more than 50-100 Å. But it takes crystallites smaller than 20-30 Å to widen the diffraction peaks to the extreme when they can possibly be confused with the amorphous band in Fig. 24. The large size of the grains does not permit the interpretation of the diffraction pattern in Fig. 24 as an artifact of the small size crystallites. These arguments make it hard to believe that the final product of the solid state reaction is a microcrystalline compound. The X-ray pattern (Fig. 27) shows a presence of a large diffused band. The size of crystallites in thicker films is usually larger than in thinner ones. This means that small crystallites are not the reason for the diffused band. This is another indirect confirmation that the final product of the Solid State Reaction is amorphous. Figure 27 shows that the films go through a structural transformation at the temperature near 240 C. This observation shows the position of T_x.

There is a significant number of facts which seem to indicate that the growth of the amorphous layer takes place uniformly over the La-Au boundary. The initial rate of change of conductivity is nearly independent of the thickness. An initial growth of the layer in isolated islands would have caused the resistivity to grow initially with a zero slope. This type of growth is not suggested by the data. Grain boundary diffusion effects would have been expected to show some dependence on the thickness of the samples; but none is observed. These are the first indirect confirmations of the planar growth. The final resolution of this problem is brought by the SIMS measurements. A comparison of the SIMS concentration profiles shown in Fig. 28

leads to the conclusion that during the first stages of the solid state reaction there are always well-defined planar interfaces between the growing alloy and the host metals.

At some point in time a supply of one of the materials will come close to being exhausted. The interface between the amorphous layer and that metal will come to the proximity of the terminal surface. This new environment should change the behaviour of one of the interfaces dramatically. In sample #3, the amorphous / gold interface has changed its nature. Sample #3 is the sample which just entered the second stage of the reaction described in Ch. IV.1. The change in the interface behaviour seems to be the reason for the existence of the second stage of reaction. The other interface becomes less well defined during this second stage of the reaction as well. The fact that the top layer of samples #1 and #2 is much softer than the one of sample #3 also agrees with these explanations. The reason for the lack of scratching is that the firmness of La-Au is much higher than the one of Au. In the sample #3, the interface between gold and amorphous material reached the surface of Au and the concentration of La on the surface increased dramatically. This lack of scratching is an indirect confirmation of the the fact that the second stage of the solid state reaction takes place when at least one of the interfaces is close to the surfaces of the film.

The ratio of Au and La in between the interfaces is not constant. The amount of the reacted material grows in time. The second stage of the reaction shows some signs of smearing out of the sharp features of the concentration profiles inside the amorphous layer. These changes in distributions can be interpreted as the equilibration of the distributions inside the newly created alloy. This observation implies that the redistribution inside the growing layer is governed by some kind of diffusion. All these facts are in full agreement with the measurements performed on Ni-Hf in Ref. 30, and in a more detailed study of this system which is described in Ch. VI.

The resistivity measurements were able to show that there is no nucleation delay in the solid state reaction. They excluded island-like growth of the reaction product at least at the beginning of the reaction. Changes of the ratio of Au and La inside the reacted layer show that diffusion should play an important role in the reaction. Simple diffusion models which do not take interfaces into consideration predict $t^{1/2}$ law for the decrease in conductance. This dependence was not observed in the resistance measurements. This inability was the first strong indicator of the importance of the interfaces in the diffusion process.

An exponential type of behaviour of the conductance is determined by the influence of the interfaces. In the next chapter, this type of behaviour will be used to choose the boundary conditions for the mathematical model of the solid state reaction. These boundary conditions are a phenomenological description of the interfaces. Historically, resistance measurements alone provided enough basis for putting forth the model for the reaction (see Ref. 22). Later, this model received some confirmation from the direct measurements of the concentration depth profiles in Ni-Hf system (see Ch. VI).

The "bubbling" of the film seen in Fig. 21 is the first nonplanar effect observed in reacted La-Au samples. This effect can be explained by a simple stress argument. Figure 29 schematically shows the atomic arrangement of Au and La atoms before the reaction (a), after the reaction started (b), and after the bubbling occurred (c). Lanthanum atoms constitute a firm inflexible matrix through which the diffusion of Au occurs. Since the La self-diffusion coefficient is extremely small, the initial distribution of Au and La will probably look like the drawing in Fig. 29b. The film thus created has extreme anisotropy in X and Y directions. To decrease the interaction between the atoms, the difference in the distances between La atoms in direction X and Y should become smaller. This equalization causes the thickness of the film to decrease and the total area of the film to increase. This redistribution introduces stress in the reacting film. This stress is strong enough to peel the reacted film of the pyrex substrate and "bubble" it up. This peeling must also produce some thickness variations in the reacted film. The film with La at the bottom does not peel off. It means that the stresses could not relax. This build-up of stress near the top and the bottom of the film can prevent the reaction from going through those regions. The remaining thin unreacted layers could be the reason why the change of resistivity of the thin samples was higher than that for the thick one. They can also explain the peeling off of the reacted films in the air. A more detailed discussion of this subject is presented in Chapter VI.

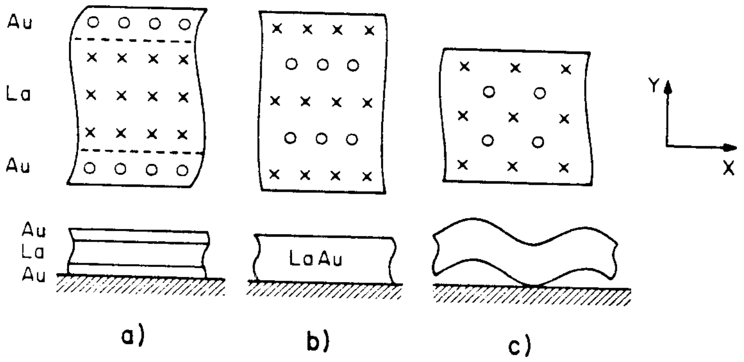

Fig. 29. The atomic arrangements of the layers a) before, b) during, and c) after the reaction. See the explanations in the text.

V. MODEL FOR THE SOLID STATE REACTION.

V.1 FIRST TIME CONSTANT.

Diffusion is likely to play an important role in the Solid State Reaction. The diffusion coefficient of Au in crystalline La is unusually large at low temperatures (see Fig. 5). Au is also a fast diffuser in Y. The same is true for Ni in Hf and Zr[47]. Thus all the couples which demonstrated the possibility of the solid state reaction[11,12,28-30] are characterized by the presence of a fast diffuser.

In the previous chapter, it is shown that a significant number of facts seems to indicate that the growth of the amorphous layer takes place uniformly over the La-Au boundary. The initial rate of change of conductivity during the reaction in La-Au is nearly independent of the original layers′ thickness; and there is no delay of the onset of resistance growth. These observation exclude nucleation and island-like growth at the onset of the reaction. The direct SIMS measurements of the distribution of Au in La during the reaction described in the previous chapter and the measurements performed on other bilayer systems (Ni-Zr[29] and Ni-Hf[30]) yield similar results: 1. The growing amorphous layer has a rather uniform and well-defined thickness at a given time during reaction. 2. The interfaces with the parent crystalline metals are rather sharp. There is no significant amount of fast diffuser outside the growing amorphous layer. 3. The influence of the grain boundary diffusion effects is insignificant. Together, all the above facts suggest that the reaction could be described in terms of a one-dimensional uniform layer growth with possible interface limiting. The proposed description is a development of the model introduced by Deal and Grove[31] to explain the thermal oxidation of silicon and adopted by Geguzin et al.[32] for growth of crystalline layers.

In the general case of the interdiffusion of two layers, the distribution of the concentration of components at times t=0 and t=tl looks like the one in Fig. 30. This diffusion can be described using a common approach originated by Darken[33] in order to explain the Kirkendall effect[34]. This aproach was outlined in chapter II.2. There is a significant difference between the treatment of the situation in question and the way it is usually done in the case of crystalline layer growth. For crystals, the ratio of the homogeneity range to the concentration of the alloy layer is negligibly small. In the case of an amorphous material, the ratio of the homogeneity range in which an amorphous alloy can be formed to the alloy concentration is large. This situation requires more careful treatment of the diffusion equations. When the amorphous interlayer grows, the diffusion must not only supply the amount of the fast diffuser required to increase the amount of the amorphous material, but also an additional amount to allow the concentration profile within the existing amorphous layer to evolve in time. In the case of a growing intermetallic crystalline compound, the latter is negligibly small and the concentration profile inside the interlayer can be assumed to be linear. This conclusion

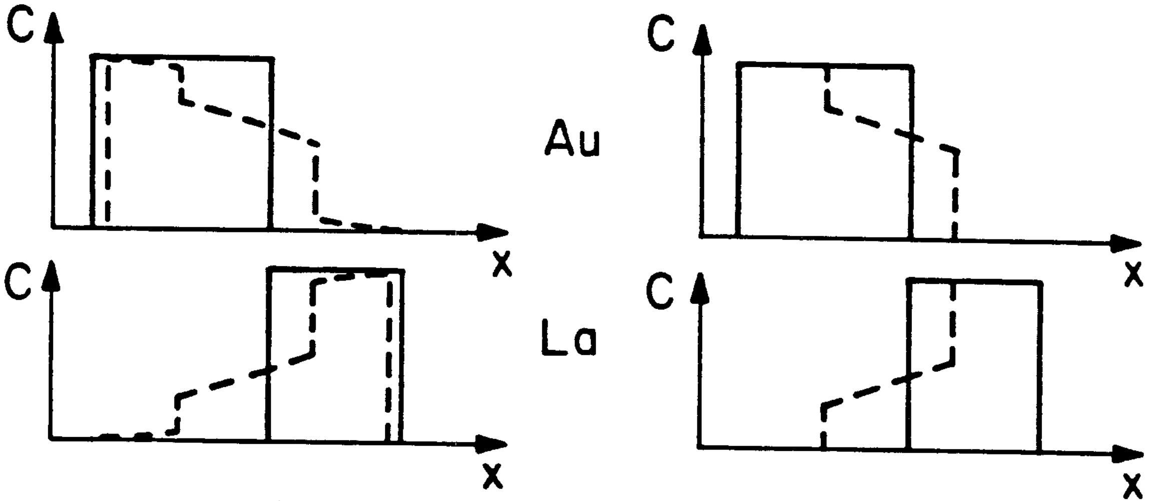

a)

b)

Fig. 30. Distributions of the concentration of the inter-diffusing couple at two different moments in time: a) in a general case; and (b), in a case when there is no solubility of the elements in each other and no change of volume during formation of the new phase.

follows from the fact that the total variation in concentration is necessarily quite small. For the case of an amorphous material, the concentration of the growing layer can vary over a broad range. The solute redistribution will lead to changes in the concentration profile. This profile can no longer be assumed to be linear.

It is also known in the present case that the mutual terminal solubility of parent metals, which comprise the diffusion couple, is negligibly small (much less than 0.2% for Au in La[27]). Also, it is known from the density data on La, Au and amorphous La Au[35] that the relative excess molar volume of formation for the amorphous phase is small (of order of 2-3%). This excess volume can be neglected as a first approximation. Mathematical difficultes force us to neglect as a first approximation the nonplanar phenomena which lead to the "bubbling" described in the previous chapter. All these simplifications will lead to a concentration distribution which look like the one in Fig. 30b.

The "flux equations" for a general case were introduced in the chapter II.2. The "flux equation" for the situation described above is a diffusion equation with the diffusion coefficient

$$D \approx (C_{au} * D_{la} + C_{la} * D_{au})(1 + H_{mix}/kT),$$

where D and C are diffusion coefficients and concentrations of the corresponding phases; and H_{mix} is the energy of mixing of elements in the amorphous alloy. In the case of La-Au alloy one writes $D_{la}=0$ (La is not a fast diffuser) and since $H_{mix} >> kT$

$$D \approx (1-C) D_{au} (1 + H_{mix}/kT) \approx D_{au} H_{mix} C (1-C)^2 / kT$$

Due to calculation difficulties, D is assumed to be constant in the discussion below.

The influence of the interface limiting can be mathematically described as boundary conditions for the diffusion fluxes in between the interfaces. The physical description of the interfaces from the first principles has not been developed yet. So far, the indirect measurements similar to the experiments described in chapters IV and VI are the only source of the experimental information about the interfaces. The boundary conditions proposed below are able to explain the interlayer growth in La-Au and Ni-Hf systems. These boundary conditions do not contradict any known data for the crystalline materials. Until the physical theory of the interfaces is developed the proposed set of the boundary conditions is no more or less appropriate than any other set which is able to explain the same experimental data.

Given the above approximations, the process of diffusion can be described by the following set of equations:

$$\begin{cases} \dfrac{\partial C}{\partial t} = D \dfrac{\partial^2 C}{\partial X^2} \\[2ex] D \left.\dfrac{\partial C}{\partial X}\right|_{X_{fa}} = (1-C_{fa}) \dfrac{dX_{fa}}{dt} \\[2ex] -D \left.\dfrac{\partial C}{\partial X}\right|_{X_{am}} = C_{am} \dfrac{dx_{am}}{dt} \\[2ex] \dfrac{dX_{am}}{dt} = \text{Function } (C_{am}-C_2) = \kappa_2(C_{am}-C_2) \\[2ex] \dfrac{dX_{fa}}{dt} = \text{Function } (C_{fa}-C_1) = \kappa_1(C_{fa}-C_1) \end{cases}$$

where - D is a diffusion coefficient assumed to be independent of the concentration.

- C - concentration of the fast diffuser
- C_1 - the concentration of Au in amorphous alloy which would allow thermodynamic equilibrium with pure Au (see ref. 11) at the fast diffuser - amorphous boundary (FA boundary).
- X_{fa} and C_{fa} - position of and the concentration at the FA boundary
- C_2 - the concentration of Au in amorphous alloy which would allow thermodynamic equilibrium with pure La (see ref. 11) at the amorphous-matrix boudary (AM boundary). La is referred to as a matrix.
- X_{am} and C_{am} - position of and the concentration at the AM boundary
- κ_1 and κ_2 - interface parameters for AM and FA boundaries.

It is assumed that $dX_{am}/dt=\kappa(C_{am}-C_2)$. This assumption differs from the assumption of the previous papers[31,32]: $dX_{am}/dt=\alpha(C_{am}-C_2)/C_{am}$. These two assumptions are virtually the same in a case where $(C_1-C_2/C_2<1$. Such a case is typical for crystalline solids. This condition is not true for a case of an amorphous material where C_2 can be much smaller than C_1. The reason for introducing a different assumption is to obtain a solution for the growth of the interlayer which, at small times, is in better agreement with what is observed in the resistance measurements. The assumption used in Ref. 31 and 32 does not produce an exponential behavior of the depth of penetration of the amorphous layer which can result in the exponential type of decrease of conductivity present in the measurements (see Fig. 19). The assumption used in the thesis gives the observed dependence.

If one uses normalized units

$$X \rightarrow X \cdot D/(\kappa_1+\kappa_2)$$

$$t \rightarrow t \cdot D/(\kappa_1+\kappa_2)^2$$

$$\alpha = \kappa_1/(\kappa_1+\kappa_2)$$

then the system of equations will look as follows:

$$\begin{cases} [\alpha(C_1-C_{fa}) + (1-\alpha)(C_{am}-C_2)] \dfrac{\partial C}{\partial X_a} = \dfrac{\partial^2 C}{\partial X^2} \\ \left.\dfrac{\partial C}{\partial X}\right|_{X_{fa}} = -\alpha(1-C_{fa})(C_1-C_{fa}) \\ \left.\dfrac{\partial C}{\partial X}\right|_{X_{am}} = -(1-\alpha)C_{am}(C_{am}-C_2) \end{cases} \qquad (8)$$

and

$$\frac{dt}{dX_a} = \frac{1}{\alpha(C_1-C_{fa}) + (1-\alpha)(C_{am}-C_2)}$$

where X_a is the width of the amorphous layer. This three parameter system of equations was solved numerically (See Appendix 1).

Figure 31 shows the positions of the interface and the distribution of the fast diffuser (Au) at different times for given C_1, C_2 and α .

The solutions of the system of equation show existence of a locus point. The point position and the value of the concentration at this point hardly change. In cases when κ's and and C's scale with each other, the locus point does not move at all. So, in many of cases, the solution of the equations can be constructed of or approximated by the solutions of the following simplified system of equations. The diffusion process in the region of interest is now controlled by the fixed point and only one moving interface. The penetration of the amorphous layer into one of the host metals can be described by a one-parameter system of equations:

$$\begin{cases} \dfrac{\partial C}{\partial t} = D\dfrac{\partial^2 C}{\partial X^2} \\ C(X = 0) = C_{in} \\ -D\dfrac{\partial C}{\partial X}\Big|_{X_{am}} = C_{am}\dfrac{dX_{am}}{dt} \\ \dfrac{dX_{am}}{dt} = \kappa(C_{am} - C_2) \end{cases}$$

or in new normalized units:

$$\begin{cases} C_{am}\dfrac{\partial C}{\partial X_{am}} = \dfrac{\partial^2 C}{\partial X^2} \\ C(X=0) = 1 \\ \dfrac{\partial C}{\partial X}\Big|_{X_{am}} = C_{am}(C_{am}+A-1) \end{cases} \qquad (9)$$

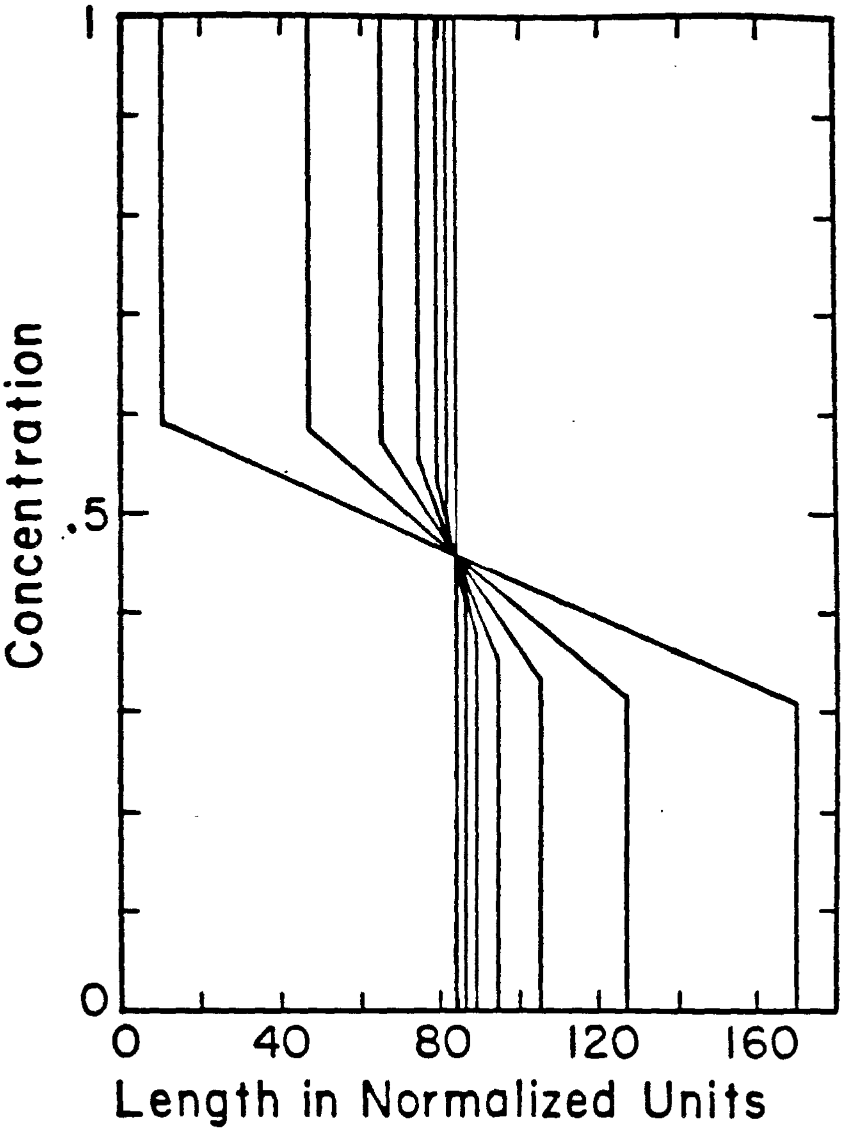

Fig. 31a. Positions of the interfaces and the distribution of the fast diffuser at different moments in time. Amorphous layer thicknesses are 5,10, 20, 40, 80 and 160 normalized units. Speeds of penetration of the amorphous layer into the host metals are different. The ratio of the speeds is approximately constant. The locus point actually moves; but its movements are too small to be detected on the given scale of X. $C_1=0.6$, $C_2=0.3$, $\alpha=0.25$.

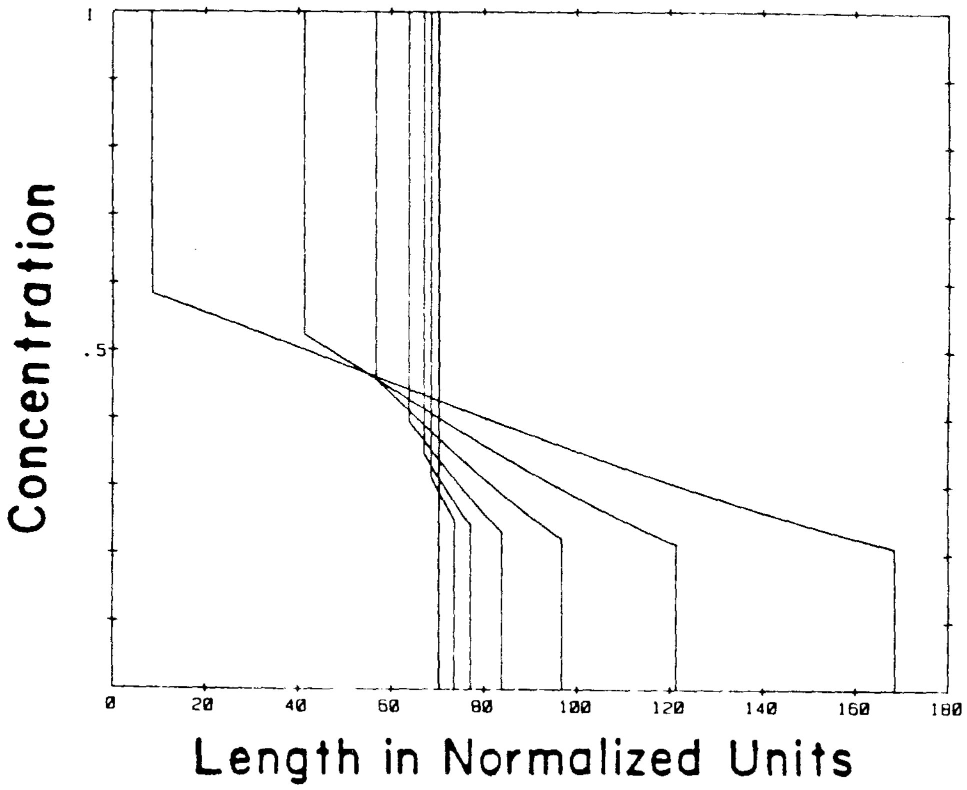

Fig. 31b. Positions of the interfaces and the distribution of the fast diffuser at different moments in time. Amorphous layer thicknesses are 5,10, 20, 40, 80 and 160 normalized units. Speeds of penetration of the amorphous layer into the host metals are different. The ratio of the speeds is approximately constant. The locus point actually moves; but its movements are too small to be detected on the given scale of X. C_1=0.6, C_2=0.3, α=0.05.

where $A = C_{in}/(C_{in}-C_2)$

C_{in} is close or equal to the initial concentration at which the amorphous layer starts to grow (Fig. 31).

$$X \rightarrow X \frac{D}{(C_{in}-C_2)\kappa}$$

$$t \rightarrow t \frac{D}{(C_{in}-C_2)^2\kappa^2}$$

$$C \rightarrow (C+A-1)(C_{in}-C_2)$$

and

$$\frac{dt}{dX_{am}} = \frac{1}{C_{am}}$$

The typical solution of the system of equations (9) is in Fig. 32. The asymptotic expansion of the solution of this system can be obtained form the following Taylor expansion:

$$C\,(X_{am},X) = \sum_{n=0}^{\infty} C_n(X_{am})\,\frac{(X_{am}-X)^n}{n!} \qquad (10)$$

where factors C_n are the solutions of:

$$\begin{cases} C_0 = C_{am} \\ C_1 = C_0\,(C_0+A-1) \\ C_n = C_0\,\left(C_{n-1}+\dfrac{dC_{n-2}}{dX_{am}}\right) \\ \displaystyle\sum_{n=0}^{\infty} C_n(X_{am})\frac{X_{am}^n}{n!} = 1 \end{cases} \qquad (11)$$

From these equations the dependence of C_{am} for small X_{am} is:

$$C_{am} = 1 - AX_{am} + A(A+1)X_{am}^2 - \left(A^3 + \frac{4}{3}A^2 + \frac{10}{3}A\right)X_{am}^3 + \ldots$$

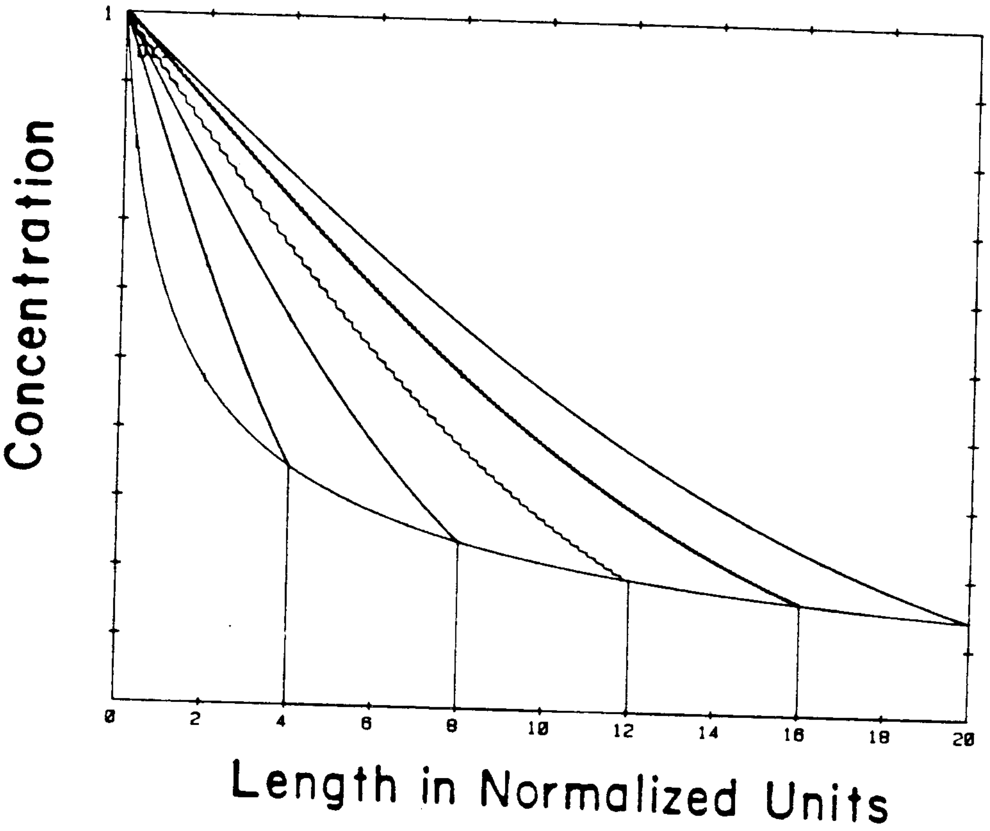

Fig. 32. Time dependence of the concentration profiles. Typical solution of the simplified model discussed in the text.

which can be checked by the direct substitution.

The asymptotic time-dependence of the position of the interface for small X_{am} can be obtained if one neglects all terms but the first one in the penetration depth dependence of C_{am}:

$$\frac{dX_{am}}{dt} = C_{am} = 1 - A\, X_{am}$$

and

$$X_{am} = \frac{1-\exp(-At)}{A} \qquad (12)$$

which is exactly the exponential behavior suggested by the resistivitv measurements (Fig. 19).

For large X_{am}, the first term in the asymptotic expansion of the solution for the concentration at the boundary is:

$$C_{am} \approx \frac{a}{X_{am}}$$

where "a" is the solution of

$$\frac{1}{A-1} = \frac{a}{1} + \frac{a^2}{1\cdot 3} + \frac{a^3}{1\cdot 3\cdot 5} + \frac{a^4}{1\cdot 3\cdot 5\cdot 7} + \cdots \qquad (13)$$

This equation leads to the usual $t^{1/2}$ dependence, though, with a different factor in front of D. It can be shown (see Appendix 2) that the actual form of the asymptote is:

$$C_{am} = \frac{a}{X_{am} + \frac{1}{A-1}} + \frac{ab}{3X_{am}^4 (A-1)^4} + \cdots \qquad (14)$$

where $b \approx 1$. The value of b is a function of A. From this asymptote, one gets the following dependence of the penetration depth of the amorphous layer vs. time:

$$X_{am} = -\frac{1}{A-1} + \sqrt{2at} + \ldots \qquad (15)$$

This form of a shifted $t^{1/2}$ dependence described by equation (15) has in fact been observed in Ni-Hf[23]. From this data, an estimate of the values of κ and D were obtained. These results are described in the next chapter.

It is worth mentioning that the standard linear approximation for the distribution of the concentration between the interfaces (an assumption typical for the treatment of crystals) gives $a=1/(A-1)$, which is rather far from the actual solution to the problem obtained here. The existence of the shifted $t^{1/2}$ time dependence similar to the one described by equation (15) was discovered by Deal and Grove[31] for the thermal oxidation of silicon but an assumption of a "steady-state solution" prevented the authors from getting the proper factor in front of D and the time dependence of growth at the beginning of the process. The assumption of a "steady-state solution" neglects all the terms but the first two in the Taylor expansion (10) for the solution of the flux equations.

If one converts from the normalized units to the usual ones, then equation (15) will have a following form:

$$X_{am} = - \frac{D}{\kappa_2 C_2} + (2aDt)^{1/2} + \ldots \qquad (16)$$

If $\kappa \to \infty$ the influence of the interfaces will become negligible and there will be no interface limiting. Since the term with the $t^{1/2}$ does not contain κ, the factor in front of the diffusion coefficient will still be "a" but not $(C_{in}-C_2)/C_2=1/(A-1)$. The latter means that a widely used "steady-state" linear approximation for the distribution of the diffuser in the limit of long times is incorrect even in the case when there is no interface limiting.

The time dependence of the concentration gradient should allow one to distinguish between the "steady-state" approximation and the exact solution described earlier. The average concentration gradient in the growing layer can be approximated by $(1-C_{am})/X_{am}$. The asymptotic dependence for the inverse gradient can be obtained from equations (13) and (15) in a form:

$$(\text{Gradient})^{-1} = -(\,a - 1/(A-1)) + \sqrt{2aDt} \quad + \ldots$$

or in conventional units for the case of large A

$$(\text{Gradient})^{-1} = -\frac{D}{3\kappa C_2{}^2} \quad + \quad (C_{in}-C_2)^{-1}\sqrt{\frac{2Dt(C_{in}-C_2)}{C_2}} \quad + \ldots \qquad (17)$$

In the usual "steady-state" approximation a=1/(A-1) and therefore there is no shift in the $t^{1/2}$ dependence of the gradient.

V.2 SECOND TIME CONSTANT.

In the limit of long times, the interlayer will consume most of the material of the diffusion couple; and at least one of the interfaces will come close to the surface of the film. The movement of this interface will slow down drastically. At this point, the mechanism of growth described above will cease to be valid. Instead, one will ultimately observe a diffusional redistribution of the fast diffuser inside the amorphous layer and relaxation of remaining stresses. The time dependence of this final redistribution is determined by the decay of the first harmonic in the distribution of the fast diffuser and the stresses in the amorphous layer. Obviously this mechanism has an exponential nature. It is believed that this redistribution process is the mechanism responsible for the second time constant found in our conductivity plots (see Fig. 20). This process will be greatly influenced by the remaining amount of the fast diffuser (or the matrix if there is not enough fast diffuser). This influence is probably responsible for the larger scatter of the points corresponding to the second time constants. The slope of the Arrhenius plot for the second time constants (Fig. 20) gives an activation energy which is also close to that for diffusion of Au in crystalline La[36]. It especially obvious in the case of the two-layer samples. Although the diffusion constant referred to in our equations is that for Au diffusion in amorphous Au-La while we are comparing this with the diffusion in crystalline La, it is not unreasonable to find that these two processes have activation energies which are not very different. This issue was discussed in Chapter II.1.

If at any time the concentration at one of the interfaces reaches a value for which a single amorphous phase becomes unstable, a new interface should be introduced. It will lead to the situation discussed by U. Gosele and K. N. Tu[37] and will explain the results obtained in Ref. 28 and 12 where an additional compound was sometimes observed as a result of the Solid State Reaction. The nucleation of additional compounds can determine the maximum thickness of the amorphous layer which can be produced by a solid state reaction at a given temperature. A simple comparison between parameters κ in a way similar to the calculations in Ref. 37 should give this maximum thickness. But the measurements of these parameters is a complicated problem. The creation of this additional interface can also change the behaviour of the previously existing interfaces and can be an alternative mechanism for the second time constant.

V.3 EXPERIMENTAL VALUES OF PHENOMENOLOGICAL PARAMETERS.

The value for the first time constant from equation (12) is $D/A\kappa^2(C_{in}-C_2)^2$. This factor must be the reason why the Arrhenius plot (Fig. 20) gave an activation energy close to that for Au diffusion in crystalline La. Comparison between the values of the first and the second time constants should give the value of D and κ. The value of the second time constant, if the mechanism described in the previous paragraph is correct, should be $d^2/D\pi^2$, where d is the total layer thickness (d=2500 Å for the samples in Fig. 20). From Ref. 11 one gets values of $C_1=0.6$ and $C_2=0.3$. Assumption of $\kappa_1=\kappa_2$ will lead to $A\approx 4$ and $C_{in}\approx 0.43$. Using these values, equation (12) and the data for bilayers from Fig. 20, one can obtain the following estimates of the parameters used in the model $D\approx 10^{-13}cm^2/sec$ and $\kappa\approx 45$ A/sec at 120 C. Activation energy for both is assumed to be the same as that for the diffusion coefficient of Au in crystalline La. Figure 33 shows the values of the diffusion coefficient plotted vs. temperature for a number of glasses. The value of the diffusion coefficient obtained from the estimate presented in this chapter fits well into the pattern.

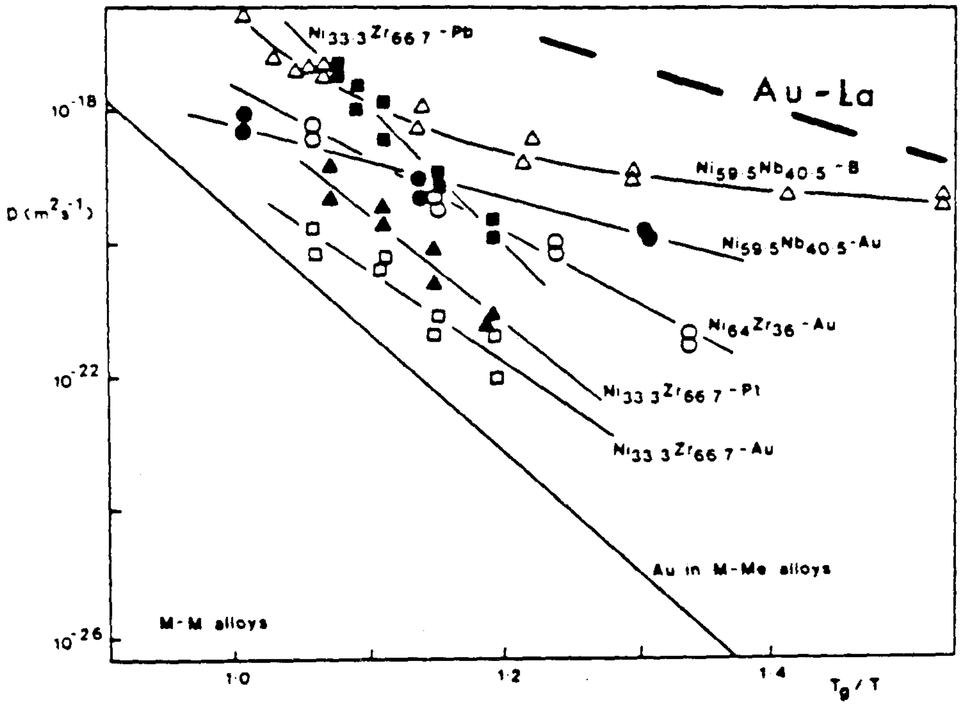

Fig. 33. Normalized Arrhenius plot of directly measured diffusion coefficients (after Ref. 44). Calculated values of parameter D for Au-La couple are shown also.

VI. COMPARISON OF THE MODEL FOR THE SOLID STATE REACTION WITH THE MEASUREMENTS ON REACTING NI-HF LAYERS.

VI.1 INTRODUCTION.

The model for the Solid State Reaction proposed in the previous chapter has been used to interpret resistivity measurements on the amorphization of Au-La multilayer films; and an overall consistent picture of the reaction process has emerged. However, several features of the reaction could not be investigated by those experiments, due to the bulk nature of resistivity data. In particular, a detailed study of the evolution of the concentration profiles during the reaction was still lacking. Van Rossum, et al.[30] applied Rutherford backscattering spectrometry to the study of the Solid State Reaction in Ni-Hf thin films. It was shown that this technique possesses the sufficient depth resolution required to control the reaction. This chapter describes a more detailed investigation of the reaction kinetics in Ni-Hf diffusion couples. Rutherford backscattering is the experimental tool for the study. A systematic comparison of backscattering data with the available diffusion model is presented. On the basis of this comparison, the effective diffusion constant, the activation energy, and the phenomenological boundary parameter for the Ni-Hf system are calculated.

VI.2 SAMPLE PREPARATION AND THERMAL TREATMENT.

Ni-Hf bilayers were prepared by electron-gun evaporation on oxydized Si substrates. The ambient pressure was brought below 10^{-7} torr prior to deposition. The bilayers consisted of a 3000 A Ni film and an Hf layer with a thickness varying between 500 and 1500 A. A thin (50 A) Hf layer was intercalated between the substrate and the Ni film to improve adhesion. All samples had Hf as the top layer.

Thermal treatments were carried out in a vacuum furnace at an average pressure of $5 \cdot 10^{-7}$ Torr. The treatment was preformed in isochronal and isothermal steps. The structural characterization of the samples before and after thermal treatment was accomplished by X-ray diffraction at glancing angle. The concentration profiles of Hf and Ni after successive thermal treatment steps were recorded by backscattering spectrometry, using 2 MeV He^+ ions. In some cases, the target was tilted with respect to the incident beam to insure optimal depth resolution.

VI.3 EXPERIMENTAL RESULTS.

Isothermal thermal treatment sequences were performed at 320, 340, 360 and 380 C. In Ref. 30, the onset of the reaction was observed around 300 C. Backscattering spectra for a typical isothermal sequence are shown in Fig. 34. The backscattering signals were normalized so as to make the Ni signal to be constant far away from the reacting layer. This normalization corresponds to the constant density of the bulk Ni

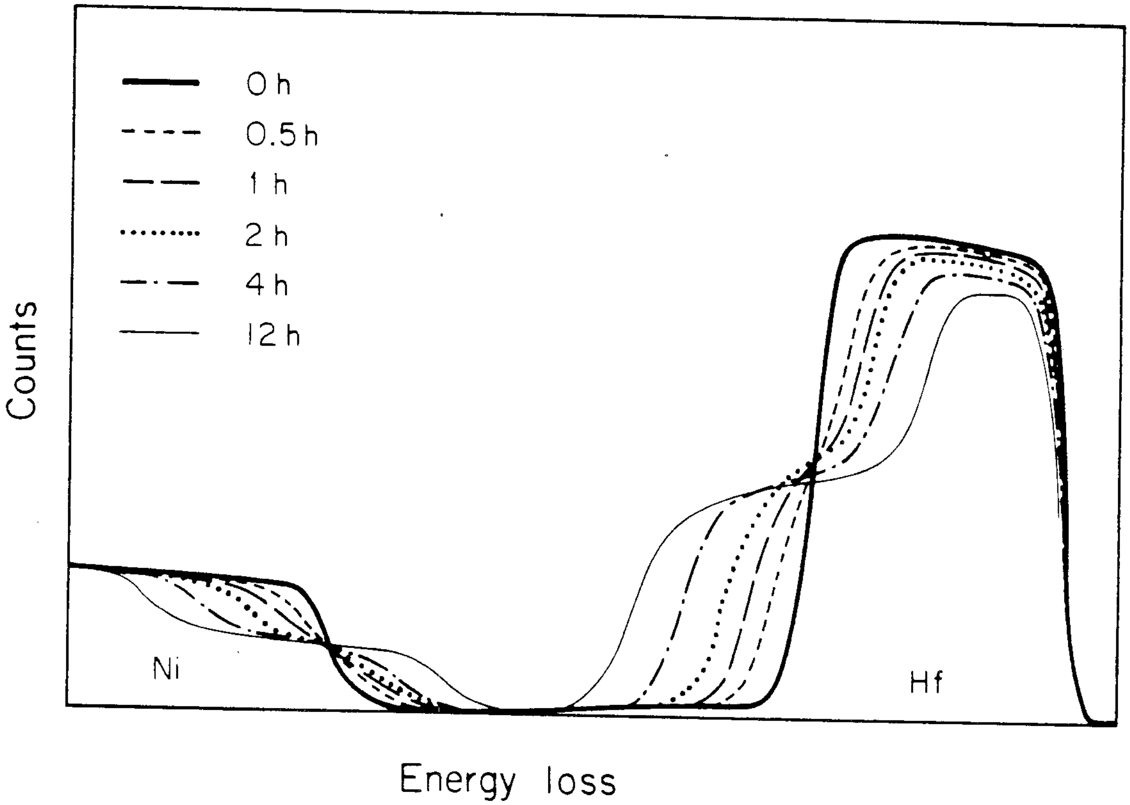

Fig. 34. Backscattering profiles for the sample as deposited and reacted at 340 C for 0.5, 1, 2, 4, and 12 hours.

far away from this layer. This procedure also establishes the proportionality between the Hf signal far from the reacting layer and the Hf concentration in that region. The amplitude of the Hf signal obtained for distances far away from the amorphous layer shows some variation which is illustrated in Fig. 35.

The growth of the amorphous layer has always been followed by measuring the position of the Ni edge with respect to the Hf surface, i.e. , from the amount of unconsumed Hf metal. In this way, no assumption concerning the density of the amorphous layer must be made to establish the depth scale of the reaction. However, this type of analysis assumes that the density of the remaining Hf matrix is constant as the reaction evolves. The latter assumption can be questionable (see Fig. 35). The other assumption made is the uniformness of the growing layer. The degree of uniformity has not been directly established either. Fig. 36 shows a set of experimental points taken at 340 C. The spacing between the points roughly corresponds to the depth resolution of the backscattering measurements (which is about 150 Å for the perpendicular beam incidence). The solid line represents the time shifted $t^{1/2}$ dependence which is predicted for the penetration depth in the previous chapter. The method for obtaining parameters for this prediction is described later. It is generally observed that the experimental points first converge toward a time shifted $t^{1/2}$ behaviour; but usually the reaction slows down prior to completion. The time or the width of the amorphous layer at which this deviation occurs depended on the thicknesses of the reacting layers (see Fig. 36).

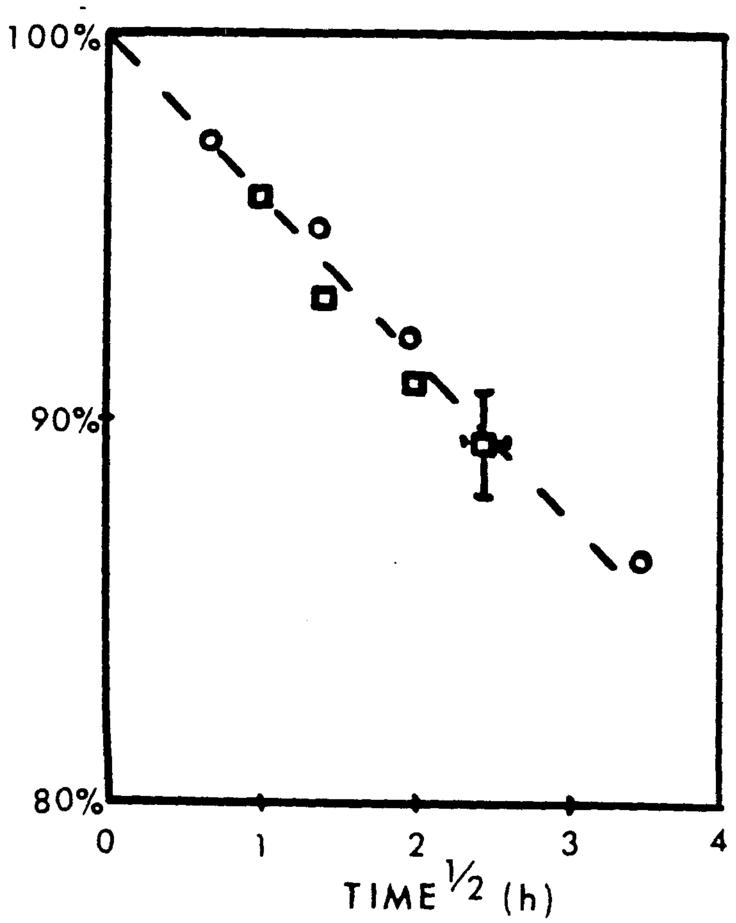

Fig. 35. The time dependence of the ratio between the current amplitude of the Hf signal and its value at the beginning of the reaction for the samples with the constant (1500 Å) thickness of Hf and different thicknesses of Ni layer.

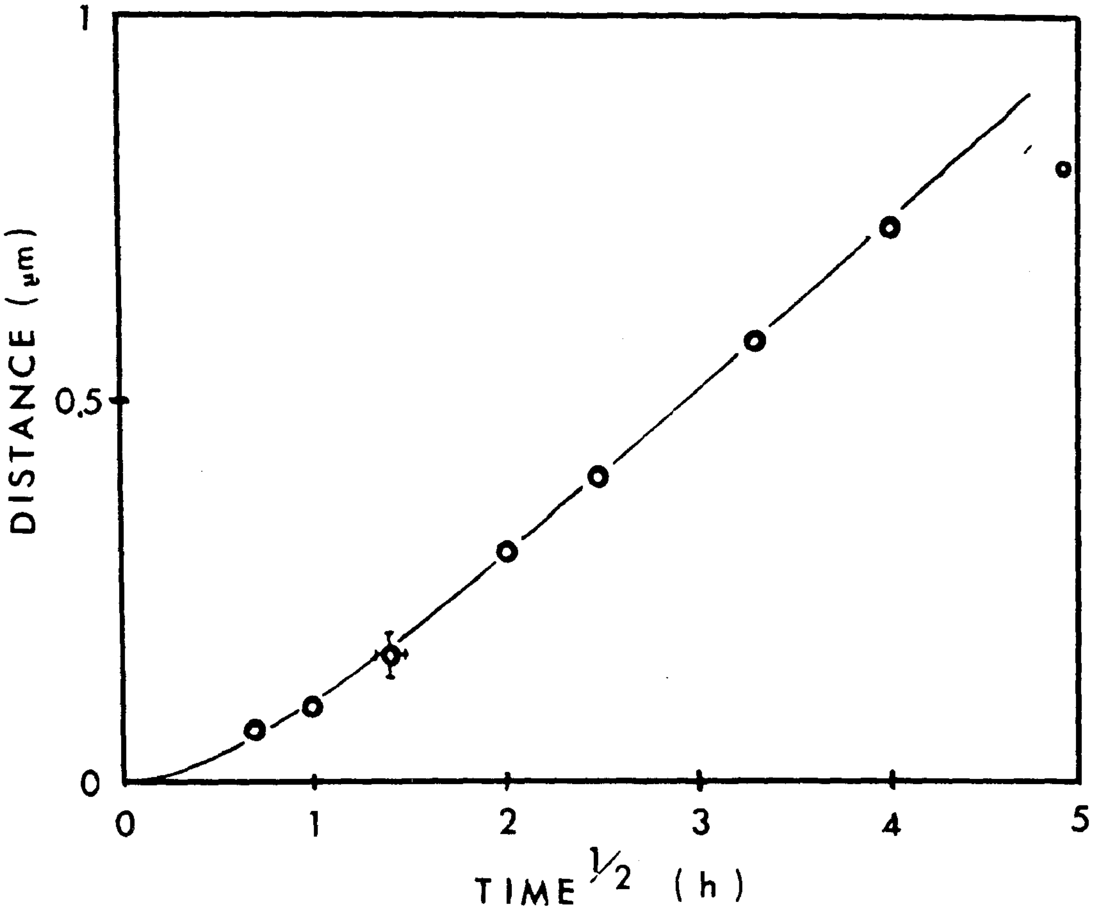

Fig. 36. Penetration depth of the amorphous layer into Hf. The thermal treatment temperature is 340 C. The solid line is the theoretical prediction for the dependence.

In order to obtain the concentration of Ni in the amorphous layer, Ni backscattering signals were numerically transformed to concentration vs. depth profiles. Since this procedure involves the density of the amorphous region, a weighted average of the elemental crystalline densities was assumed. An illustration of the time evolution of the concentration profile is given in Fig. 37. A plot of $(dC/dx)^{-1}$ vs. $t^{1/2}$ is shown in Fig. 38. The values of dC/dx were obtained by a linear fit to the concentration profile in between the regions of the rapid change of concentration (see Fig. 37) The time evolution of the concentration gradient exhibited the same behaviour as the interface position.

VI.4 COMPARISON BETWEEN THE MODEL AND THE EXPERIMENTAL DATA.

The growth of the amorphous alloy results in movements of the Ni front edge and the Hf back edge. Both concentration profiles exhibit typical features of the solid-state reaction: i) a large composition gradient across the mixed layer and ii) a fairly sharp boundary between the amorphous and crystalline regions. The first observation reflects the large metastable homogeneity range[11] of the amorphous phase as compared to most crystalline compounds. The second one suggests that the amorphous layer has a uniform thickness during its growth. It is true that backscattering spectra do not provide indisputable evidence for the microscopic smoothness of the reaction interface, since lateral non-uniformities are averaged out over the cross section of the analyzing beam. Nevertheless, the fact that the interface does not significantly broaden with time (i.e., the slope of

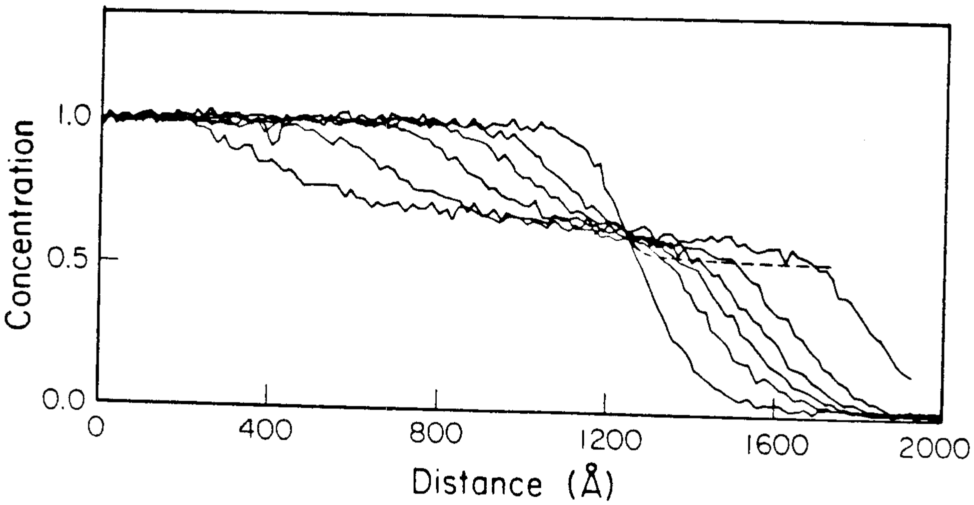

Fig. 37. Concentration profiles for the sample reacted at 340 C. The prediction for the concentration at the interface vs. penetration depth is also shown.

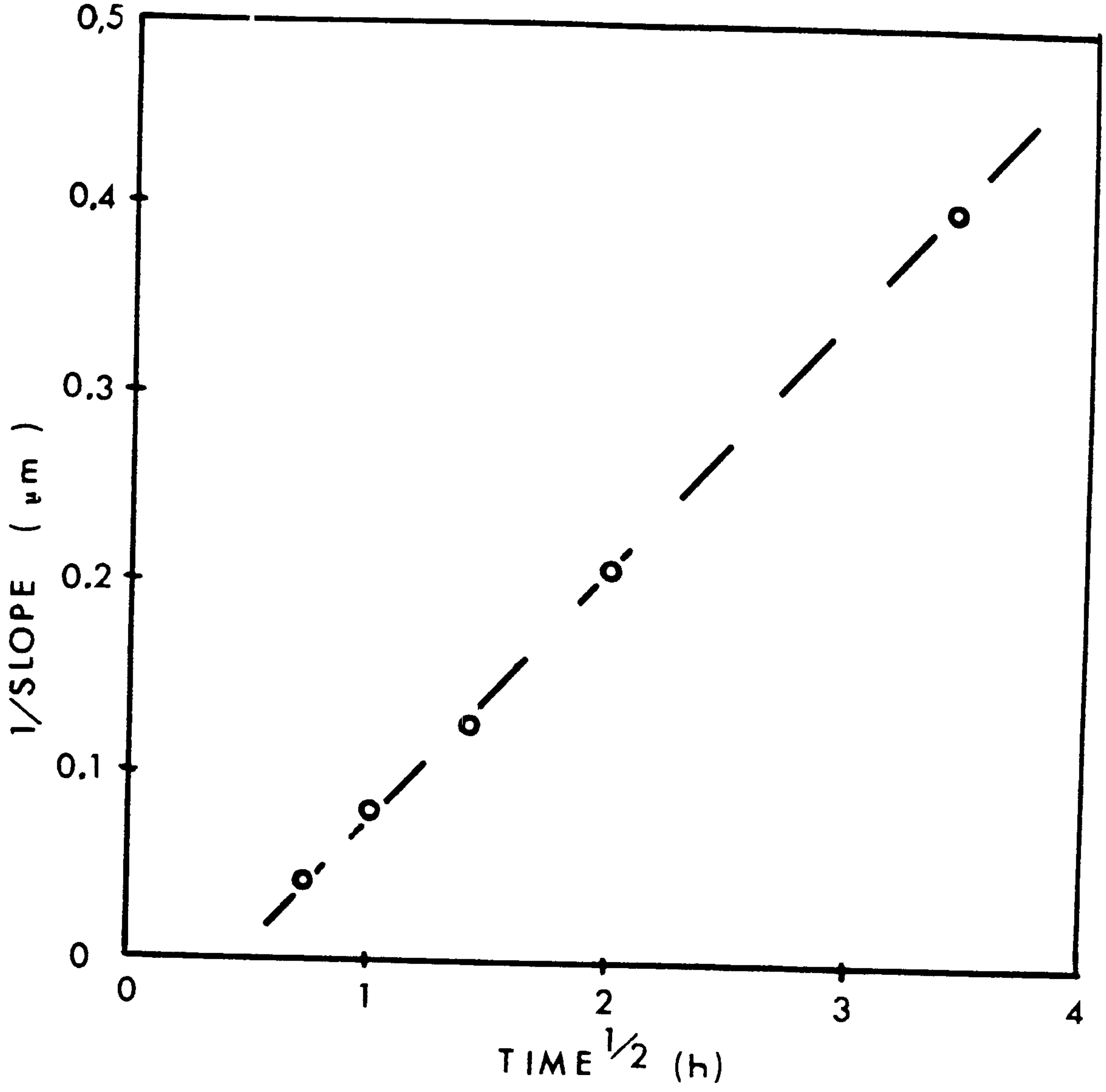

Fig. 38. Time dependence of the Ni concentration gradient.

the moving edge remains approximately constant) clearly rules out the appearance of isolated amorphous islands and favors the picture of a uniform layer growth. An additional argument for a uniform layer growth is a good agreement with a one-dimentional growth model which is discussed below.

Equations (16) and (17) show that the comparison of the slopes of the $t^{1/2}$ dependences of the concentration gradient and the amorphous layer penetration depth (see Figs. 36 and 38) gives the value of the difference $C_{in}-C_2\approx 0.16$. From Fig. 37 the fixed concentration (locus) point has a concentration of $C_{in}\approx 0.62$. From these two values, $A\approx 4$, $C_2\approx 0.46$, and $C_1\approx 0.73$. These parameters are used in the numerical fits described in this article. The estimated range of Ni concentration in the amorphous alloy from $C_2=0.46$ to $C_1=0.73$ agrees extremely well with the predictions of the thermodynamic description[1] calculated in Ref. 30. Since A is the only independent parameter in the Eqns. (9), it should be verified that all the results are fit by the same solution of these equations.

In Fig. 39, experimental points obtained from isothermal treatment sequences at different temperatures have been translated into normalized units and superimposed on the same plot. This figure illustrates the fundamental scale invariance of the reaction. From the fitted curves and the established values of C_{in} and C_2, we can extract values for the effective interdiffusion coefficient D and the boundary parameter κ at different temperatures. The calculated values of D have been plotted vs. inverse temperature in Fig. 40 (Arrheneus plot). From this plot, the activation energy for the diffusion coefficient

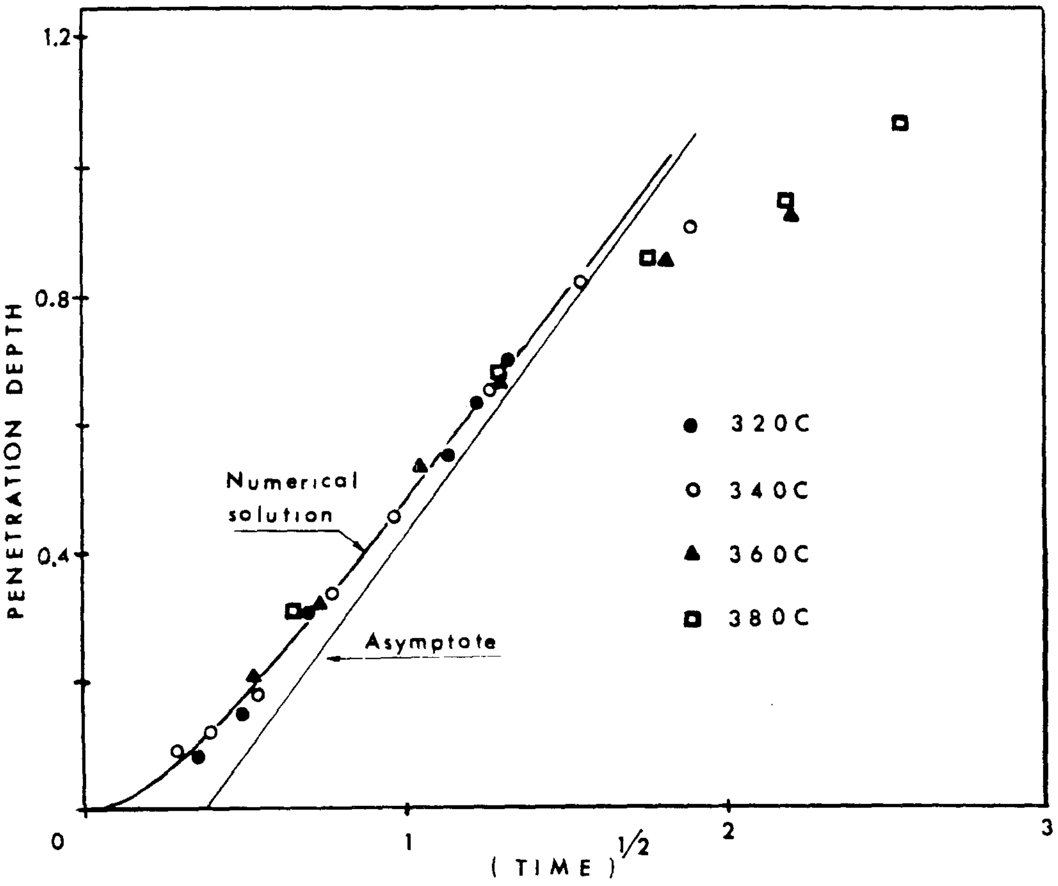

Fig. 39. Comparison between observed and predicted time dependence of the penetration depth. The solid line is the theoretical prediction for the dependence.

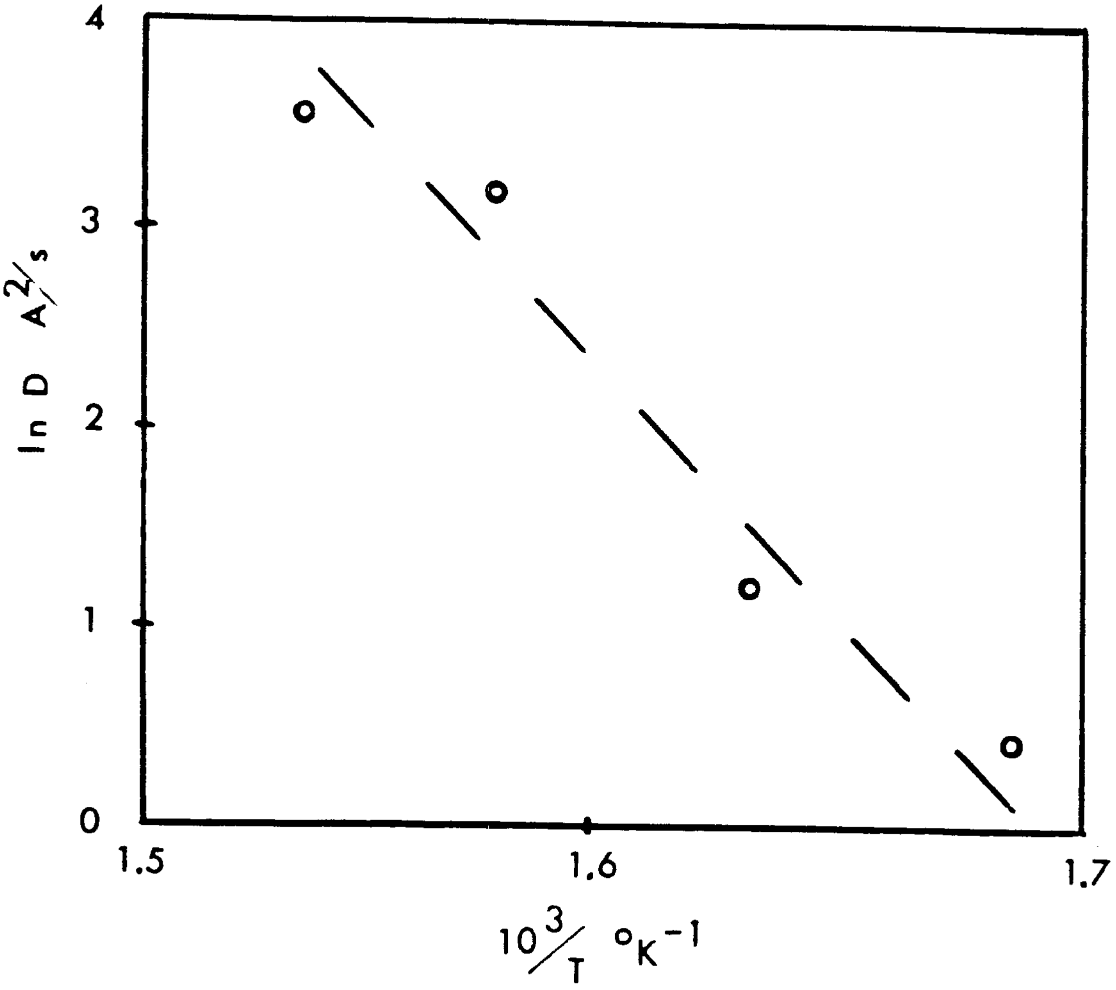

Fig. 40. Arrhenius plot for the values of D.

is 1.6 eV. This value is very reasonable by comparison with the measured diffusion data in ETM-LTM metallic glasses (see Fig. 41). Here ETM and LTM refer to early transition metals and late transition metals in glasses composed of the same. It has been observed that the values of transition metal diffusion coefficients for different relaxed amorphous alloys are correlated with T/T_g, where T_g is the glass transition temperature of the alloy[44]. In Ref. 45, the value of the recrystallization temperature for the amorphous Ni-Hf at a composition close to the ratio of Ni and Hf in our experiment was determined to be 850 K. In fact, T_g should be close to this temperature. The value of T_g permits us to compare the value of the fitting parameter D in our experiment with the diffusion coefficients observed in various metallic glasses. Figure 41 shows this comparison. The values of D and its activation energy are close to that observed for diffusion coefficients near T_g in similar ETM-LTM glasses (e.g.,Ni-Zr). This comparison tends to substantiate the validity of the analysis and suggests that the values of D determined here are probably quite reliable. It is worth mentioning once again that Fig. 41 contains diffusion data for relaxed glasses. Unrelaxed glasses (as may be appropriate to our reacted layer) tend to have somewhat enhanced diffusion coefficients[44].

According to Eq. (16), the value of κ can be derived from the intercept of the $t^{1/2}$ asymptote with the penetration depth axis. The value of this intercept does not show significant changes even when the value of the diffusion coefficient changes with temperature more than an order of magnitude. This constant shift leads to a

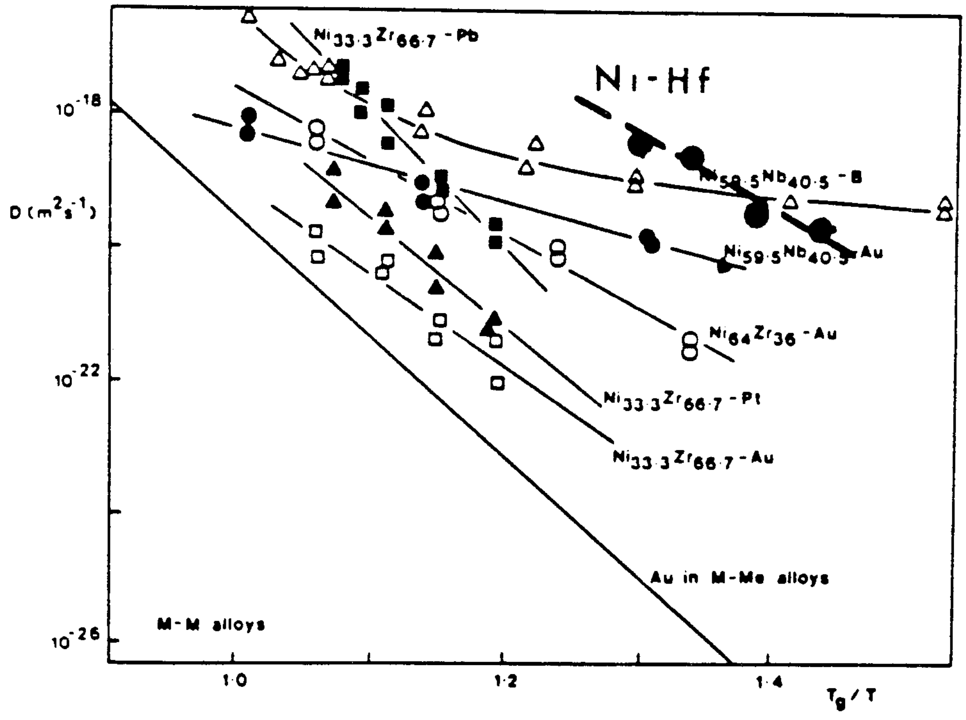

Fig. 41. Normalized Arrhenius plot of directly measured diffusion coefficients (after Ref. 44). Calculated values of parameter D for Ni-Hf couple are shown also.

constant 880 Å length scale for all temperatures and a constant ratio $D/\kappa \approx 140$ Å. This implies that the activation energies for D and κ are close to each other. At 340 C, the value of κ is 0.23 Å/sec and D is 33 Å^2/sec. A meaningfull interpretation of these results can be given only when a fully developed interface model is available. The values of the length scale for Ni-Hf and La-Au systems[6] turned out to be very close. As a result, the values of the boundary parameter κ for both systems must also be nearly the same for equal values of the diffusion coefficient. The maximum possible speed of the interface is of the order of 1/100 of a monolayer per second. This provides a reference point for the future interface models.

It should be emphasized that within the framework of the amorphous layer growth model, the shift in the $t^{1/2}$ asymptote does not imply an incubation time for amorphous layer formation. This shift should not be considered as evidence for nucleation of the amorphous phase. Rather, the value of the shift represents a typical time scale over which the interface kinetics completely dominate the amorphous layer growth. Similar transitions between interface and diffusion controlled growth have been observed in many other thin film systems[48]. The first successful interpretation of this phenomena was given by Deal and Grove[31] for silicon oxide growth on crystalline silicon.

Near the end of the Ni-Hf reaction, deviations from the predicted behaviour are observed. These deviations for different samples seem to scale with the same length and time parameters as the predicted part of the behaviour (see Fig. 39). These deviations take place at the same penetration depth for all the samples with the same geometry, while thinner samples demonstrate this deviation earlier than thicker ones (see Fig. 42). When the moving interface approaches the terminal surface of a pure metal layer, the interface behavior changes. The possible reason for this "proximity effect" is discussed later. A similar apparent slowdown of the reaction during the later stages is observed in measurements performed on the La-Au system and is described in chapters IV and V.

The prediction for the concentration of Ni at the interface vs. the interface penetration depth is plotted in Fig. 37. One consistently observes a change of slope in the measured concentration profile at the predicted position. This correlation leads to the conclusion that the position where this change of slope occurs is related to the position of the interface between the amorphous and the crystalline phases. To determine the exact interface position requires a model for the physical shape of the interface. One must account for experimental resolution, non-planar effects and density changes. We want to emphasize that the value of the C_2 was not obtained from Fig. 37, but was derived from comparison between Fig. 36 and Fig. 38. The behaviour of the predicted boundary concentration is another consistency test for the model.

There are two experimental facts which are not accounted for within the model: 1. The shift of the observed dependency $(dC/dx)^{-1}$ is too large to be explained by the model (see Fig. 38); and 2. the amplitude of the Hf signal in the backscattering profiles decreases up to 10% during the reaction (see Fig. 35). Experimental limitations

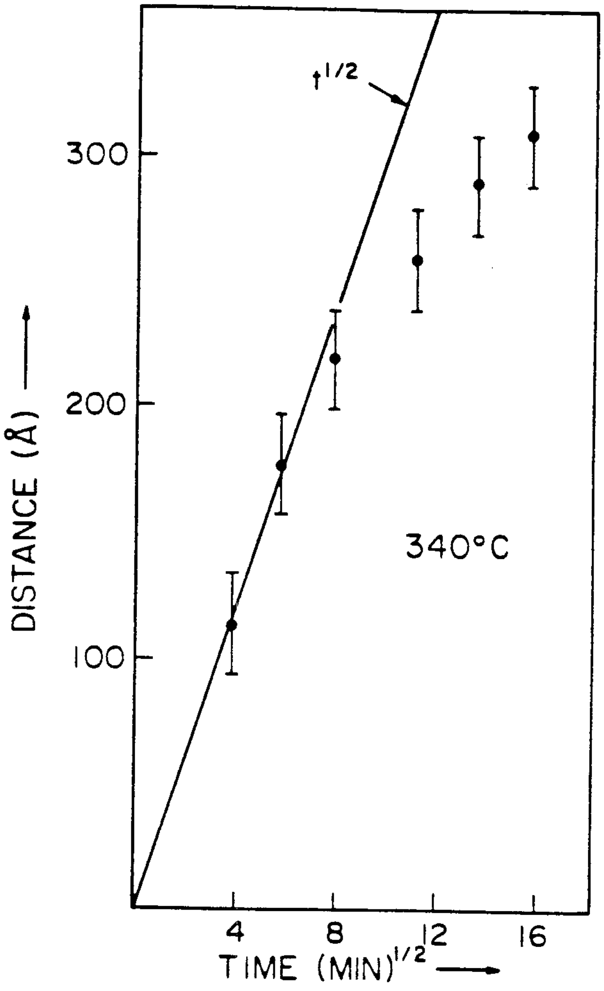

Fig. 42. Penetration depth of the amorphous layer into Hf. The thermal treatment temperature is 340 C. Layers' thicknesses are: Ni - 250 A, Hf - 400 A. (From Ref. 30)

may be responsible for some part of these deviations. The resolution of the backscattering is of the order of 150 Å. This is smaller but comparable to the thickness of the amorphous layer. There are presumably sharp changes in concentration at the ends of the layer which are smeared out by the resolution. This additional smearing can lead to a higher experimental value of dC/dx which can explain some of the shift in the $(dC/dx)^{-1}$ vs. $t^{1/2}$ dependence. The sensitivity of the method to the presence of dissolved Ni in crystalline Hf layer is limited to approximately 5%. The presence of the dissolved Ni could explain the drop in the Hf signal, although it is difficult to explain the 5% of dissolved Ni in crystalline Hf based on the equilibrium phase diagrams of the systems similar to Ni-Hf[46]. Oxygen and Zr impurities, and the presence of a hafnium oxide layer on top of the film, are sources of experimental errors as well. Nevertheless, they can not account for the 10% changes in Hf signal. An explanation can be proposed using the hypothesis of coherency strains at the interfaces. Direct evidence of strain effects comes from the crack and stress patterns observed in the reacted La-Au samples (see Ch. IV). A possible origin of strains is discussed in Ch. IV in connection with the peeling of the thin Au-La samples. The mechanism in question is illustrated by Fig. 43. Figure 43a shows the schematic arrangements of the Ni and Hf atoms before the reaction. Fig. 43b is the same after one monolayer has reacted and if the coherency of Hf atoms at the interface has been preserved. Attempts to maintain coherency in Fig. 43b subjects Hf and Ni atoms in the reacting layers to considerable strains. The distances between Hf atoms in the already reacted layer are different in different

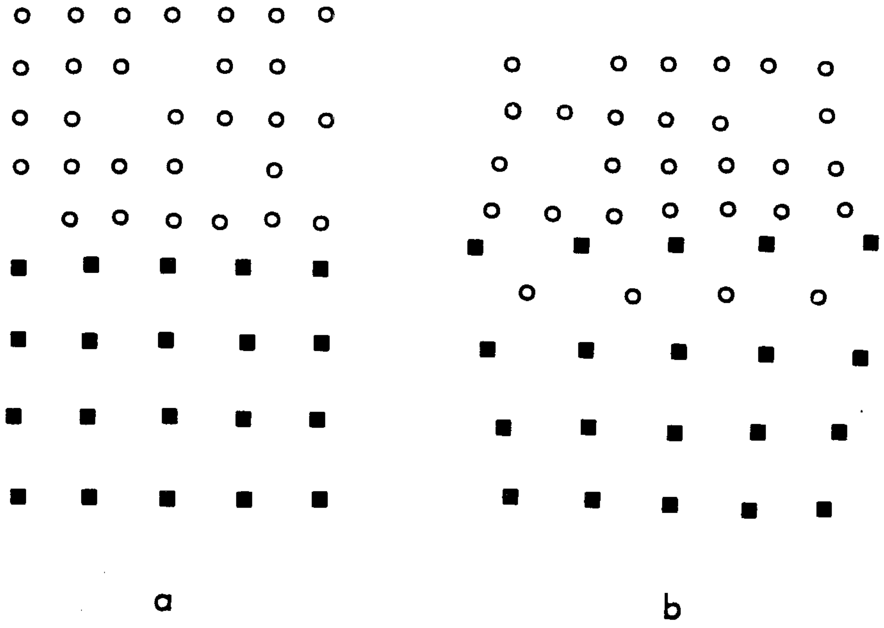

Fig. 43. The atomic arrangements in the case of conserved coherency of the layers: a) Before the reaction. b) After one monolayer has reacted. See description in the text.

directions. These differences are obviously energetically unfavorable and must be decreased at a price of breaking coherency with the crystalline layer. This break in coherency leads to stresses at the interface. A glass, as opposed to a liquid, can sustain stresses, so, as a result, an interface has a stress field associated with it. There are two consequences of this process. 1. The reacted layer tends to become thinner than the total thickness of the original layers. The surface area of the layer tends to be larger than the original surface area. 2. Tremendous stresses are introduced in the Hf layer. Such effects may be partially responsible for the differences between the model and the experiment. The morphology changes might influence the apparent gradient of the concentration of Ni in the reacted layer, while stresses in Hf could cause voids and cracks. The latter might explain the apparent drop in the Hf signal (see Fig. 35). The value of the strain, introduced in Fig. 43b by attempts to conserve the coherency completely, is over 10%. No material can elastically sustain such a strain. In order to make the stresses smaller, the interface must become less sharp and consist of more than one monolayer. Then the stress can decay gradually with the distance from the interface. The simple picture in Fig. 43 is not expected to describe adequately real interface behaviour. This picture is intended to show one possibility for the interface model.

VII. CONCLUSIONS.

The resistance measurements and the Rutherford backscattering are shown to be an extremely powerful tool for studying the Solid State Reaction. The comparison between the observed results and the proposed one-dimensional interface limited diffusion model shows a high degree of agreement. The limits of the validity of the model are demonstrated. They are probably caused by the complicated nature of the interface itself. The reference points for the future physical models of the interface are provided. The calculated values of the diffusion coefficient are in reasonable agreement with the values observed in similar systems.

The agreement of the measurement on Ni-Hf and La-Au systems with the model initially derived for the case of Au-La couple, alone, seems to indicate that this model is a good description of amorphous layer growth by Solid State Reaction as a phenomenon, as opposed to a model for a particular system of metals.

REFERENCES:

1. P. Duwez, R. H. Willens and W. Klement
Nature (London) 187, p.869 (1960)

2. P. Duwez, R. H. Willens and W. Klement
J.Appl.Phys. 31, 1136 and 1500 (1960)

3. D. R. Harbur, J. W. Anderson and W. J. Maramam.
Trans.Met.Soc. AIME 245, 1055 (1969)

4. G. Beghi, R. Matera and G. Piatti
J.Nucl.Mater. 31, 259 (1969)

5. R. Pond and R. Maddin
Mater.Sci.Eng. 23, 87 (1969)

6. M. Laridjani, P. Ramachandrarao and R. W. Cahn
J.Mater.Sci. 7, 627 (1972)

7. W. L. Johnson in Glassy Metals I, ed. by P. Beck and H. J. Guntherodt, Springer-Verlag, Neidelberg, 1981, Ch. 9.

8. W. Buckel and R. Hilsch
Z.Phys. 138, 109 (1954)

9. M. Mehra, W. L. Johnson, A. P. Thakoor, and S. K. Khanna
Sol.State Comm. 47, 859 (1983)

10. R. W. Cahn, Proc. of Conf. on Rapid Solidification Processing, ed. by R. Mehrabian, et al., Reston, 1977, p. 129

11. R. B. Schwarz and W. L. Johnson
Phys.Rev.Let. 51, No 5, 415 (1983)

12. W. L. Johnson, B. P. Dolgin, M. Van-Rossum
Proc. of NATO Advanced Institute: "Glass-Current Issues"
Plenon Press, 1984, in press.

13. X. L. Yeh, K. Sammer and W. L. Johnson
Appl.Phys.Lett. 42, 242 (1983)

14. J. W. Mayer, B.-Y. Tsang, S. S. Lau and L-S. Haung
Nucl.Instr.Methods. 182/183, 1 (1981)

15. W. A. Grant, J.Vac.Sci.Techn. 15, 1644 (1978)

16. C. P. Hinesley, J. G. Morris
Metall. Trans. 1, 1476 (1970)

17. A. R. Miedema and P. F. De Chatel in Theory of Alloy Phase Formation, ed. L. H. Bennett. (American Metals Society, Warrendale, PA 1979, p. 344

18. R. Boom, F. R. De Boer, A. K. Niessen and A. R. Miedema
Physica 11B, pp. 285-309 (1983)

19. See for example O. Penrose and J. L. Lebowitz in Fluctuation Phenomena, ed. by E. W. Montroll and J. L. Lebowitz North Holland, New York, 1979, Ch. 5.

20. D. Turnbull, Contemp. Phys. 10, 473 (1969)

21. C. V. Thompson and F. Spaepen
Acta Metall. 27, 1855 (1979)

22. B. P. Dolgin and W. L. Johnson,
DOE report DOE/ER 10870-146, California Institute of Technology, Pasadena, February 1984.

23. B. P. Dolgin, M. Van-Rossum and W. L. Johnson.
Submitted J.Non-Cryst.Sol, 1984

24. See, for example, G. S. Cargill
Sol.State.Phys. *30*, 227 (1975)

25. See, for example, M. Ruhle and M. Wilkens "*Transmission Electron Microscopy*" in *Physical Melallurgy*,
ed. by R. W. Cahn and P. Haasen,
North-Holland Physics Publishing, New York, 1983, Ch. 11.

26. W. K. Chu, J. W. Mayer and M. A. Nicolet,
Backscattering Spectrometry, Academic Press, New York, 1978

27. M. Hansen, *Constitution of Binary Alloys*,
McGraw Hill Book Co., New York, 1958

28. R. B. Schwarz, K. L. Wong, W. L. Johnson and B. M. Clemens,
J.Non-Cryst.Sol. *61* & *62*, 129 (1984)

29. B. M. Clemens, W. L. Johnson and R. B. Schwarz,
J.Non-Cryst.Sol. *61* & *62*, 817 (1984)

30. M. Van Rossum, M. A. Nicolet and W. L. Johnson,
Phys. Rev. B29. No. 10, 5498 (1984)

31. B. E. Deal and A. S. Grove,
J.Appl.Phys. *36*, 3770 (1965)

32. Ye. Ye. Geguzin, Yu. S. Kaganovski, L. M. Paritskaya and V. I. Solunskiy, *Sov.Phys.Met.Metallov.* *47*, 127 (1978)

33. L. S. Darken, *Trans.Am.Inst.Min.Met.Eng.* *175*, 184 (1948)

34. A. D. Smigelskas and E. O. Kirkendall
Trans.Am.Inst.Min.Met.Eng., *171*, 130 (1947)

35. A. Williams, "*Atomic Structure of Transition Metal Based Metallic Glasses*," PhD Thesis, California Institute of Technology, 1981

36. M. P. Dariel, G. Erez and G. M. J. Schmidt, *Phylos.Mag.*, *19*, 1053 (1969)

37. U. Gosele and K. N. Tu, *J.Appl.Phys.* *53* 4, 3252 (1982)

38. R. Mehrabian, *Int.Metallurg.Rev.*, *27* 185 (1982)

39. C. N. J. Wagner in *Liquid Metals*, ed. by B. Z. Beer, Dekker, New York, 1972

40. See, for example, C. P. Flynn, *Point Defects and Diffusion*, Clarendon Press, Oxford, 1972

41. For discussion of the conversion from a differential equation to a finite difference algorithm, see, for example, R. W. Hamming, *Numerical Methods for Scientists and Engineers*, McGraw Hill Book Co., New York, 1962

42. See, for example, A. Ralston and P. Rabinovitz, *A First Course in Numerical Analysis*, McGraw Hill Book Co., New York, 1978, p. 466

43. See, for example, D. L. Goodstein, *States of Matter*, Prentice-Hall, Inc., Englewood Cliffs, New Jersey 1975

44. B. Cantor and R. W. Cahn in *Amorphous Metallic Alloys*, Butterworth, London, 1983, p. 317

45. K. H. J. Buschow and J. Beekmans, *J.Appl.Phys.* *50*, 6348 (1979)

46. See, for example, *Constitution of Binary Alloys, First Supplement*, ed. by R. P. Elliott, McGraw-Hill Book Co., New York, 1965

Constitution of Binary Alloys, Second Supplement, ed. by F. A. Shunk, McGraw-Hill Book Co., New York, 1969

47. A. D. Le Claire, J.Nucl.Mat. 69, 70 (1978)

48. Proceedings of the symposium on Thin Film Phenomena - Interfaces and Interactions, ed. by J. E. E. Baglin and J. M. Poate, v. 78-2, The Electrochemical Society, Inc., Princeton, 1978

APPENDIX I.

In order to obtain the numerical solution of the system,

$$\begin{cases} [\alpha(C_1-C_{fa}) + (1-\alpha)(C_{am}-C_2)]\,\dfrac{\partial C}{\partial X_a} = \dfrac{\partial^2 C}{\partial X^2} \\ \left.\dfrac{\partial C}{\partial X}\right|_{X_{fa}} = -\,\alpha(1-C_{fa})(C_1-C_{fa}) \\ \left.\dfrac{\partial C}{\partial X}\right|_{X_{am}} = -\,(1-\alpha)C_{am}(C_{am}-C_2) \end{cases}$$

it was substituted by a finite difference equation system for the values of C at points $X_a=nd$, $n=10,11,\ldots$, and $X=kd$, $k=1,2,\ldots,n$. All the derivatives were substituted by the second order finite differences[41]. The solution of the finite difference system is described below.

NUMERICAL EQUATIONS.

Let us define:

- u_k, a set of values of C at points $X=kd$, $k=1,\ldots,n$, for $X_a=nd$
- v_k, a set of values of C at points $X=kd$, $k=1,\ldots,n$, for $X_a=nd+d$
- v_0 and v_{n+1} are the values of C at points $-\,yd$ and $nd+(1-y)d$ correspondingly, where "y" is the ratio of the total increase of the width of the amorphous layer and its penetration depth of the layer in the left.

$$y = \alpha(C_1-u_1)/[\alpha(C_1-u_1)+(1-\alpha)(u_n-C_2)]$$

The positions of points u_k, v_k in space are described in Fig. 44. The values of v_k and u_k are connected by the following set of equations:

$$u_1=v_1-2F[v_0/y(1-y)-v_1/y+v_2/(1-y)]$$

$$u_k=v_k-F(v_k-2v_k+v_{k+1}) \quad , \ k=2,\ldots,n-1$$

$$u_n=v_n-2F[v_{n-1}/(2-y)(1-y)-v_n/(1-y)+v_{n+1}/(2-y)]$$

$$v_0-v_1=\alpha dy(1-U_0)(C-U_0)=\Delta_1$$

$$v_n-v_{n+1}=(1-\alpha)d(1-y)U_n(U_n)=\Delta_2$$

where

$$F=[\alpha d(C_1-U_0)+d(1-\alpha)(U_{n+1}-C_2)]^{-1}$$

$$U_0=1.5u_1-0.5[u_1 \text{ for } X_a=(n-1)d]$$

$$U_n=1.5u_n-0.5[u_{n-1} \text{ for } X_a=(n-1)d]$$

U_0 and U_n are average values for the concentration at the boundary for two consecutive positions of the interfaces. As in the rest of the equations these values are approximated with d^2 accuracy.

The system of equations can be rewritten in a matrix form:

$$\begin{vmatrix}0\\u_1\\u_2\\u_k\\u_{n-1}\\u_n\\0\end{vmatrix} + \Delta_1\cdot\begin{vmatrix}1\\0\\0\\0\\0\\0\\0\end{vmatrix} + \Delta_2\cdot\begin{vmatrix}0\\0\\0\\0\\0\\0\\1\end{vmatrix} =$$

$$\begin{Vmatrix}
1 & -1 & & & & & 0 \\
-2F/(1-y) & 1+2F/y & -2F/y/(1-y) & & & & \\
0 & -F & 1+2F & -F & & & \\
 & & \cdots & & & & \\
 & & -F & 1+2F & -F & & \\
 & & & \cdots & & & \\
0 & & & -F & 1+2F & -F & \\
 & & & & -2F/(2-y)(1-y) & 1+F/(1-y) & -2F/(2-y) \\
 & & & & & 1 & -1
\end{Vmatrix} \cdot \begin{vmatrix}v_0\\v_1\\v_2\\\cdot\cdot\\v_k\\\cdot\cdot\\v_{n-1}\\v_n\\v_{n+1}\end{vmatrix}$$

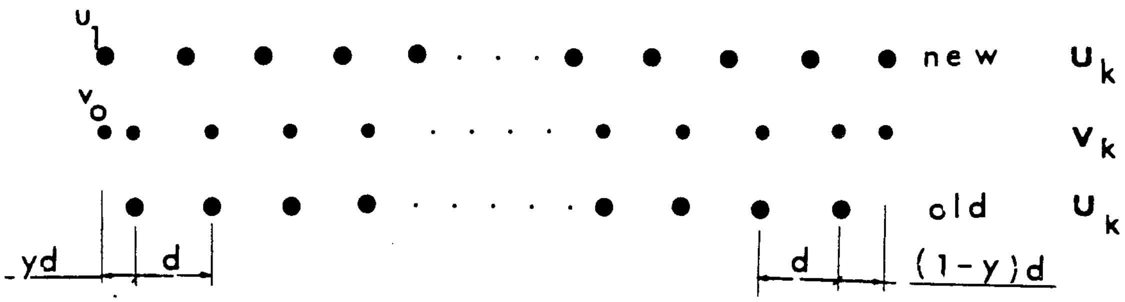

Fig. 44. Coordinates of the points in two consecutive iterations for the numerical solution of the diffusion equations. See the description in the text.

The tridiagonal matrix on the right side of the equation will be referred to as $\|G\|$. This matrix can be easily inverted. The standard algorithm for this inversion[42] starts with rewriting this matrix as a multiple of two bidiagonal matrixes:

$$\|G\| = \|H\| \cdot \|I\|$$

$$\left\| \begin{array}{ccccc} a_1 & b_1 & & & O \\ c_1 & a_2 & b_2 & & \\ & \cdots & \cdot & \cdot & \cdot \\ & & c_{n-1} & a_{n-1} & b_{n-1} \\ O & & & c_n & a_n \end{array} \right\| = \left\| \begin{array}{ccccc} 1 & & & & O \\ e_1 & 1 & & & \\ & & \cdot\;\cdot\;\cdot & & \\ & & e_{n-2} & 1 & \\ O & & & e_{n-1} & 1 \end{array} \right\| \cdot \left\| \begin{array}{ccccc} f_1 & b_1 & & & O \\ & f_2 & b_2 & & \\ & & \cdot\;\cdot\;\cdot & \cdot & \\ & & & f_{n-1} & b_{n-1} \\ O & & & & f_n \end{array} \right\|$$

where $f_1 = a_1$

$e_k = a_k/f_{k-1}$

$f_k = a_k - e_{k-1}b_{k-1}$.

So, the original matrix equation can be written now in the symbolic form:

$$|y_k| = |u_k| + |\Delta_1| + |\Delta_2| = \|H\| \cdot \|I\| \cdot |v_k|$$

The vector $|y_k|$ was introduced to simplify the notation. The solution of this equation is obtained in two steps:

First: $|x_k| = \|H^{-1}\| \cdot |y_k|$, where

$x_1 = y_1$

$x_k = y_k - e_k\, y_k,$ $k=2, \ldots n+1$.

Second: $|v_k| = \|I^{-1}\| \cdot |x_k|$, where

$$v_{n+1} = x_{n+1} / f_{n+1}$$

$$v_k = (x_k - b_k v_{k+1}) / f_k , \quad k=n,n-1, \ldots 1 .$$

After both steps are performed the original system of equations will have the following form:

$$v_0 = s_0 + t_0 \Delta_1 + r_0 \Delta_2 \tag{A1}$$

$$v_k = s_k + t_k \Delta_1 + r_k \Delta_2 \quad k=1, \ldots n \tag{A2}$$

$$v_{n+1} = s_{n+1} + t_{n+1} \Delta_1 + r_{n+1} \Delta_2 \tag{A3}$$

where

$$\Delta_1 = \alpha\, dy(1-v_0)(C_1-v_0)$$

$$\Delta_2 = (1-\alpha)d(1-y)v_{n+1}(v_{n+1}-C_2)$$

s_k, t_k, r_k are sets of numbers obtained from the procedure described earlier.

The system of two quadratic equations (A1) and (A3) can be solved by a method of successive approximations. The solution gives values of v_0 and v_{n+1}. These variables determine Δ_1 and Δ_2. Eqns. (A2) define the rest of v_k.

At this step, the solution v_k is found. In order to repeat the iteration, the values at the set of equidistant points (see Fig. 43) must be found. Quadratic interpolation formulas[41] can do the job.

The-three step algorithm was implemented in the FORTRAN program "DFN." The listing of the program follows.

PROGRAM DFN.FOR

```
        IMPLICIT REAL*8 (A-H,P-Z)
        INTEGER*2 NAME(5),NAME1(5)
        REAL*8 C(1001),D(999),E(1001),H(1001)
C
C     INPUT DATA FILE IS DIFDAT.DAT
C
C         Input data for each calculation consists of 4 lines of data.
C     There can be as many sets of these 4 lines as one needs.
C
C        Each of these lines contains:
C
C     1 line ( FORMAT (4G15.5) ):  C1, C2,  , and maximum value of Xam.
C     2 line ( FORMAT (6A2) ) : Name of the file which will contain the
C         values of Xam, C(X1), C(X2), time and amount of the fast
C         diffuser in the interlayer.
C     3 line ( FORMAT (6A2) ) : Name of the file which will contain the
C       concentration profiles  at  the  points  which  are described
C         in the line 4.
C     4 line ( FORMAT (*)  ) :  N1, M, N2, M1, M2;  where N1 is the
C          number of points in the initial linear approximation for the
C          distribution of the fast diffuser  (usually 5);  N2  maximum
C          number  of  the  iteration  steps  performed;  M defines the
C          number of steps after which the concentration and  positions
C          will be saved in the file defined in line 2; M1 same for the
C          line 3;  if M2>1 then the whole calculation will be repeated
C          for the twice larger maximum value of Xam.   It will be done
C          M2 times.
C
C
      OPEN (UNIT=1,NAME='DIFDAT.DAT',TYPE='OLD')
 20   READ (1,40,END=9990) C1,C2,ALF,XL
      TYPE *,'C1=',C1,'C2=',C2,'ALPHA=',ALF,'X=',XL
 40   FORMAT (9G15.5)
      READ (1,50) (NAME(I),I=1,5)
      TYPE 50,NAME
      READ (1,50) (NAME1(I),I=1,5)
      TYPE 50,NAME1
      READ (1,*) N1,M,N2,M1,M2
      TYPE *,'N1=',N1,'M=',M,'N2=',N2,'M1=',M1,'M2=',M2
      TYPE *,'              Loop 0'
 50   FORMAT (2(1X,5A2))
C
C       All input data are in
C
      OPEN (UNIT=2,NAME=NAME,TYPE='NEW')
      PRINT *,'C1=',C1,'C2=','ALPHA=',ALF,'X=',X
      PRINT *,'N1=',N1,'M=',M,'N2=',N2,'M1=',M1,'M2=',M2
      PRINT 50,NAME,NAME1
      WRITE (2,*) ' C1=',C1,'C2=','ALPHA=',ALF,'X=',X
```

```
      WRITE (2,*) ' N1=',N1,'M=',M,'N2=',N2,'M1=',M1,'M2=',M2
      OPEN (UNIT=3,NAME=NAME1,TYPE='NEW')
      WRITE (3,*) ' C1=',C1,'C2=','ALPHA=',ALF,'X=',X
      WRITE (3,*) ' N1=',N1,'M=',M,'N2=',N2,'M1=',M1,'M2=',M2
      DEL=XL/FLOAT(N2-1)
      ALF1=1.D0-ALF
 55   FORMAT (I5,10G13.6)
      PRINT *,'    N   ','  Time    ','      X2       ',
     1'    C1        ','    C2       ','   Integral ','    XL     ',
     2'Pos of 0 curv',' Conc there'
C
C
C          Initial distribution of the concentration is assumed
C                    to be linear
C
C
      C81=ALF*(1+C1)-ALF*C2
      C82=2.D0*ALF*C1
      C0=C82/(C81+DSQRT(C81*C81+2.D0*(1.D0-2.D0*ALF)*C82))
      SL=DEL*ALF1*(C0-C2)*C0
      DO 80 I=1,N1
 80   C(I)=C0-SL*(FLOAT(I)-.5D0*FLOAT(N1+1))
      X1=ALF*(C1-C(1))
      X2=ALF1*(C(N1)-C2)
      T=DEL*FLOAT(N1-1)*2.D0/(X1+X2+2.D0*ALF*(C1-C0))
      XL=DEL*FLOAT(N1-1)*X1/(X1+X2)
      D1+C(1)-DEL*SL*X1/(X1+X2)
      D2=C(N1)+DEL*SL*X2/(X1+X2)
C
C
C     Initializing of variables is through
C
C
      DO 9100 N999=1,M2
      DO 9000 N=N1+1,N2
C
C
C     The elements of the matrix to be inverted are calculated
C
C
      N0=N-1
      N01=N-2
      X1=ALF*(C1-1.5D0*C(1)+.5D0*D1)
      X2=ALF1*(1.5D0*C(N0)-.5D0*D2-C2)
      X=X1/(X1+X2)
      XL=XL+DEL*X
      F=1.D0/DEL/(X1+X2)
      F1=F*F
      F2=2D0*F
C
C     The inversion of the matrix starts
C
```

```
      D1=C(1)
      D2=C(0)
      A1=F2+1.D0
      D(1)=1.D0+F2/(1.D0+X)
      E(1)=F2/X/(1.D0+X)
      B1=F/D(1)
      E(2)=B1*E(1)
      C(2)=C(2)+B1*C(1)
      A2=A1-B1*F2/(1.D0+X)
      D(2)=A2
      DO 100 I=3,N01
      B1=F/A2
      C(I)=C(I)+B1*C(I-1)
      E(I)=E(I-1)*B1
      A2=A1-B1*F
  100 D(I)=A2
      B1=F2/(2.D0-X)/A2
      A2=1+F2/(1.D0-X)-B1*F
      H(N)=1.D0/(F2/A2/(1.D0-X)/(2.D0-X)-1.D0)
      E(N)=-E(N01)*B1*H(N)/A2
      C(N)=-(C(N0)+B1*C(N01))*H(N)/A2
      C(N0)=C(N)
      E(N0)=E(N)
      H(N0)=H(N)+1.D0
      DO 200 I=N01,2,-1
      E(I)=(E(I)+F*E(I+1))/D(I)
      H(I)=F*H(I+1)/D(I)
  200 C(I)=(C(I)+F*C(I+1))/D(I)
      E(1)=(E(1)+F2*E(2)/(1.D0+X))/D(1)
      C(1)=(C(1)+F2*C(2)/(1.D0+X))/D(1)
      H(1)=F2*H(2)/(1.D0+X)/D(1)
C
C
C      The values of the first and the last elements are to be
C         determined
C
C
      S11=(1.D0+E(1))*ALF*X*DEL
      S12=H(1)*ALF1*DEL*(1.D0-X)
      C71=1.D0+(C1+1.D0)*S11
      S21=E(N)*ALF*X*DEL
      S22=H(N)*ALF1*DEL*(1.D0-X)
      C81=1.D0+C2*S22
      S1=C(1)
      S2=C(N)
  220 C72=2.D0*(C(1)+S11*C1+S12*(S2-C2)*S2)
      S3=C72/(C71+DSQRT(C71*C71-2.D0*S11*C72))
      C82=2.D0*(C(N)+S21*(C1-S3)*(1.D0-S3))
      S4=C82/(C81+DSQRT(C81*C81-2.D0*S22*C82))
      IF (S1.EQ.S3) GO TO 240
      S1=S3
      S2=S4
```

```
      GO TO 220
 240  C(N)=S2
      X1=ALF*DEL*X*(C1-S1)*(1.D0-S1)
      X2=ALF1*DEL*(1.D0-X)*(S2-C2)*S2
      DO 250 I=1,N0
 250  C(I)=C(I)+E(I)*X1+H(I)*X2
      S3=C(N01)+.5D0*(1.D0-X)*C(N0)-C(N-3)+(1.D0-X)(C(N0)+C(N-3)
     1-C(N01)*2.D0))
C
C
C     The values of the concentration are going to be recalculated
C         for the equidistant points.
C
C
      DO 300 I=N01,2,-1
      S4=C(I)+.5D0*X*(C(I-1)-C(I+1)+X*(C(I+1)+C(I-1)-C(I)*2.D0))
      C(I+1)=S3
 300  S3=S4
      C(2)=S3
      C(1)=S1
      T=T+F*DEL*DEL
C
C
C     The calculated values of the concentration are to be saved in
C         corresponding files
C
C
      IF (M*(N0/M).NE.N0) GO TO 8890
      S=.5D0*(S1+S2)
      DO 8000 I=2,N0
      IF (C(I+1)+C(I-1)-2.D0*C(I).LT.0D0) I2=I
 8000 S=S+C(I)
      X1=FLOAT(N0)
      X2=X1*DEL
      X3=DEL*FLOAT(I2-1)-XL
      S=S*DEL
      WRITE (2,40) T,X2,S1,S2,S,XL,X3,C(I2)
      PRINT 55,N,T,X2,S1,S2,S,XL,X3,C(I2)
      IF (M1*(N0/M1).NE.N0) GO TO 8890
      DO 8300 I=1,N/10
 8300 WRITE (3,8400) (C(10*I+J),J=-1,0)
      WRITE (3,8400) C(N)
 8400 FORMAT (10F11.8)
 8890 TYPE 8900,N
 8900 FORMAT ('+N=',I4,G10.2)
 9000 CONTINUE
      DEL=DEL+DEL
      N1=(N2+1)/2
      DO 9100 I=1,N1
      C(I)=C(2*I-1)
      TYPE 9050,N999
 9050 FORMAT('+              Loop', I4)
```

```
9100 CONTINUE
     IF (M1.LE.N2) GO TO 9300
     DO 9200 I=1,N2/20
9200 WRITE (3,8400) C(10*I+J),J=-9,0)
     WRITE (3,8400) C(N1)
9300 CLOSE (UNIT=2,DISP='SAVE')
     CLOSE (UNIT=3,DISP='SAVE')
     GO TO 20
9990 STOP
     END
```

APPENDIX II.

Solutions of the equations (9) can be obtained from the following Taylor expansion for the solution of the system:

$$C\ (X_{am}, X) = \sum_{n=0}^{\infty} \ C_n(X_{am})\ \frac{(X_{am}-X)^n}{n!}$$

where factors C_n satisfy

$$\begin{cases} C_0 = C_{am} \\ C_1 = C_0\ (C_0 + A - 1) \\ C_n = C_0\ (C_{n-1} + \dfrac{dC_{n-2}}{dX_{am}}\ ) \\ \displaystyle\sum_{n=0}^{\infty} C_n(X_{am}) \frac{X^n_{am}}{n!} = 1 \end{cases} \quad .$$

Substitution of C_n by their asymptotic expansion in a form

$$C_n = \sum_{m=0}^{\infty} \frac{a^n_m}{X^{n+m}_{am}\ (A-1^{n-1}}$$

leads to the following set of equations:

$$\begin{cases} a^0_n = 0 & \text{(A4)} \\ a^1_m = a^0_{m+1} + \displaystyle\sum_{k=0}^{n} a^0_k\ a^0_{m+1-k} & \text{(A5)} \\ a^0_m = a^0_1\ (a^{n-1}_m - (n+m-2)\ a^{n-2}_m) + \displaystyle\sum_{k=1}^{m} b_k a^n_{m-k} & \text{(A6)} \\ \displaystyle\sum_{n=0}^{\infty} \frac{a^n_m}{n!} = 1 \text{ if } m = 0 \text{ and } 0 \text{ if } m > 0 & \text{(A7)} \end{cases}$$

where

$$b_1 = a_2^0 \,/\, a_1^0$$

$$b_n = \left(a_{n-1}^0 - \sum_{k=1}^{n-1} b_k\, a_{n-k+1}^0\right) / \, a_1^0$$

If one introduces $a=a_1^0$, then factors a_0^n can be written as polynome of "a" in a form:

$$a_0^n = \sum_k d_k^n\, a^k .$$

Substitution into the system (A6) gives following relations between d

$$d_k^n = 0 \qquad \text{for } k<0 \text{ and } n<2k;$$

$$d_n^n = 1$$

$$d_{n-k}^n - d_{(n-1)-k}^{(n-1)} = -\,(n-2)\, d_{(n-2)-(k-1)}^{(n-2)} .$$

From this, one can obtain values of d_k^n in a form:

$$d_{n-k}^n = \sum_{m=k}^{n-2} m\, d_{m-(k-1)}^m = \frac{(-1)^k (n-1)!}{2^k k!(n-2k-1)!}$$

Substitution into (A7) gives the following equation for the value of "a":

$$1 = \sum_n \frac{a_0^n}{n!} = \sum_n \sum_k \frac{d_k^n a^k}{n!} = \sum_{k=1}^{\infty} a^k \sum_{n=k}^{2k-1} \frac{d_k^n}{n!} = \sum_{n=1}^{\infty} a^n \,\frac{2^{k-1}(k-1)!}{(2k-2)!}$$

One can check that $a_2^0=-a$, $b_1=-1$ and $a_1^n=a_0^{n+2}/a$ satisfies all the equations for a_1^n.

a_2^n must satisfy an equation

$$a_2^n = a(a_2^{n-1} - na_2^{n-2}) - a_1^n + b_2a_0^n \quad , \quad n = 2,3, \ldots$$

From this,

$$\sum_{n-2}^{\infty} \frac{a_2^n}{n!} = a \sum_{n-2}^{\infty} \left(\frac{a_2^{n-1}}{n!} - \frac{a_2^{n-2}}{(n-1)!} \right) - \sum_{n-2}^{\infty} \frac{a_1^n}{n!} + b_2 \sum_{n-2}^{\infty} \frac{a_0^n}{n!} \; .$$

If the summation was done from 0 to ∞ then all the sums except for the last one would have been equal to zero. This fact and the values for a_1^n for n=0,1 lead to $b_2=0$ and $a_3^0=a$.

It was proved so far that

$$C_{am} = C_0 = \frac{a}{X_{am}} - \frac{a}{(A-1)X_{am}^2} + \frac{a}{(A-1)^2X_{am}^3} - \frac{a(1+b_3)}{(A-1)^3X_{am}^4} + \ldots$$

or

$$C_{am} = \frac{1}{X_{am} + \frac{1}{A-1}} - \frac{ab_3}{(A-1)^3X_{am}^4} + \ldots$$

which is the result referred to in equation (14) in the text.

An equation for b_3 can be obtained in a similar manner. Numerical calculations for A-1 from 0.1 to 1000 have shown that $b_3 \approx 1/3(A-1)$ and $b_4 = 2b_3$.